3D nanoimprint technology for NIR Fabry-Pérot filter arrays

Fabrication, characterization and comparison of different cavity designs

Dissertation for the Acquisition of the Academic Degree

Doktor der Ingenieurwissenschaften (Dr.-Ing.)

Faculty of Electrical Engineering and Computer Science

University of Kassel

Germany

By

Duc Toan Nguyen, M.Sc.

Kassel, April 2016

Erklärung

Hiermit versichere ich, dass ich die vorliegende Dissertation selbstständig, ohne unerlaubte Hilfe Dritter angefertigt und andere als die in der Dissertation angegebenen Hilfsmittel nicht benutzt habe. Alle Stellen, die wörtlich oder sinngemäß aus veröffentlichten oder unveröffentlichten Schriften entnommen sind, habe ich als solche kenntlich gemacht. Dritte waren an der inhaltlich-materiellen Erstellung der Dissertation nicht beteiligt; insbesondere habe ich hierfür nicht die Hilfe eines Promotionsberaters in Anspruch genommen. Kein Teil dieser Arbeit ist in einem anderen Promotions- oder Habilitationsverfahren verwendet worden.

Kassel, April 2016

Duc Toan Nguyen, M.Sc.

Eingereicht am:	20. April 2016
Tag der Disputation:	17. June 2016
Gutachter:	Prof. Dr. Hartmut Hillmer Prof. Dr. Peter Lehmann
Promotionskommission:	Prof. Dr. Hartmut Hillmer Prof. Dr. Peter Lehmann Prof. Dr. Axel Bangert Prof. Dr. Marcus Ziegler

Acknowledgements

First of all, I would like to give many thanks to Prof. Dr. Hartmut. Hillmer for giving me the chance to work in the fantastic field of Microsystems technology and offering me the opportunity to work at INA. I have learned a lot under his sustained and skillful guidance.

My great gratitude to Prof. Dr. Lehmann for co-supervising my thesis.

I am also appreciated with all the current and former members of nanospectrometer group for the successful teamwork. They are Dr. Albrecht, Dr. Woit, Dr. Mai, Dr. Ullah, Carsten Woidt, Tamara Meinl, André Istock, Imran Memon, Yannan Shen, Waleed Al-Esayi, Ramya Kolli and Ikram Hafiz.

My gratefulness to my former master and project work student Muath Ababtain and Nikolai Yurttagül for their contribution.

I would like to thank to Dietmar Gutermuth, Jens Krumpholz, Anita Dueck and other INA colleagues for their technical support.

My appreciate goes to Dr. Manuel Thesen from Micro resist technology GmbH. and Dr. Marc Verscheeren from Philips Research for those resist support and valuable scientific discussion.

I would like to thank the Ministry of Education and Training (Vietnam) for the finance support.

Last but not least, I would like to express my deep and sincere gratitude to my family: my parents, my brothers and sisters, especially my wife for their unconditional support and encouragement in all the past years.

Zusammenfassung

Im Rahmen dieser Arbeit wird die Herstellung von miniaturisierten NIR-Spektrometern auf Basis von Fabry-Pérot (FP) Filter Arrays behandelt. Bisher ist die kostengünstige Strukturierung von homogenen und vertikal erweiterten Kavitäten für NIR FP-Filter mittels Nanoimprint Technologie noch nicht verfügbar, weil die Qualität der Schichten des Prägematerials unzureichend ist und die geringe Mobilität der Prägematerialien nicht ausreicht, um die vertikal erweiterten Kavitäten zu füllen. Diese Arbeit konzentriert sich auf die Reduzierung des technischen Aufwands zur Herstellung von homogenen und vertikal erweiterten Kavitäten. Zur Strukturierung der Kavitäten wird ein großflächiger substratkonformer UV-Nanoimprint Prozess (SCIL - Substrate Conformal Imprint Lithoghaphy) verwendet, der auf einem Hybridstempel basiert und Vorteile von harten und weichen Stempeln vereint. Um die genannten Limitierungen zu beseitigen, werden alternative Designs der Kavitäten untersucht und ein neues Prägematerial eingesetzt. Drei Designlösungen zur Herstellung von homogenen und erweiterten Kavitäten werden untersucht und verglichen: (i) Das Aufbringen des Prägematerials mittel mehrfacher Rotationsbeschichtung, um eine höhere Schichtdicke des Prägematerials vor dem Prägeprozess zu erzeugen, (ii) die Verwendung einer hybriden Kavität bestehend aus einer strukturierten Schicht des Prägematerials eingebettet zwischen zwei Siliziumoxidschichten, um die Schichtdicke der organischen Kavität zu erweitern und (iii) die Optimierung des Prägeprozesses durch Verwendung eines neuen Prägematerials. Die mit diesen drei Ansätzen hergestellten FP-Filter Arrays zeigen, hohe Transmissionen (beste Transmission > 90%) und kleine Linienbreiten (Halbwertsbreiten <5 nm).

Schlagworte: NIR Spektrometer, 3D-Nanoimprint, Nanospektrometer, Fabry-Pérot-Filter, Miniaturisierung.

Abstract

The fabrication of miniaturized NIR spectrometers based on arrays of multiple Fabry-Pérot (FP) filter are reported within this thesis work. Today, the low-cost patterning of homogeneous extended cavity heights for NIR filters using the conventional spin –coated nanoimprint methodology is not available because of insufficient coating layers and low mobility of the resist materials to fill extended cavity structures. This work will focus on the reducing of the technological effort for fabrication of homogeneous extended cavities. Alternative cavity designs are studied, including a new resist and large-area 3D nanoimprint based on a hybrid mold and apply UV Substrate Conformal Imprint Lithography (UV-SCIL) to overcome these limitations. Three different solutions for structuring homogeneous extended cavity heights are presented and compared, i.e. (i) applying the multiple spin coating of the resist to obtain thicker initial resist layer, (ii) introducing a hybrid cavity (combination of thin oxide layer and the organic cavity) to compensate the height differences, and (iii) optimizing the imprint process with a novel resist material. The imprint results based on these methods demonstrate the implementation of NIR FP filters with high transmission intensity (best single transmission >90%) and small line widths (<5 nm in full width at half maximum).

Key words: near infrared, spectrometer, 3D nanoimprint, nanospectrometer, Fabry-Pérot filter, miniaturization.

Contents

1. INTRODUCTION AND MOTIVATION..1
2. THEORETICAL BASICS 6
2.1. Foundation of Fabry-Pérot filter and its optical parameters 6
2.1.1 Distributed Bragg Reflectors (DBRs)..6
2.1.2 Fabry-Pérot Filter...8
2.1.3 Optical parameters of FP filters 11
2.2 State of the Art: Fabry-Pérot Filter based nanospectrometers 12
2.3 Foundation of nanoimprint technology 15
2.3.1 Introduction of nanoimprint...15
2.3.2 Classification of nanoimprint lithography methods 15
2.3.3 Nanoimprint methods 16
2.3.4 Nanoimprint resists materials 20

3. RELEVANT TECHNOLOGICAL PROCESS..22
3.1 Foundations of deposition and patterning methods 22
3.1.1 Basics of Plasma enhanced chemical vapor deposition (PECVD)...................22
3.1.2 Basics of Ion beam sputtering deposition (IBSD) 24
3.2. Foundation of the applied characterization methods. 35
3.2.1. Basics of spectroscopic ellipsometry..35
3.2.2 Basics of white light interferometer (WLI) 38
3.2.3 Introduction of the measurement setup for spectral characterization...............39

4. DESIGN, SIMULATION AND FABRICATION OF NIR FP FILTERS 48
4.1 Design of NIR static FP filters 48
4.2 Simulation of NIR static FP filters 50
4.2.1 Simulation of DBRs for FP filters 50
4.2.2 Simulation of NIR static FP filter arrays 51
4.3 Discussion of the simulation results 53
4.3.1 Deposition rate of PECVD and deformation of stop-band of FP filters............53
4.3.2 Simulated optical properties of FP filter arrays in three different methods 54
4.4 Fabrication of NIR static FP filters 57

5. FABRICATION AND CHARACTERIZATION OF MASTER TEMPLATE FOR THE NEAR INFRARED RANGE 59
5.1 Fabrication of master templates for NIR range.. 59
5.2. Experimental results of NIR master template and discussion.................................... 62
5.2.1 Experimental results 62
5.2.2 Discussion of the experimental result..63
5.3 Soft stamp replication.. 66

6. FABRICATION AND CHARACTERIZATION OF STATIC FILTER ARRAYS FOR THE NEAR INFRARED RANGE 70
6.1 FP filter arrays fabricated by the method using multiple spin coating 70
6.1.1 Fabrication process of FP filter with cavity structured by multiple spin coating process 71
6.1.2 Optical characterization of FP filter arrays fabricated by multiple spin coating method 73
6.1.3 Results and discussion 73
6.2 FP filter arrays fabricated by the method using hybrid cavity 75
6.2.1 Fabrication process of FP filters using the method using hybrid cavity for structuring cavity 76
6.2.2 Optical characterization of FP filter arrays using hybrid cavity........................77
6.2.3 Results and discussion 78
6.3 FP filter arrays fabricated by the method using novel resist mr-NIL210 80
6.3.1 Investigation of novel resist mr-NIL210 for SCIL process 81
6.3.2 Fabrication process of FP filter arrays using novel resist mr-NIL210 83
6.3.3 Optical characterization of FP filter arrays using novel resist mr-NIL210 84
6.3.4 Result and discussion..85
6.4 Characterization of the three FP filter fabrication methods of NIR FP filter arrays 86
6.4.1 Comparison of the technological effort for the three FP filter fabrication methods 86
6.4.2 Surface roughness in the heterostructure of cavity...87
6.4.3 Effect of high temperature during top DBR deposition 91

7. SUMMARY AND OUTLOOK..93
APPENDIX 96
Appendix A 96

Spin coating process of photoresist and polymers....96
Appendix B **98**
Thin Film deposition process by PECVD 98
Appendix C.... **99**
Process flow of master template fabrication using GaAs....99

LIST OF ABBREVATIONS....**100**
CHEMICAL ELEMENTS....**101**
BIBLIOGRAPHY **102**
PUBLICATION....**112**

1. Introduction and motivation

Despite of the development of sciences and technologies, humans are facing with a lot of problems, such as the quality of food, beverages and other agriculture products, which affect to the human's health, i.e. causing the diseases and therefore reducing the age average. It is happening in over the world, Asia, Europe and US. This is not only the challenge for social welfare system but also raises a big requirement of the developing of product authenticity and authentication technologies [1]. These requirements call for a on-line detection techniques which have the following advantages (i) assembled in the production line and carry out under the realistic environment, (ii) early detection of problem failures, (iii) permanent monitoring of the conditions and (iv) assessment of conditions at any desired time [2]. These advantages enable a possibility of detection the quality of raw materials and final products under steady process conditions. Considering the demands in practice, it is more necessary to develop a fast and efficient method to accomplish the product quality detection.

Optical spectroscopy [3], [4], [5] referring to the study of absorption and emission spectra of matter in the visible, near infrared (NIR) and ultraviolet (UV) spectral range, is a valuable measurement method. It has been extensively studied and widely applied in many fields such as in medicine, physics, chemistry, biology, space technology, process control, food and agriculture [6]–[23]. For many applications, low fabrication cost, high resolution and potential for strong miniature of the optical spectrometers, are crucial demands, especially for networked sensing systems. A lot of efforts from researcher, scientist and companies have been performing to miniaturize the spectrometers. However, previous approaches as the microfabrication of components followed by an

assembly is still strongly limited by the size and cost [24]. Optical micro-electro-mechanical system (MEMS) is more succesful approach [25], different types of MEMS-based microspectrometers have been developed including grating-based microspectrometer [26], [27], [28] and interferometer-based microspectrometer [29], [30], [31], [32]. Based on the MEMS technologies, Correia et al. proposed the idea to combine Fabry-Pérot filter arrays including 16 cavity heights and photodiodes to detect 16 cavity heights [29], then Wang et al. used the similar structure and broadened to detect 128 different wavelengths in the range of 722 – 880 nm [32]. However, the above-mentioned Fabry-Pérot based microspectrometers are still not cost efficient since it has to take at least N individual steps including lithography and etching process for 2^N different Fabry-Pérot filter cavities.

To overcome those issues mentioned above, in INA, we use a similar concept but replace the multiple deposition steps to generate various FP cavity heights by a single step: 3D nanoimprint, which enables the various cavity heights to differ from each other in the nm region. Since 3D nanoimprint is applied the device is called optical nanospectrometer [33], [34]. It consists of a static FP filter array and a corresponding detector array. All FP filters are using two identical dielectric Distributed Bragg Reflectors (DBRs) designed for a specific wavelength range. However, each filter reveals a different resonance cavity height (defined by the nanoimprinted polymer) in between and defines a different small spectral transmission band (called filter transmission line below). Up to now, the research in INA was focused on the visible spectral range between 460 nm and 700 nm involving corresponding cavity heights between 150 and 270 nm [34].

Each DBR consists of a periodic sequence of thin dielectric films with alternating high and low refractive indices. The optical thickness of each thin film in the DBR is a quarter of the design wavelength in the respective material. The DBR reveals a spectral range of high reflectivity (the so-called stop-band) and these two DBRs form a resonator and the space in between is called FP cavity. The thickness of each cavity is directly proportional to the corresponding spectral filter line for a considered cavity material for each individual filter. The UV-Substrate Conformal Imprint Lithography (SCIL), methodology uses hybrid templates, enables to generate 2D structures and was developed by Philips Research and Suss Mirco Tec. [35]. We were enlarging the SCIL methodology to 3D and very high resolution in the vertical direction. Thus, we are now able to apply 3D SCIL to fabricate different cavity heights in a single step [34] with high vertical resolution.

To address with our nanospectrometer in NIR spectral range, it is required to generate cavity heights in the range of 1 μm thickness using 3D nanoimprint. One of the main challenges is to produce the extended homogeneous cavities to address longer wavelengths in spectroscopy. The quality of cavity structures sensitively depends on the quality of the initially spin coated UV-Curable resin layers and the available viscosity of UV-Curable resin [36], [37]. Considering a distinct viscosity, the applied spinning frequency is limiting the resin layer thickness. High thicknesses require low spin frequency, however, low frequency will strongly degrade the homogeneity of resin layer and the quality of imprinted structures.

The main objective of this thesis is to find the solution to overcome the challenges mentioned above. Thus, the homogeneous extended cavities were designed and fabricated by three methods: (i) Using multiple spin coating of the

resin in order to obtain a thicker initial resin layer; (ii) using a "hybrid" cavity combining oxide layers and the UV-Curable resin to accumulate the required cavity heights and (iii) optimizing the nanoimprint process with a novel resin material. Another main objective of this thesis work is to apply those above-mentioned homogeneous extended cavity methods for fabrication of Fabry-Pérot filter arrays in NIR range.

This thesis comprises seven chapters:

- Chapter 1 introduces the background and motivation and outlines this thesis work.
- Chapter 2 presents the theoretical basics including the foundation of the Fabry-Pérot filter arrays and nanoimprint technology. Section 2.1 introduces the foundation of FP filter and its optical parameters, next the state of the Art of the FP filter based nanospectrometers is introduced in section 2.2, the foundation of nanoimprint technology is presented in section 2.3 comprised of various nanoimprint methods and resist materials.
- Chapter 3 deals with foundation of the implemented technological process. This chapter introduces the main fabrication and characterization technology for FP filters, including the deposition and patterning methods (section 3.1) and applied characterization methods (section 3.2).
- Chapter 4 presents the design, simulation and fabrication of NIR FP filters. The FP filters were first designed with different cavity structure methods (section 5.1), then they are simulated by OpenFilters software (section 5.2) and the simulated results are discussed in section 5.3. Finally, the fabrication steps of NIR FP filters are presented in section 5.4.

- Chapter 5 reports the work of fabrication and characterization of the master templates for NIR. The fabrication process was first review in section 5.1, then the results are discussed in section 5.2. Next, the soft stamps replicated from master template for SCIL process are presented in section 5.3.
- Chapter 6 presents the works of fabrication and characterization of FP filter arrays for NIR. Each method corresponded with each cavity structure design is reported in section 6.1 – 6.3. Section 6.4 deals with the characterization of three FP filter fabrication methods, including the comparison of technological effort in fabrication of FP filter arrays by three methods and reports the surface roughness problem in cavity structure and the effect of high temperature on cavity layer during fabrication process.
- Chapter 7 sums up the achievements of this thesis work, opening new questions to guide future work on the topic of fabrication NIR Fabry-Pérot filter arrays.

2. Theoretical basics

2.1. Foundation of Fabry-Pérot filter and its optical parameters

The FP filter was first demonstrated in 1897 by Charles Fabry and Alfred Pérot at the University of Marseille [38]. Their discovery was a result from work primarily conducted in the field of electricity and the necessary in this field for precise measurements of small distances.

The FP filter is an optical resonator that confines and stores light energy at selected frequencies. This optical transmission system incorporates feedback, whereby the light is repeatedly reflected within the system and thus circulates without escaping the system. A standard FP filter comprises of two parallel, highly refractive mirrors and a cavity formed between them. In this chapter we will discuss about the Distributed Bragg Reflectors (DBRs) which implements as highly reflected mirrors and afterwards are the theory of FP filter and its optical parameters.

2.1.1 Distributed Bragg Reflectors (DBRs)

A DBR consists of two materials with different refractive indices, i.e. high and low, and each set of two layers is called period. The thickness of each layer is $\lambda_0/(4n)$, where λ_0 is the desired center wavelength and n is the refractive index [39]. When the light beam passes through the DBR, the beam reflected within high refractive index layer experiences no phase shift. Therefore, all the incident beams which are reflected at successive boundary layers, reappear all in phase at the front surface and they contribute constructively interference [40].

The reflectivity of the mirror can be defined from the equation 2.1 [40]:

$$R \cong 1 - 4\left(\frac{n_L}{n_H}\right)^{2p} \frac{n_s}{n_A} \quad (2.1)$$

Where R is the reflectivity of the mirror, p is the number of period; and n_L, n_H, n_S, n_A are the low, high, substrate and air refractive indices respectively.

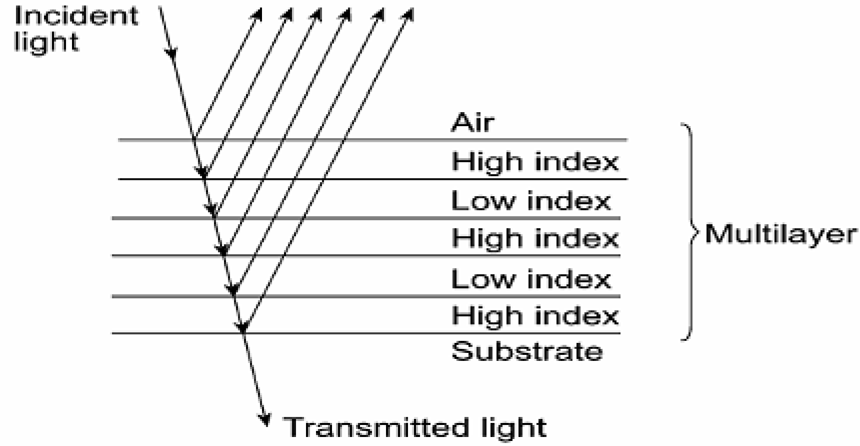

Fig. 2.1 Structure of Distributed Bragg Reflector (DBR) [39]

The equation (2.1) shows that, the higher number of periods the higher reflectivity. In the Fig. 2.2 shows the different reflectivity of DBR varied to the number of periods. Moreover, from the equation (2.1), the higher differences in refractive index of the DBR layers have high reflectivity with small number of periods. That we can see in case of using InP/air DBR (refractive indices for InP and air are 4.5 and 1 respectively), only 2.5 periods of InP/air achieves a reflectivity larger than 99.5% [41], which needs at least 15.5 periods to achieve in case of using Si_3N_4/SiO_2 as shown in Fig. 2.2.

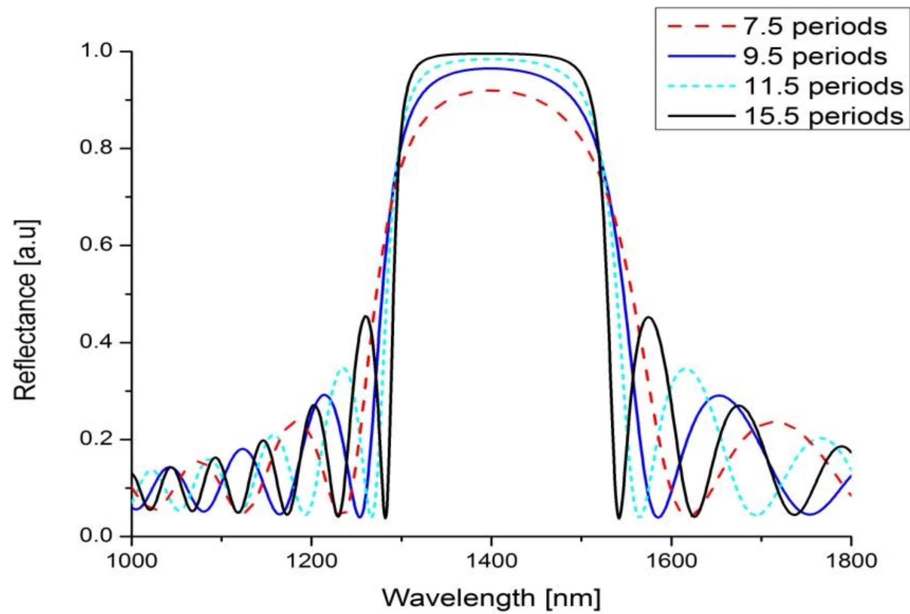

Fig. 2.2 Reflectivity of DBR with different period numbers. The reflectivity of DBR is directly proportional with the number of periods.

2.1.2 Fabry-Pérot Filter

A FP filter consists of two DBRs which separated by a distance d, forming an optical resonance cavity as shown in Fig. 2.3. It is called the interferometer when d is variable and etalon when d is fixed. The filters are characterized by constructive and destructive interference of waves in the resonance cavities.

Fig. 2.3 shows the plane waves reflected between two parallel surfaces P_1 and P_2, with distance d and n is the refractive index of the interspace. The transmission and reflection amplitude coefficient of the incident beam which travels from left to right is denoted with label $^+$, and label ' for those from the beam that comes from the right to left.

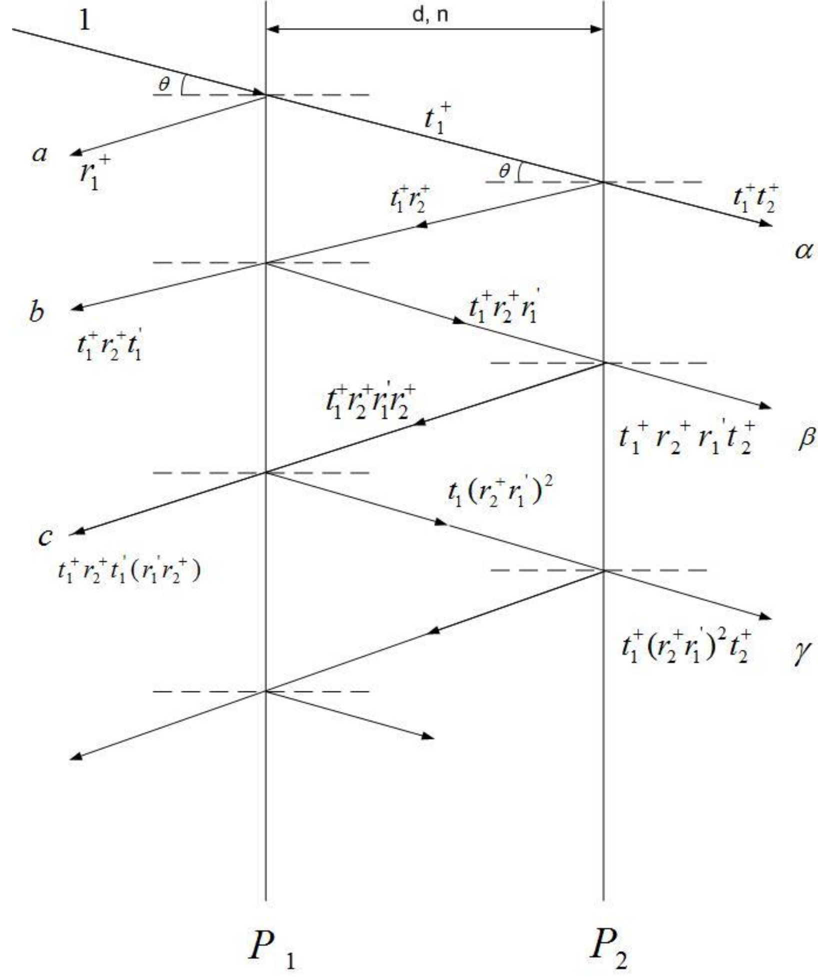

Fig. 2.3. Multiple reflection of plane waves between two plane P1 and P2 parallel surfaces. The amplitude coefficients of the reflected set of beams denote as a,b,c and the transmitted beams as α, β, γ [42]

φ is the phase lag of the phase difference due to distinct path lengths for each beam at the output light beam. φ is defined as [42]:

$$\varphi = \frac{4\pi n d cos\theta}{\lambda} \tag{2.2}$$

If the first m transmitted beams are superposed, the amplitude $E_t(m)$ of the resultant electric vector of transmitted light is given by:

$$E_t(m) \qquad = t_1^+ t_2^+ [1 + r_1^{'} r_2^+ e^{i\varphi} + \cdots + \left(r_1^{'} r_2^+\right)^{m-1} e^{i(m-1)\varphi}]$$

$$= t_1^+ t_2^+ [1 - \left(r_1^{'} r_2^+\right)^m e^{im\varphi} / (1 - r_1^{'} r_2^+ e^{i\varphi}] \tag{2.3}$$

For an infinite number of beams as m →∞ this becomes:

$$E_t \rightarrow E_t(\infty) = t_1^+ t_2^+ / (1 - r_1^{'} r_2^+ e^{i\varphi}) \tag{2.4}$$

The corresponding transmitted I_t can be described as:

$$I_t = |t_1^+ t_2^+|^2 / (1 + \left|r_1^{'} r_2^+\right|^2 - 2|r_1^{'} r_2^+| cos\psi \tag{2.5}$$

With ψ= φ + ϵ (2.6)

ϵ is the correction for phase change. For a single surface, we have R and T as the surface intensity reflection and transmission coefficient, and:

$$t^+ t^{'} = T; r^+ = -r^{'}; r^{+^2} = r^{,2} = R; \text{R+T} = 1 \tag{2.7}$$

For the ideal dielectrics we have: $\epsilon = 0$, and $t_2^+ = t_1^{'}$ and $r_2^+ = r_1^{'}$, therefore, the energy transmission coefficient for the pair of surfaces becomes:

$$I_T = \frac{T^2}{1 + R^2 - 2Rcos\varphi} \tag{2.8a}$$

$$= T^2 / [(1 - R^2) + 4Rsin^2(\frac{\varphi}{2})] \tag{2.8b}$$

$$= \frac{T^2}{(1 - R)^2} (\frac{1}{1 + \left[\frac{4R}{(1 - R)^2}\right] sin^2(\frac{\varphi}{2})} \tag{2.8c}$$

$$= [T/(1 - R)]^2 \left[1 + Nsin^2\left(\frac{\varphi}{2}\right)\right]^{-1} \tag{2.8d}$$

$$= \left[\frac{T}{1 - R}\right]^2 A(\varphi) \tag{2.8e}$$

Where N is equal to $\frac{4R}{(1-R)^2}$. Equation (2.8e) is known as basic Airy formulas for transmission and A(φ) is the Airy shape function [42]. The energy reflection coefficient is given:

$$I_R = Nsin^2\left(\frac{\varphi}{2}\right)[1 + Nsin\left(\frac{\varphi}{2}\right)]^{-1} \quad (2.9)$$

In case R + T = 1 with no surface absorption, the energy transmission and reflection coefficients are complementary and equal to:

$$I_R + I_T = [T^2/(1-R)^2 + Nsin^2(\frac{\varphi}{2})]/[1 + Gsin^2\left(\frac{\varphi}{2}\right)]^{-1} \quad (2.10)$$

When φ equal to 2mπ then the maximum transmission will emerge:

$$\varphi = \frac{4\pi dcos\theta}{\lambda} = 2m\pi \quad (2.11)$$

This maxima or transmission peak can be expressed in frequency domain as:

$$f_m = m\left(\frac{c}{2ndcos\theta}\right) \quad (2.12a)$$

$$= m(FSR) \quad (2.13b)$$

Where FSR is the free spectral range, which is the distance between two adjacent transmission peaks. This FSR depends only on the optical path length if the light incidents normal to the etalon.

For the normal incidence light and an air gap cavity (n=1), the FSR is defined as:

$$FSR = \frac{c}{2d} \quad (2.14)$$

Where d is the distance between two mirrors, m is an integer, λ represents the resonant wavelength in the interferometer, and c is the speed of light in a vacuum.

2.1.3 Optical parameters of FP filters

There are some important optical parameters which have to consider when characterize FP filters such as: The Full Width Half Maximum (FWHM), the Resolving Power ($\Re$), and the Finesse ($\mathcal{F}$).

The first parameter, FWHM, is the separation between the points on either side of a maximum where the intensity has fallen to half the maximum value. FWHM is defined as:

$$FWHM = \frac{\lambda^2(1-R)}{2\pi d\sqrt{R}} \tag{2.15}$$

The FWHM of the filter at a given wavelength determines the resolving power which is the second interested parameter:

$$\Re = \frac{\lambda}{FWHM} \tag{2.16}$$

For a feasible FP filter used in optical spectroscopy, it is required a small enough of FWHM to resolve the spectrum. The FSR, in contrast, has to large enough to avoid overlap of different filter transmission lines.

The Finesse ($\mathcal{F}$) is defined as the ratio of FSR and FWHM, replace FWHM from (2.13) and the corresponding FSR value from (2.12) in vacuum is $FSR = \lambda^2/2d$ [43].

$$\mathcal{F} = \frac{\mathrm{FSR}}{\mathrm{FWHM}} = \frac{\pi\sqrt{\mathrm{R}}}{1-\mathrm{R}} \tag{2.17}$$

From the equation (2.17), the finesse, i.e. the resolution of a FP filter only depends on the reflectance of the mirrors.

2.2 State of the Art: Fabry-Pérot Filter based nanospectrometers

Nowadays people all over the world is daily facing with a lot of problems which is affected to their health and therefore reducing the average age. It is happening in over the world and become a big challenge for not only social welfare system but also raises a big demand of developing of heath care technologies.

Based on the urgent requirement mentioned above, the optical spectrometer has been invented and widely used in many fields like medicine, physics, chemistry, biology, space technology, process control, food and agriculture [6]–[23]. For many applications, low fabrication cost, high resolution and potential for strong miniature of the optical spectrometers are crucial demands, especially for network sensing systems. A lot of efforts from researcher, scientist and companies have been performing to miniaturize spectrometers. Many approaches have been proposed to solve this drawback. However these conventional spectrometers are still limited in size and cost [24]. Optical micro-electro-mechanical system (MEMS) [25] is a potential approach, different types of MEMS-based microspectrometers have been developed including grating-based microspectrometer [26]–[28] and interferometer-based microspectrometer [29]–[32]. Based on MEMS technologies, Correia et al. proposed the idea to combine Fabry-Pérot filter arrays including 16 cavity heights and photodiodes to detect 16 cavity heights [29], then Wang et al. used similar structure and broadened to detect 128 different wavelengths in the range of 722-880 nm [32]. However, the above-mentioned Fabry-Pérot based microspectrometers are still not cost efficient since it has to take at least N individual steps including lithography and etching process for 2^N different Fabry-Pérot filter cavities. Other approach from Emadi et al. for fabricating a linear variable microspectrometer with slope cavity based on photoresist reflow and further dry etching is also not cost efficient and the practical resolution of this microspectrometer is doubtful [44].

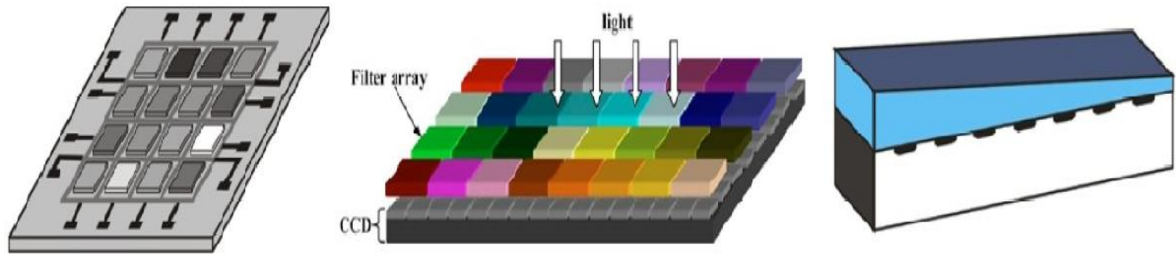

Fig. 2.4 Schematic of a Fabry-Pérot-based microspectrometer: Correia et al., 16 channels on a single chip CMOS, the lateral dimension is 4.7 mm x 4.7 mm [45] (left); Wang et al., 128 channels on a CCD, 12 mm x 12 mm x 5 mm [32] (middle); Emadi et al., more than 20 channels on a CCD [44] (right).

In order to solve the above-mentioned drawback and maintaining the outstanding advantages of the FP filter structure, a novel methodology of fabrication the miniaturized FP filter based spectrometers using nanoimprint technology is developed and introduced at INA [34], [46]–[50], [48]. In this method, we use a similar concept but replace the multiple deposition steps to generate various FP cavity heights by a single step: 3D nanoimprint, which enables the various cavity heights to differ from each other in nm region. Since 3D nanoimprint is applied the device is called optical nanospectrometer [33],[34]. It consists of a static FP filter array and a corresponding detector array. All FP filters are using two identical dielectric Distributed Bragg Reflectors (DBRs) designed for a specific wavelength. However, each filter reveals a different resonance cavity height (defined by the nanoimprinted polymer) in between and defines a different small spectral transmission band.

2.3 Foundation of nanoimprint technology

2.3.1 Introduction of nanoimprint

Nanoimprint lithography was first introduced in 1996 by Chou. et al. [51] as a low cost, high throughput and high resolution. Nanoimprint lithography is used to fabricate nanometer scale pattern.

The principle of imprint lithography can be described in two steps. First, a mold with nanostructures on its surface is pressed into a thin resist coated on a substrate. After curing, the imprint mold is released from the layer. As a result, the nanopatterns are transferred on the layer.

2.3.2 Classification of nanoimprint lithography methods

Since 1995, nanoimprint lithography has developed with different methods. However, its fundamental principle is the same. Fist, a substrate is coated with a polymer layer or functional layer, and the stamp is pressed into the polymer layer. The imprint mold is released from layer after curing. Consequently, the structures are transferred on the layer.

The nanoimprint technology can mainly be summarized in hot embossing lithography, UV lithography, and soft lithography. Different soft lithography has been proposed, such as micro contact printing (μCP) [52], [53], [54], [55], replica molding (REM) [56], [57][58]. Depending on the kind of stamp, hard nanoimprint [59]and soft nanoimprint [60], [61], [62] are defined .

The classification of nanoimprint lithography is showed in Fig. 2.5 below:

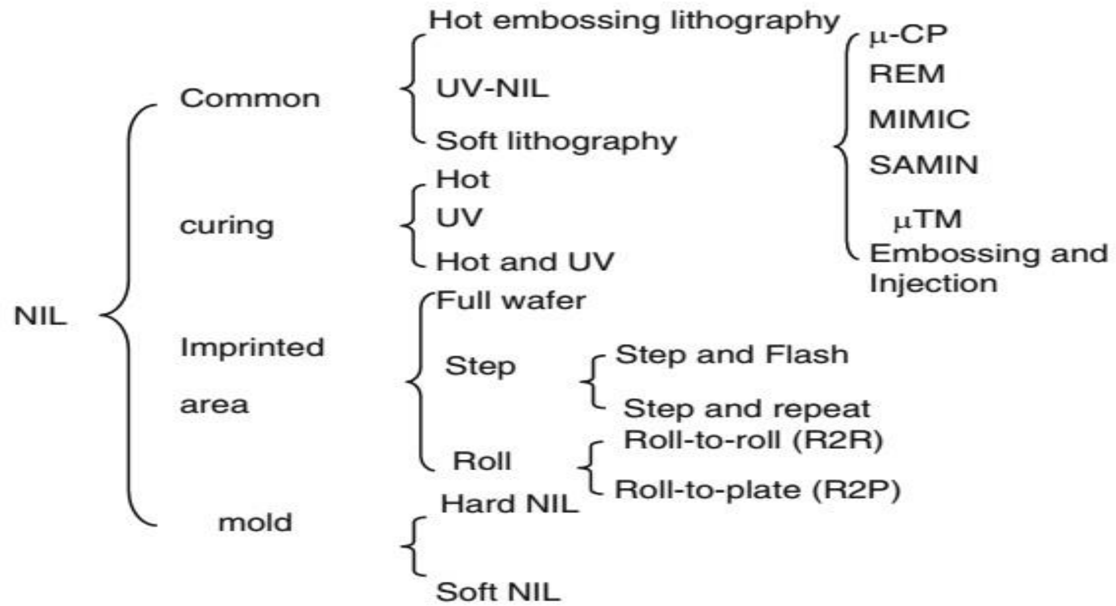

Fig. 2.5 Classification of nanoimprint lithography, original figure from [63]

2.3.3 Nanoimprint methods

As mentioned above, different nanoimprint methods have been proposed, in this section the thermal nanoimprint, UV nanoimprint, soft nanoimprint and UV Substrate Conformal Imprint Lithography (UV-SCIL) will be summarized.

2.3.3.1 Thermal nanoimprint lithography

Thermal or hot embossing was first introduced by Chou's group [64]. In this method, a thin film is spin-coated on the substrate, then the stamp is brought into contact with the surface of the thin film under certain pressure. At the same time, the polymer is heated up above the glass transition temperature; afterwards the patterns on the mold are pressed into the softened polymer film. The stamp and polymer are separated after cooling and pattern resist is left on the substrate. During this process, the residual layer is unavoidable; it can be removed by plasma process (reactive ion etching).

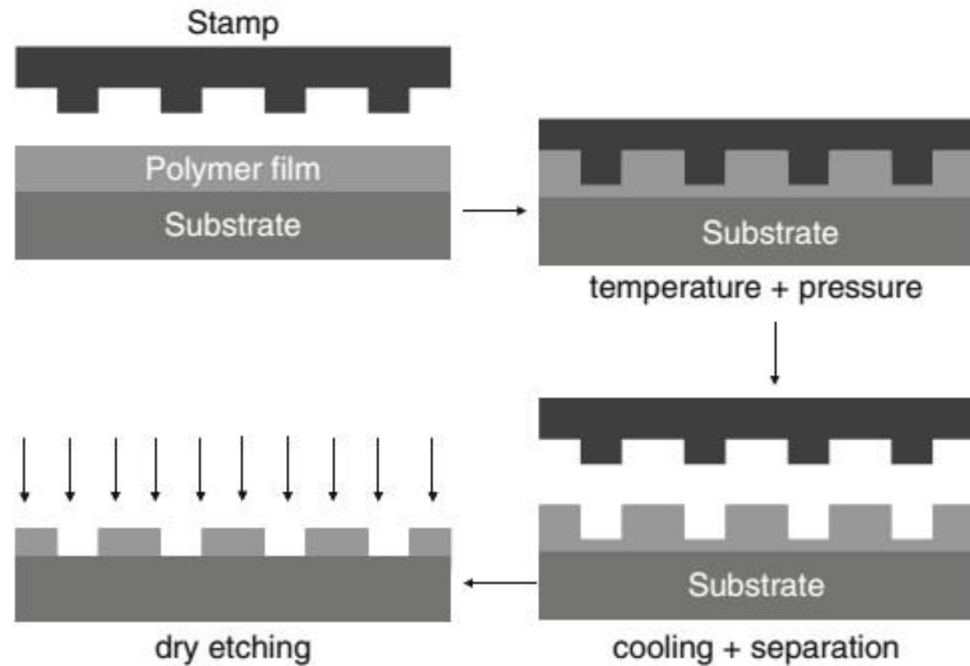

Fig. 2.6 Schematics of the thermal nanoimprint lithography process, original figure from [63]

In the thermal process, it is required high pressure (50-100 bar) to full fill the cavity of the stamp. Therefore, the stamp material is with high mechanical strength. Si, SiO_2, Si_3N_4, diamond, or metal are used as the stamp material.

During the thermal nanoimprint, not only imprint resist is heated but also the templates, it leads to distortion of imprint structures. On the other hand, heating and cooling process will take longer time than other nanoimprint technology that work at room temperature.

2.3.3.2 UV nanoimprint lithography

In this method, a transparent stamp is used for imprinting a pattern on the UV Curable film and later on cured by UV exposure.

When compared with the thermal nanoimprint method, the viscosity for the UV-NIL is much smaller and the stamp is transparent to UV light. Moreover, UV-

NIL work at room temperature and has lower applied pressure and alignment for IC devices.

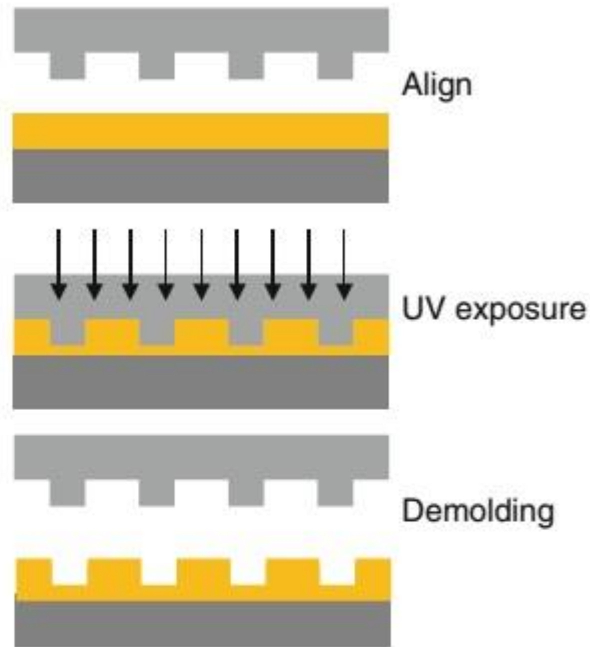

Fig. 2.7 Schematic of UV-NIL: imprint resist is coated on the substrate and align; the stamp is imprinted into the resist, and UV curing is applied; separation of the stamp and the substrate, original figure from [63]

There are two options for the stamp of UV-NIL, it could be either hard material (quartz) or soft polymer material (PDMS). In case of soft stamp, named soft UV-NIL [65], it can bring into conformal contact with a rough surface and satisfy with large area imprint surface [66]

2.3.3.3 Soft nanoimprint lithography

Soft nanoimprint can replicate micro/nanostructure by template/master made out of an elastic, deformable material (soft material). This method was first proposed by Whiteside from Harvard university [54]. It includes three basic steps:

- Mother template fabrication.

- A copy of a deformable material stamp (daughter stamp) is formed from a mother stamp. Usually, PDMS polymer is used as soft material.
- Imprint pattern with the daughter stamp.

Thanks to the soft and flexible stamp, the soft nanoimprint lithography can reduce the damage of template during imprinting caused by the contaminations such as particle on the substrate [67], [58], which is unavoidable with rigid stamps.

Different soft nanoimprint has been proposed and realized, such as microcontact printing (μCP), replica molding (REM), microtransfer moding (μTM), and nanotransfer lithography (nTP).

2.3.3.4 UV Substrate Conformal Imprint Lithography (UV-SCIL)

UV-SCIL uses hybrid stamps, enables to generate 2D structures and was developed by Philips Research and Suss Micro Tech. [68]. This methodology provides patterning of sub-50 nm structures over large areas at very low pressure. The UV-SCIL process is based on the transfer of patterns from hybrid Polydimethylsiloxane (PDMS) stamp into UV-curable resists.

Fig 2.8 shows the UV-SCIL process: the SCIL stamp is first brought into contact with the imprint resist on the substrate sequentially by releasing the vacuum in the grooves step by step. This sequential contact helps to prevent the stamp from air bubble trapping. The capillary forces help to fill the structures at very low pressure 20 mBar. As the sequential contact is done over the entire substrate and the structures are imprinted on the resist, then UV-exposure is applied to cure and harden the structures. Finally, the SCIL stamp is separated from the substrate by switching on the vacuum in the grooves in the opposite way to the imprint process.

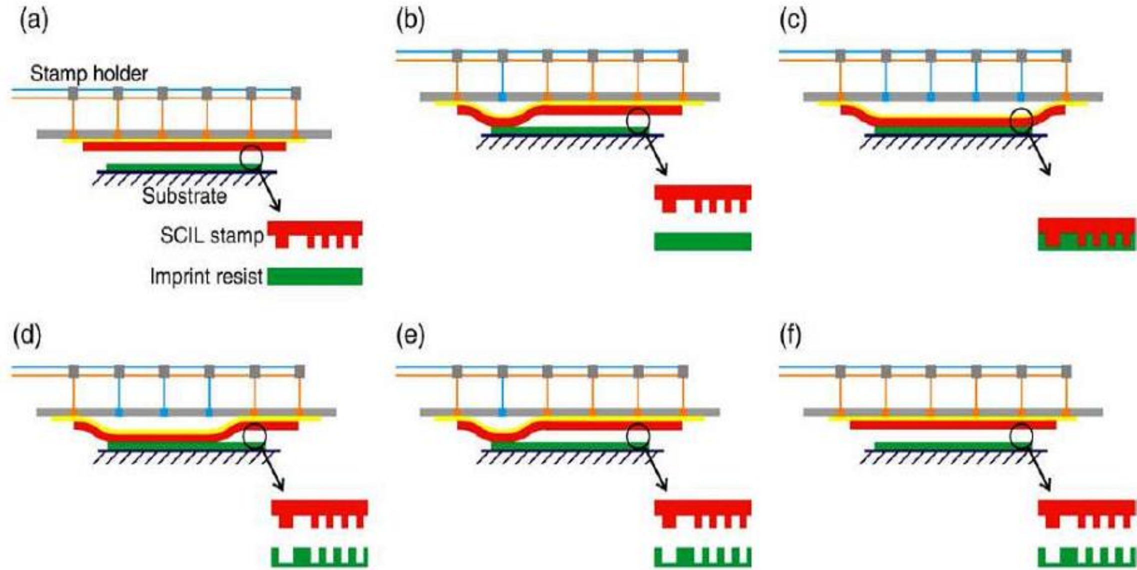

Fig. 2.8 Schematic description of SCIL imprint and separation sequences [58]: (a) the SCIL stamp is fixed on the holder by vacuum; (b) the sequential imprint process starts by releasing vacuum step by step; (c) the imprint process is completed by releasing vacuum in the grooves over the entire substrate; (d) the separation of stamp and substrate takes place in a sequential manner after the curing time is over; (e) and (f) the separation is completed when all the vacuum grooves are switched on.

2.3.4 Nanoimprint resists materials

The nanoimprint resists require some properties such as a sufficiently low viscosity during imprinting and adequate mechanical strength after curing. A sufficiently low viscosity resists guaranties for full filling in all the patterns of the stamp during the imprinting process. The mechanical strength of cured resists is important for the stamp releasing process.

Two kinds of nanoimprint resists are most used in nanoimprint lithography. They are thermal resist and UV-Curable resist. For thermal resist such as Polymethylmethacrylate (PMMA) and Polystyrene (PS) [69], the glass transition temperature (T_g) is the most important parameter. Too high T_g needs longer

heating and cooling time during thermal nanoimprint process, while too low T_g leads to relaxation.

The resist used in this thesis work is UV-Curable resist: mr-UVCur06 has viscosity around 15 mPas and mr-NIL210 has viscosity around 2 Pas. Both products come from Micro resist technology GmbH. These resists can work at room temperature and adapt the SCIL process: fast curing, low shrinkage and less deformation.

3. Relevant technological process

3.1 Foundations of deposition and patterning methods

3.1.1 Basics of Plasma enhanced chemical vapor deposition (PECVD)

3.1.1.1 Chemical Vapor Deposition (CVD)

Chemical vapor deposition (CVD) is the process of chemically reacting volatile compound of a material to be deposited with other gases to produce a non-volatile solid that deposit atomistically on a suitable placed substrate. CVD is a chemical process which transforms gaseous molecules, called the precursors into a solid material in the form of thin film or powder, on the surface of substrates.

CVD is used mainly to deposit monocrystalline, polycrystalline, amorphous and epitaxial layer of materials. These materials include: polysilicon, silicon oxides and nitrides.

CVD is classified based on the basis by which chemical reactions are initiated (e.g., activation process) and process conditions: Atmospheric pressure CVD (APCVD)- CVD processes at atmospheric pressure; Low-pressure CVD (LPVCD)- CVD processes at sub atmospheric pressure; and Plasma enhanced CVD (PECVD)- CVD processes that utilize plasma to enhance chemical reaction rates of the precursors.

3.1.1.2 Plasma enhanced chemical vapor deposition (PECVD)

Plasma-enhanced deposition processing is done using electric discharge plasmas in which the energy sustains the ionized state is supplied by an externally applied electric field. Most of the applications involve the use of low pressure (glow discharge) plasmas. The energetic species in these plasmas are the free electrons. They gain energy from the electric field faster than the ions do and are thermally

isolated from the atoms and molecules as far as elastic collisions are concerned, by the mass difference. Consequently, the electrons accumulated sufficient kinetic energy to undergo inelastic collisions and to sustain the ionization, while the heavy particle (molecule) temperature remains low.

Plasma is designed as an ionized gas. It requires low temperatures, which is often critical in the manufacture of semiconductors, and is mainly used for the deposition of dielectric and passivation films like silicon oxide or nitride or Oxide-Nitride-Oxide (ONO) layers.

Compare with APCVD and LPCVD, PECVD has some advantages such as: low operation temperature; lower chances of cracking deposited layer; good dielectric properties of deposited layer; good step coverage and less temperature dependent.

The schematic layout of the system is shown in Fig. 3.1. In the deposition chamber, a temperature controlled grounded electrode is used to hold the substrate and can heat the substrate up to 400ºC. A strong electric field is applied between a second electrode and the holder which excites the gas molecules present in between and causes the plasma ignition. The generated radicals react on the surface to create amorphous films. The system is driven by a low and a high frequency generator applied between the two parallel electrodes. The high frequency generator is matched to the chamber through an automatic matching unit (AMU) The duty cycle (the time ratio between the high and the low frequency during the deposition process) of the plasma excitation frequency is varied during the process by an automatic switching unit (SWI). Three mass flow controllers (MFC) ensure precise proportioning of the reactive gases. A root and a dual stage rotary pump is used to remove the radicals and ions that do not contribute to the deposition.

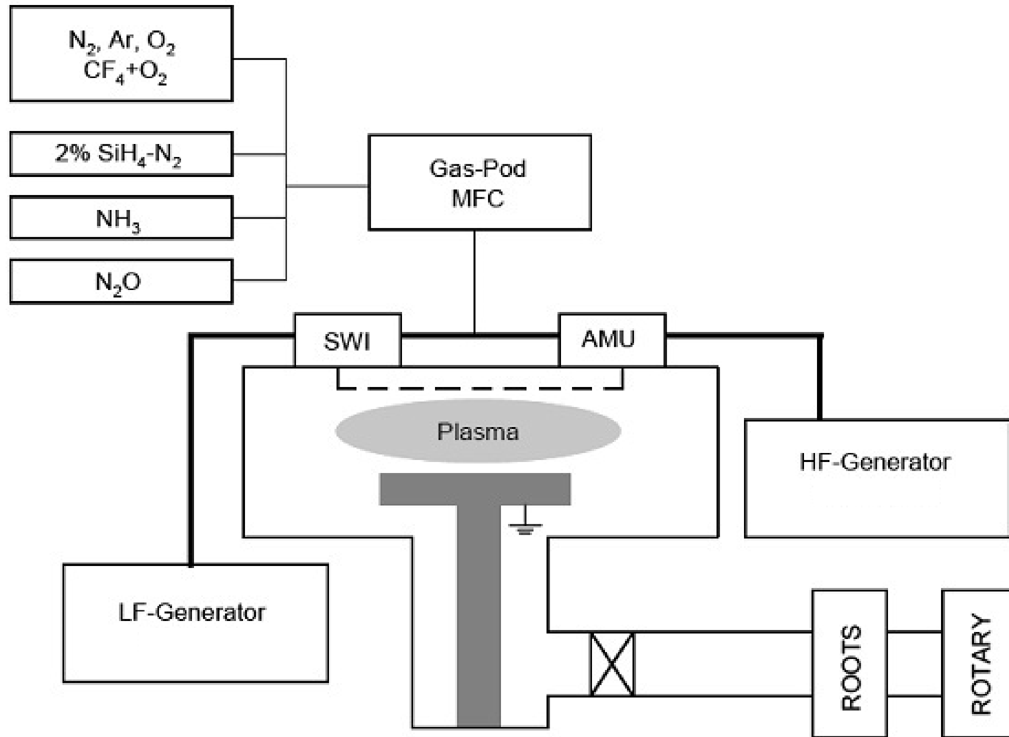

Fig. 3.1 Configuration of the plasma enhanced chemical vapor deposition (PECVD) machine used (Plasma Lab 80 Plus, Oxford Instruments) [70]

Two percent silane (SiH_4) diluted in nitrogen (N_2) and ammoniac (NH_3) are used for silicon nitride (Eq. 3.1) whereas silicon dioxide (SiO_2) results from the same silane and nitrous oxide (N_2), (Eq. 3.2)

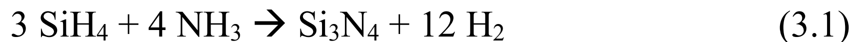

$$3\ SiH_4 + 4\ NH_3 \rightarrow Si_3N_4 + 12\ H_2 \qquad (3.1)$$

$$SiH_4 + 2\ N_2O \rightarrow SiO_2 + 2\ N_2 + 2\ H_2 \qquad (3.2)$$

Other process gases like nitrogen (N_2), Argon (Ar), Oxygen (O_2) and a cleaning gas like carbon tetrafluoride with oxygen ($CF_4 + O_2$) are also available.

3.1.2 Basics of Ion beam sputtering deposition (IBSD)

IBSD is used to deposit metals and their oxides. Metal atoms are knocked out or sputtered from a metal surface using an ion beam and are then accelerated towards the substrate where they are deposited on top of the substrate. For metal

oxides, oxygen gas is released into the chamber where it reacts with the knocked out metal atoms forming oxides which are then deposited on the substrate surface.

IBSD is used to deposit oxide layer such as Titanium dioxide, Silicon dioxide, Niobium dioxide, etc. Layers deposited by this technology have better optical properties compared to PECVD. This is due to the absence of hydrogen inside the chamber during deposition as well as slow deposition rates of IBSD resulting in much better cohesion between deposited layers. This is because of deposition rate does not depend on gas flow but on sputtering rate of the material which is relatively constant.

Fig. 3.2 shows the IBSD system, it uses Ion Beam Source 1 (IBS1), usually heavy ions of noble gases (e.g. Argon or Xenon) for plasma generation. The positively charged Argon ions are accelerated towards the target material where the ions transfer their energy to the target atoms. This energy is more than the lattice energy of the atoms. Thus, the atoms are ejected from the target and move towards the substrate. In order to deposit oxides, IBS2 is used. The entire process takes place under high vacuum.

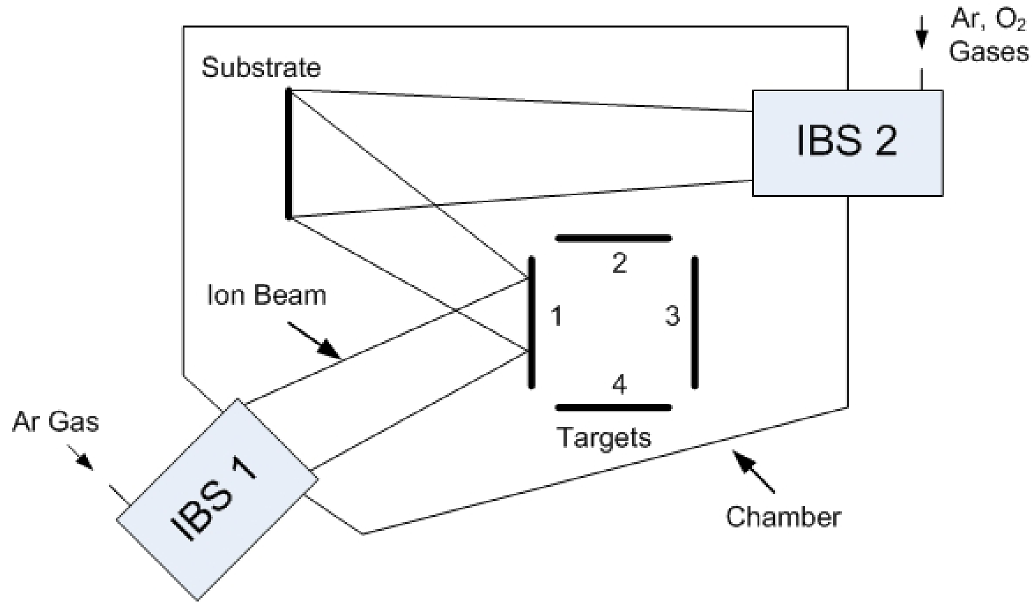

Fig. 3.2 Schematic view of an IBSD system, redraw from [71]

3.1.3 Basics of photolithography

3.1.3.1 Principle of photolithography

Photolithography is a process in which the patterns are transferred from the mask to the thin coat of photosensitive material covering the surface of a wafer. These patterns represent several regions in an integrated circuit such as implementation regions, contact windows and the bonding pad areas. These patterns are just the temporary features on the resist, in order to get the circuit features, these patterns must be transferred into the underlying layers of the device with the help of etching [72], [73], [74]

Photolithography process should be carried out in clean room environment, it is because of the fact that dust particles in the air can stay on the wafer or template and can cause defects in the circuit features [75].

3.1.3.2 Exposure tools

The performance of an exposure tool depends on three parameters, i.e. resolution, registration and throughput.

- Resolution is the minimum feature dimension that can be transferred with the high reliability on the photoresist.
- Registration is concerned with the measure that how precisely patterns on a successive mask can be aligned with respect to formerly defined patterns on the wafer.
- Throughput depends on the numbers of wafer that can be exposed per unit time for a given mask level.

There are many lithographic techniques e.g. UV lithography, extreme UV lithography, X-Ray lithography, electron beam lithography and nanoimprint lithography. The main difference between these techniques is the resolution limit [76].

3.1.3.3 Radiation sources

Power and radiance are the two major things which can play an important role in the source with which exposure is being done:

- Power: the total power required to have a perfect exposure depends upon the sensitivity of the resist and the time for which exposure is being done.
- Radiance is the amount of power that can be focused on the resist and is given as power density per steradian.

For a good exposure, it is required that the power and the radiance must be as high as possible and this can be achieved with the help of a high pressure Mercury-Xenon arc lamp.

3.1.3.4 Photomask

The binary masks were used for the photolithography. These masks produce patterns of opaque and transmissivity features on the resist. Binary masks are produced with the help of the chrome coating on fused silica substrate. One disadvantage of the binary mask is that the smallest feature size is effected by the diffraction and interference effect and this problem can effect to the reproducibility of the binary mask. Shift masks are used to overcome this drawback and can achieve feature size of 65nm and below. The advantage of using the phase shift mask is that it can suppress the diffraction effect with the help of the phase and interference effect [77].

3.1.3.5 Photoresist

Photoresist [78] is considered as the radiation sensitive compounds that can be categorized in two types: positive or negative photoresist.

- Positive photoresist: in this type of resist, the UV exposed parts become more soluble in the developer and are removed. Before exposure the photosensitive compound is unsolvable in the developer solution, but after exposure it has ability to absorb radiations in the exposed patterns [75]. This helps in changing its chemical structure which becomes soluble in the developer solution and after development the exposed areas are removed as shown in Fig. 3.3.
- Negative photoresist: in this resist, the exposed regions become less soluble in the developer and it creates the reverse patterns on the photoresist as found on the mask. It is because of the negative photoresist causes a polymer cross-linking due to chemical reaction after exposure. This cross-linked polymer has higher molecular weight

and become insoluble in the developer [75]. As the result, the unexposed parts are removed after development as shown in Fig. 3.3.

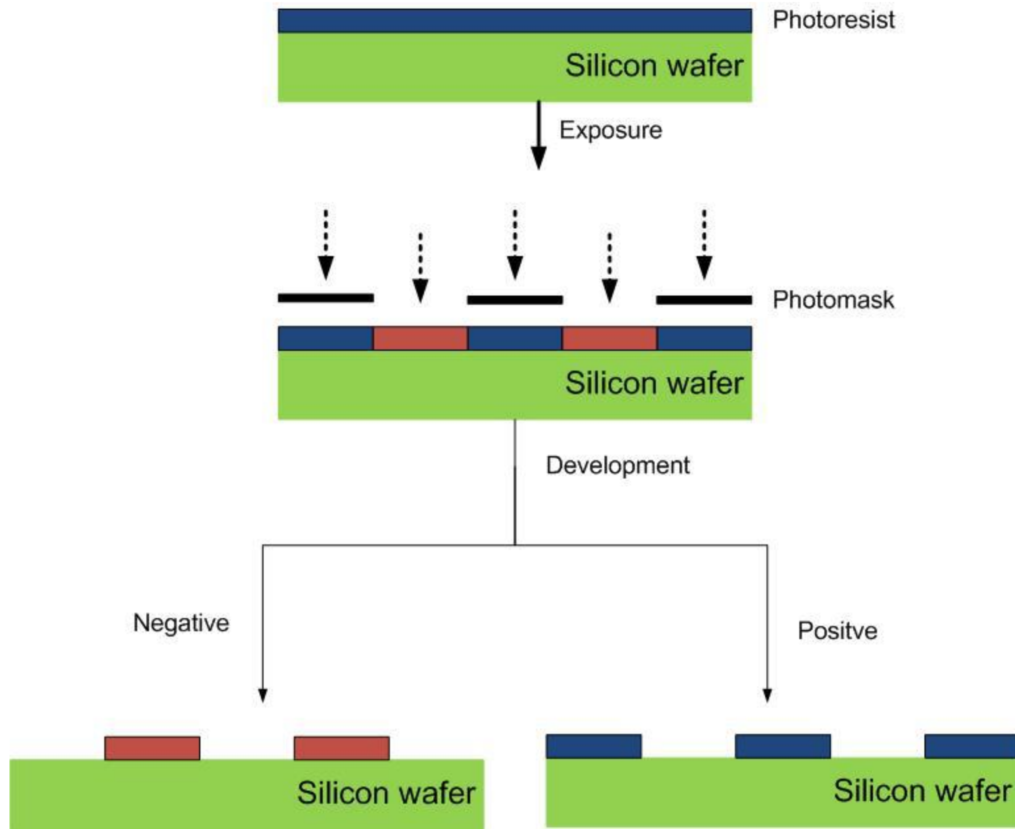

Fig. 3.3 Demonstration of positive and negative photoresist

3.1.4 Basics of dry-etching

Etching [72], [74] is the removing process for the unmasked parts of the substrate. There are many kinds of etching: isotropic and anisotropic etching, wet and dry etching, chemical and physical etching.

Dry etching [73] is the process in which the ions produced from plasma process are used as etcher. Inert gases such as Argon are used in ion etching and ion beam etching, which are considered as a pure physical etching process. The chemical plasma etching process can be performed using reactive ions in reactive ion etching and reactive ion beam etching to achieve deep etching.

Reactive ion etching (RIE)

Reactive ion etching (RIE) [79], [70] is an etching technique used to control the dimension etching of small geometries with the help of chemically reactive plasma which removes the material of wafer. RIE is a type of dry etching and applied for fabrication of microstructures. RIE combines the characteristics of pure chemical etching and pure physical etching by offering anisotropic etching property of pure chemical etching, high selectivity and etching rate of pure physical etching.

Fig. 3.4 shows a typical parallel plate reactor of a RIE system. Two parallel electrodes create the electric field. The mass flow controller (MFC) is used to control and mix the process gases which are injected into the chamber via gas inlet on the top electrode. The radio frequency 13.5 MHz is applied between the electrodes to ionize the process gases and generate the plasma (including charged ions, free electrons and neutral radicals). The electric field generated DC bias between electrodes accelerates the ions towards the surface of the substrate. In case of using inert gases, physical etching (sputtering) takes place and the substrate surface is knocked down since the high kinetic energy of the accelerated ions.

The RIE system using in this thesis work for fabrication master template is Oxford Plasmalab 80+ which is connected with H_2, CH_4, Argon and O_2.

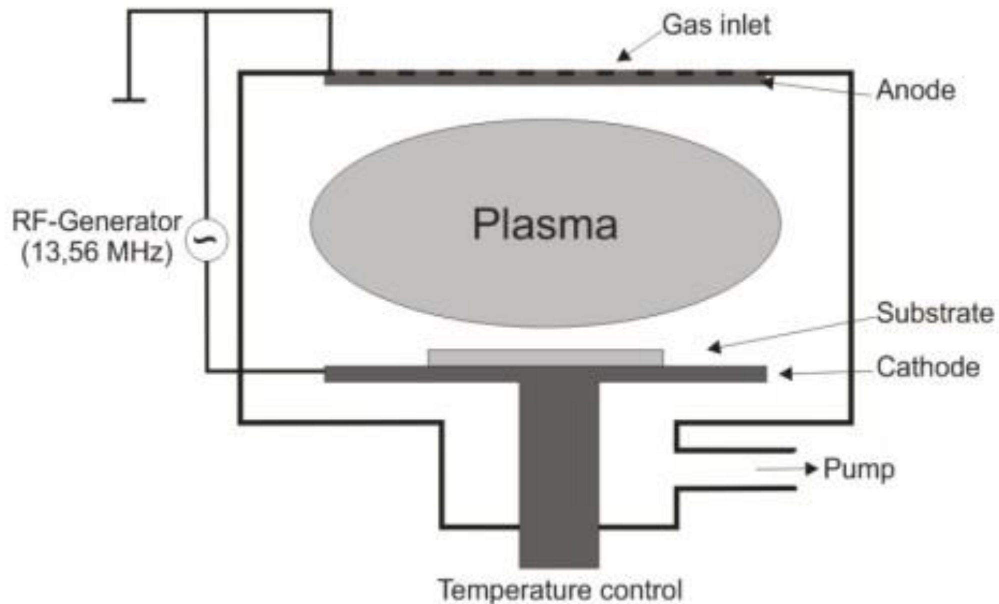

Fig. 3.4 Schematic of reactive ion etching system, original figure from [80]

3.1.5 Basics of lift off process

Besides wet or dry etching, lift-off is a common technique to pattern metal or dielectrically films in the µm or sub-µm range. The main criteria for the choice of a photoresist best-suited for a certain lift-off process are:

- The thickness of the coated material.
- The coating technology (evaporation, sputtering, VCD, etc.) and the maximum temperature the resist film has to stand during coating.
- The required resolution.
- The availability of positive or negative photomasks.
- The available exposure wavelengths (g-, h-, i-line in UV range).

After these questions have been answered, it is time to look for a resist meeting the requirements for lift-off process. Positive and negative photoresist are mainly used during the work of this thesis.

- Positive photoresist is suitable for lift-off process to only a limited extent for two main reasons: positive resists do not cross-link which keeps the softening point to values at 110-130^{0}C. Since these temperatures often occur during typical coating processes, the resist features will be rounded and become coated overall making lift-off hard or impossible. Even if the resist features do not soften, positive resists allow only positive or in the best case, 900 sidewalls which also promotes the coverage of the sidewalls during coating.
- Negative photoresist is generally the best choice for lift-off processes: on the one hand, negative resists designed for lift-off attain a reproducible undercut. Such an undercut help to prevent the resist sidewalls from being coated, which makes the subsequent lift-off easier. On the other hand, the crosslinking of the resin of common negative resists maintains the undercut even at very high coating temperatures, which helps to maintain the undercut during coating.

3.1.6 Basics of spin coating process

Spin coating has been used for several decades for the application of thin films [81]–[87]. A typical process involves depositing a small puddle of a fluid resin onto the center of a substrate and then spinning the substrate at high speed (typically around 3000 rpm) [88]. Centripetal acceleration will cause the resin to spread to, and eventually off, the edge of the substrate leaving a thin film of resin on the surface. Those parameters of the resin such as the viscosity, the drying rate, percent solids, etc. will effect to the quality of final film thickness. Factor such as final rotational speed, acceleration, and fume exhaust contribute to how the properties of coated films are defined [89].

One of the most important factors in spin coating is repeatability. Subtle variations in the parameters that define the spin process can result in drastic variations in the coated film. Fig. 3.5 describes the simple spin coating process:

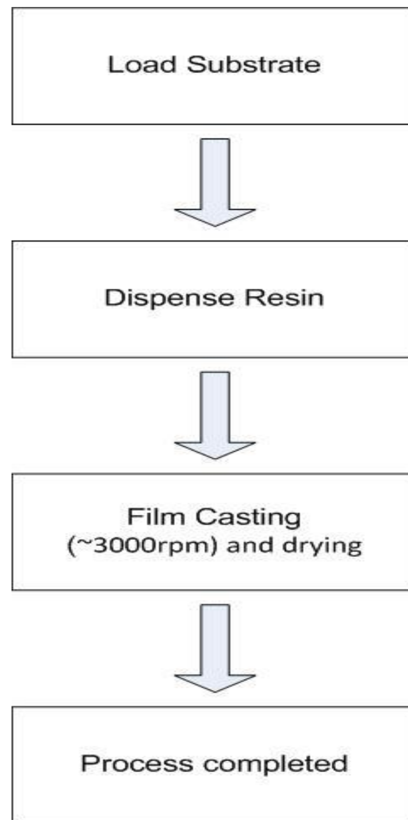

Fig. 3.5 Schematic of simple spin coating process [89]

In this process, the dispense step in which the resin fluid is deposited onto the substrate surface is carried out, a high speed spin step to thin the fluid, and a drying step to eliminate excess solvents from the resulting film. Two common methods of dispense are static dispense, and dynamic dispense.

Static dispense is simply depositing a small puddle of fluid on or near the center of the substrate. The volume of this fluid can range from 1 to 10 cubic centimetre (cc) depending on the viscosity of the fluid and the size of the substrate to be coated [90]. Higher viscosity and or larger substrates typically require a larger puddle to ensure full coverage of the substrate during the high speed spin step.

Dynamic dispense is the process of dispensing while the substrate is turning at low speed. A speed of about 500 rpm is commonly used during this step of the process [90]. This serves to spread the fluid over the substrate and can result in less waste of resin material since it is usually not necessary to deposit as much to wet the entire surface of the substrate. This is a particularly advantageous method when the fluid or substrate itself has poor wetting abilities and can eliminate voids that may otherwise form.

After the dispense step, it is common to accelerate to relatively high speed to thin the fluid to near its final desired thickness. Typical spin speeds for this step range from 1500-6000 rpm, again depending on the properties of the fluid as well as the substrate. This step can take from 10 seconds to several minutes. The combination of spin speed and time selected for this step will generally defined the final film thickness [91]. The final film thickness will be inversely proportional to the spin speed as shown in Fig. 3.6 and spin time [92], [93].

A separate drying step is sometimes added after the high speed spin step to further dry the film without substantially thinning it. This can be advantageous for thick films since long drying times may be necessary to increase the physical stability of the film before handling. Without the drying step problems can occur during handling, such as pouring off the side of the substrate when removing it from the spin bowl.

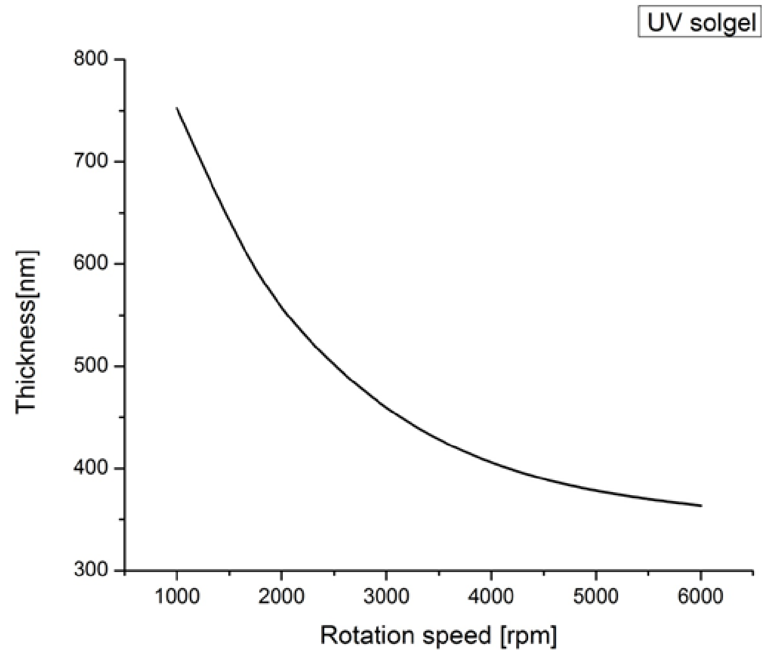

Fig. 3.6 Schematic of the spin curve of resist UV-Solgel. The thickness of the resist layer depends on the spin speed; higher thickness requires lower spin frequency.

3.2. Foundation of the applied characterization methods.

3.2.1. Basics of spectroscopic ellipsometry

Ellipsometry is an optical measurement technique which is used to determine the dielectric properties (complex index of reflection) and thickness of thin (a few Å – a few μm) transparent film [94]. It utilizes polarized light and its changing properties upon reflection and transmission at or through dielectric media.

Quickness, precision, and the non-destructive nature are strengths of the method. Therefore, ellipsometry is a standard measurement technique used in the industry (e.g. microelectronics, solar cells), as well as in basic research throughout natural and engineering sciences.

An ellipsometer comprises a light source, a polarizer and an analyzer. The principle of ellipsometry is based on the analysis of the change of light

polarization upon reflection from (or transmission through) a sample. A light beam with a known polarization is projected with a certain angle on the sample under test and the polarization of the reflected light is recorded as shown in Fig. 3.7 below:

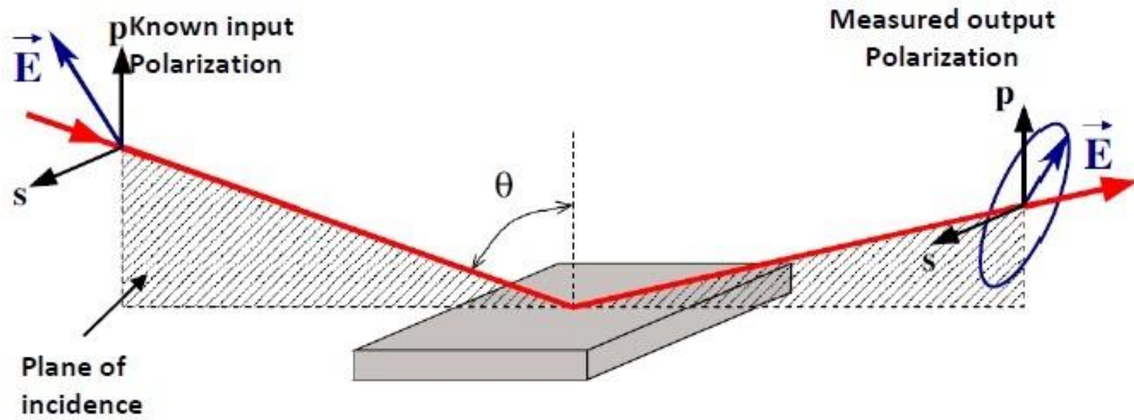

Fig. 3.7 Schematic of a typical ellipsometry configuration. Linearly polarized light is projected on a sample with incident angle (θ). The polarization of the light is changed upon reflected depending on the sample properties. The measured light is compared with the input light to extract important information about the unknown properties of the sample [95].

The incident polarized light can be resolved into two components p (parallel to the plane of incidence) and s (perpendicular to the plane of incidence) as illustrated in the Fig. 3.7. The p-polarized and the s-polarized lights reflect differently off the sample and have different reflection coefficient R_p and R_s. However, they are not separately measureable and instead the complex reflection coefficient ratio (ρ) defined in term of R_s and R_p as shown in equation 3.3 is measureable.

$$\rho = \frac{R_p}{R_s} \tag{3.3}$$

This complex reflection coefficients ratio is related to the structural and optical properties of the sample and it is determined by pure polarization measurements with ellipsometry. Commonly, the ratio is represented in polar form in terms of two ellipsometric angles ψ ($0 \le \psi \le 90^0$) and Δ ($0 \le \Delta \le 360^0$) as shown in equation below [96].

$$\rho = \tan(\psi) e^{j\Delta} \qquad (3.4)$$

Where ψ is the amplitude ratio ($|R_p|/|R_s|$) and Δ is the differential phase shift ($\Delta_p - \Delta_s$).

Spectroscopic ellipsometry (SE) measures the two values (ψ, Δ) as a function of the wavelength of incident light [94], we can extract both the thickness and also the dependence of the optical properties on wavelength with SE. Variable Ellipsometry (VASE) work as a function of both the wavelength and the angle of the incidence. The different angles provide new information and therefore enhance the sensitivity to the unknown parameters [95].

To extract the optical parameters of the sample to be measured requires a complex data analysis of the measurement data by means of software (e.g, WVASE32) numerically a model function adjusts. In this case, a fit model only with the help of already known material parameters such as refractive indices $n_i(\lambda)$, extinction coefficient $k_i(\lambda)$ and the individual layer thickness d_i are created. Then with this model the theoretical ψ_{theory} and Δ_{theory} will be calculated. Through an interactive variation of material parameter is the theoretical model function extent modified to an optimum agreement of the experimental $\psi_{exp}(\lambda)$, $\Delta_{exp}(\lambda)$ and the theoretical $\psi_{theory}(\lambda)$, $\Delta_{theory}(\lambda)$ is achieved values. The calculated and experimental data are compared and an estimator like the Mean Squared Error (MSE) can be used to indicate how well the calculated data fits the measured

data. The unknown model parameters are varied to get the best fit between the generated and measured data. A model that is reasonably close to the measured data has an MSE < 10.

3.2.2 Basics of white light interferometer (WLI)

White light interferometer is a fast, non-contact measurement technique with high accuracy and long measurement range, it offers high quality 3D image with high vertical precision for optical MEMS as well as microstructures [97], [98].

A WLI system employs a broadband light source, an interferometer objective (Mirau/Michelson), a PZT translator for moving the objective in nanometer scale, and a camera for capturing the interferogram. The system setup is shown in Fig. 3.8.

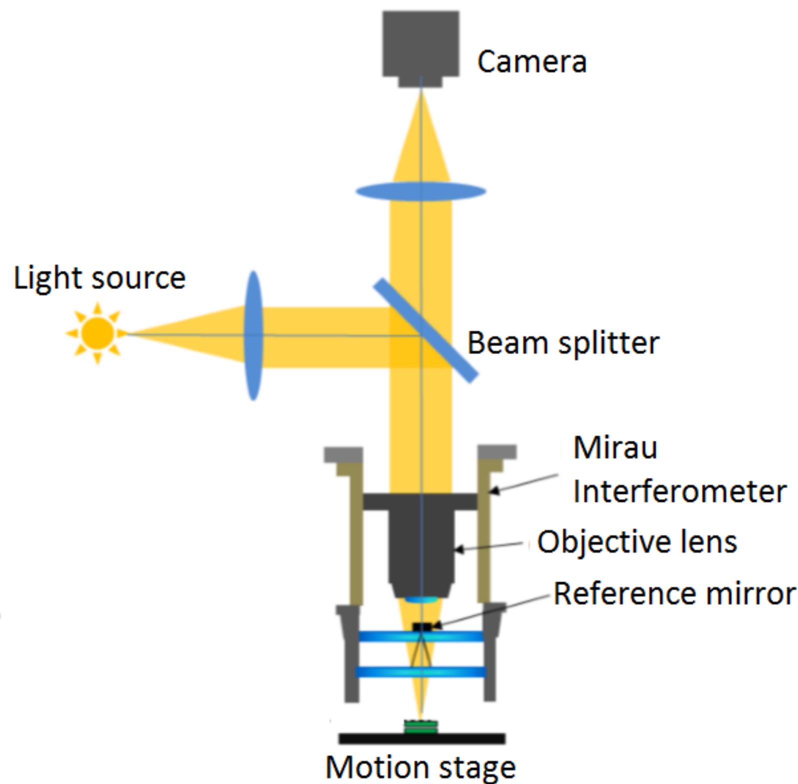

Fig.3.8 Schematic illustration of the main components of the white light interferometry, original figure from [99]

The light from the white light source is divided in two beams by a beam splitter: one beam goes to an internal reference mirror and the other one goes to the sample under test. The reflected beams from reference mirror and the sample interfere constructively and destructively and produce bright and dark fringe pattern which is captured by the camera. The objective is moved vertically in small steps with the help of the translation system. The intensity data is recorded by camera as a function of the vertical position for each pixel. The data is then processed to create a complete 3D image of the sample surface. The lateral measurement are performed by calculating the pixel size from the field of view of the objective in use while the vertical measurement is created interferometrically [97].

The WLI used at INA is Zygo NewView 5000 system from Zygo Corporation with maximum vertical step height of 100 µm and vertical resolution of 0.1 nm. The lateral field of view and the lateral resolution depend on the objectives as well as the image zoom setting. With 5x objective, the field of view is up to 3.525 mm x 2.65 mm. Lateral resolution down to 0.32 µm can be obtained when use 50x objective.

3.2.3 Introduction of the measurement setup for spectral characterization

3.2.3.1 Compact microscope spectrometer setup

This microscope spectrometer setup was installed and reported earlier in the work of H. H. Mai [50] in order to characterize the optical properties of FP filter arrays in visible range.

Construction of the microscope spectrometer setup

The microscope spectrometer setup includes four main parts: (i) an illumination system, (ii) a collimation and magnification system, (iii) a sample stage and

finally (iv) a data recording and analysis system. The construction detail of the setup is shown in the Fig. 3.9 below:

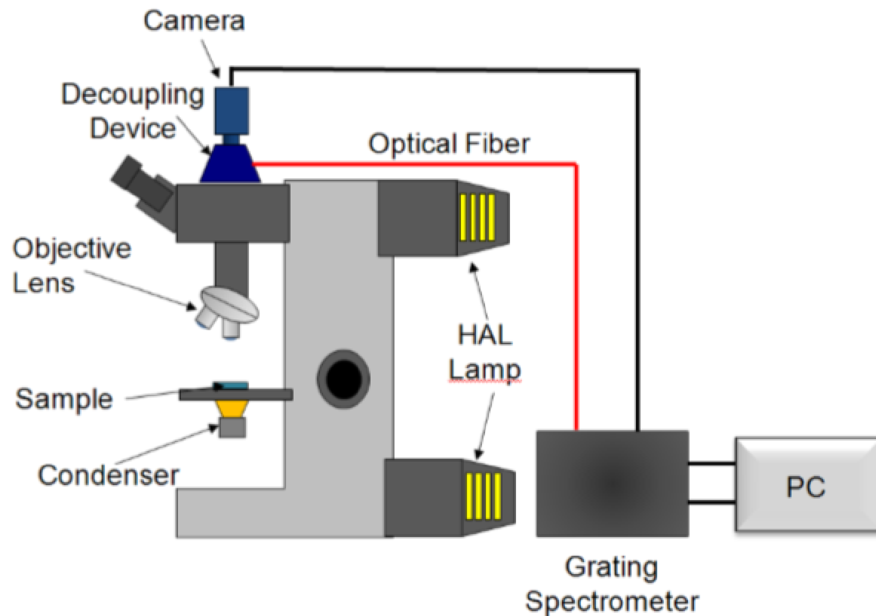

Fig. 3.9 Scheme of the experimental setup of the compact microscope spectrometer

(i) The illumination system of the setup: Two halogen lamps [100], [101] HALs 100 are used as broad band light sources; one lamp is used for reflection measurement and other for transmission measurement.

(ii) The collimation and magnification system: the optical microscope *Axio Image D 1m* from *Carl Zeiss* is used for collimation and magnification. This optical microscope includes a series of elements such as objective lenses, a translation stage, a condenser, a CCD and a decoupling device with an adjustable diaphragm. Three kinds of objective lenses 2.5x, 10x and 50x are used with high numerical aperture (NAs) which results in high resolution and bright image with rich contrast of the sample.

(iii) The sample stage: is an important part in any measurement setup used for carrying the samples and scanning the whole of the samples. In this setup the translation stage *Scan 100 x 80-1 mm Maerzhaeuser Wetzlar* is used.

This translation stage can be displaced in x-, y- and z- directions, whereas the inspected sample is placed on the microscope translation stage. A CCD camera is used to capture the real image of the structure and to define the exact position of the filter. By adjusting the diaphragm aperture to fit the different image sizes, different filter dimension can be measured.

(iv) The data recording and the analysis system of the setup: in this work, the data recording system consist of a coupling device used to select and couple the transmitted or reflected light from FP filter into an optical fiber, together with an OSA for recording and analyzing the data. The *OSA AQ6375* from *YOKOGAWA* is used for NIR measurements, this OSA can be calibrated for the measurement of wide spectral ranges from 350 nm to 1200 nm. The OSA works as a spectrometer and a detector and can measure transmission and reflection spectrum in combination of a microscope. The spectrum is directly shown on the screen of the analyzer using the software *AQ6370 Viewer* with variable wavelength resolutions from 0.02 nm to 10 nm.

Working principle of the setup in transmission measurement

The transmission measurement is shown in Fig. 3.10 below:

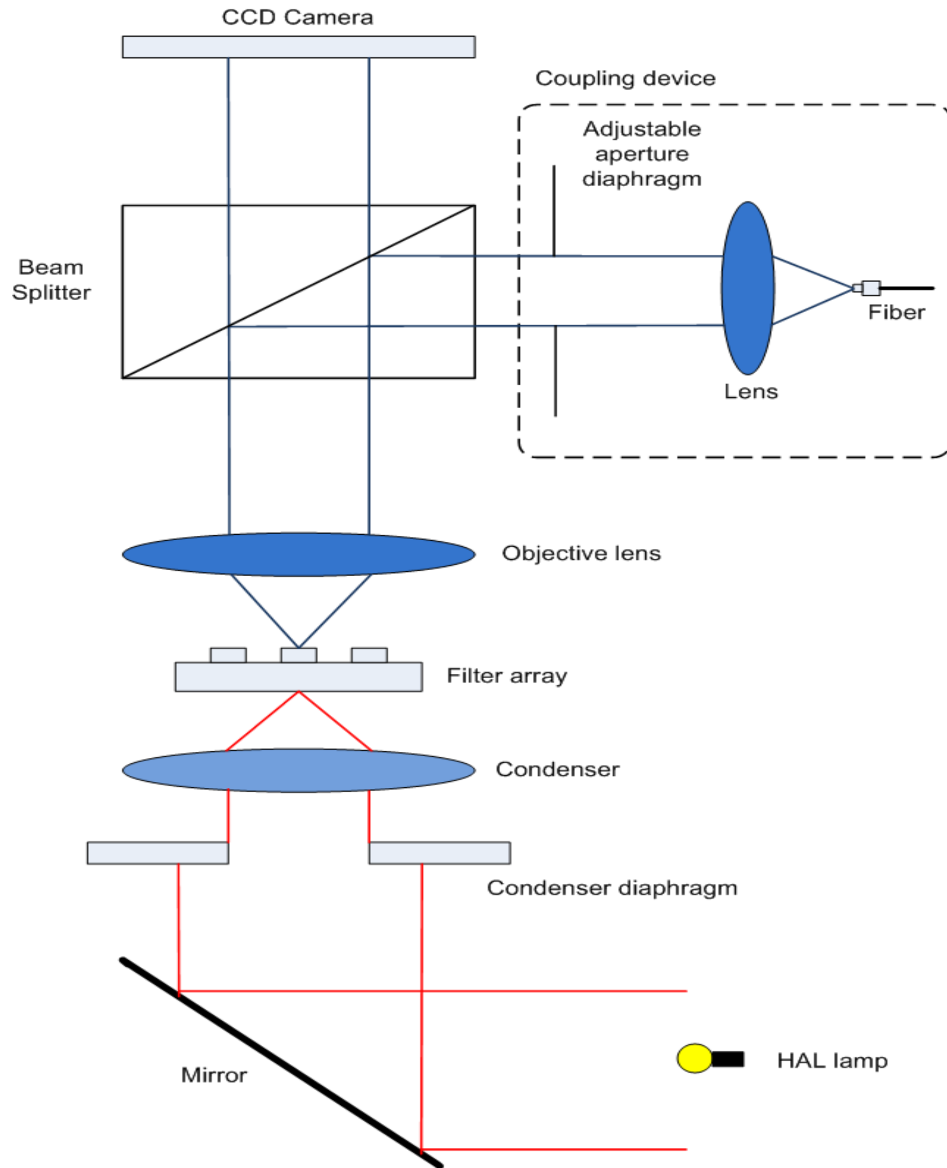

Fig. 3.10 Scheme of the system for transmission measurement, redraw from [99]

The filter is first placed on the translation stage and illuminated by light coming from the underneath sample using the lower halogen lamp. This light is reflected by the mirror upward to the condenser diaphragm placed underneath the translation stage, the light is concentrated to the sample surface as a circle of few millimeters diameter, and here the interaction between light and the filter takes place. The transmitted or diffracted light through the sample is gathered by the objective lens and guided to beam splitter which splits the beam in two parts: one

part strikes to the CCD camera to display the top view image of the filter structure, the other part is reflected to the adjustable aperture diaphragm and then focused by a single lens and couple into the optical fiber.

3.2.3.2 Free beam broad band confocal setup

With this setup, we can measure in not only visible range but also in NIR range. In this part we will discuss about the construction details and the working principle of the setup.

Construction of the free beam broad band confocal setup

This setup has the same construction like the compact microscope spectrometer setup; it consists of four main parts: (i) an illumination system, (ii) a collimation and magnification system, (iii) a sample stage and (iv) a data recording and analysis system. On the other hand, an imaging system is equipped with the setup for capturing the top view image of the sample. The construction of the setup is shown in Fig. 3.11 below:

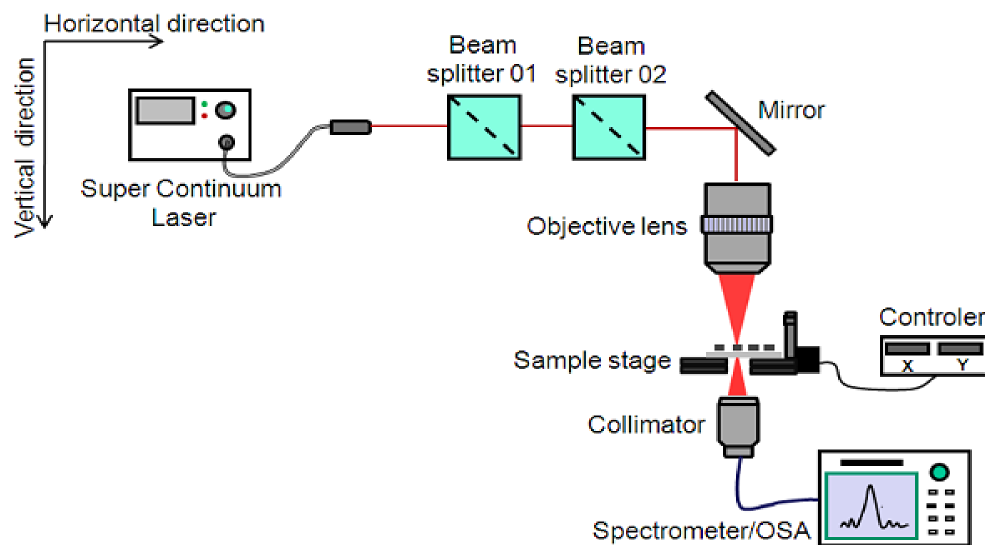

Fig. 3.11 Schematic diagram of the free beam broad band confocal setup for transmission and reflection measurements, original figure from [99].

(i) The illumination system of the setup: a SuperK Extreme Super-continuum white light laser (SCWLL) [102], [103] is used as the illumination system. Compare with HAL lamps used in compact microscope, this laser can support a very wide spectral output covering from 460 to 2400 nm with high average power of about 4.3 W. The laser output is a single mode Gaussian beam with the beam quality M^2 less than 1.1, and the beam divergence is less than 5 mrad.

(ii) The collimation and magnification system of the setup: in this work, the collimation and magnification consists of a mirror coated with Aluminum which allows a good agreement in reflecting all the wavelengths of the SCWLL and an objective lens which is assigned to project a focused beam on the filter membrane. In this setup, we use the 10x objective lens from Mitutoyo *NT46-403 Mitutoyo Objective lens, Edmund Optics*, it can work in the visible range as well as in the NIR range, specifically from 480 to 1800 nm, with high transmission efficiency of 80% in the visible range and 60 % in the NIR range [99].

(iii) The sample stage: is used for carrying the sample and can move in x, y, z direction and help to scan and focus thoroughly the whole of filter arrays. The scheme of the sample stage is shown in Fig. 3.12 below:

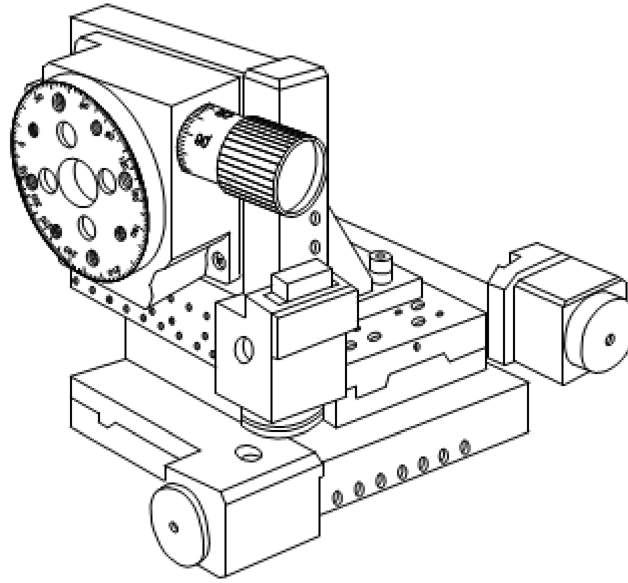

Fig. 3.12 Scheme of the sample stage consisting of a xyz translation with sub-micron resolution and a rotation stage, original figure from [99].

(iv) The data recording and analysis system of the setup: as shown in Fig. 3.11 above, this part consists of a collimator, a grating spectrometer or an OSA (in this work we use the OSA). The collimator *IR CFC 11X-C 1050-1620 nm* from Thorlabs is used for the measurement in NIR range. The central lenses can be moved along the optical axis with the maximum translation 1.5 mm and be adjusted in vertical and horizontal direction to find the most appropriate position of the lenses for achieving the best coupling efficiency. Two OSAs, *AQ 6373 350-1200 nm and AQ 637 1200-2400 nm*, are used for measurement in the range from 350 nm to 2400 nm. The fiber connected from collimator to OSA is single mode fiber to avoid the losses of the power during propagation.

(v) The imaging system of the setup is installed in order to observe the top view image of the filter arrays on the sample during measurement. The schematic diagram of the imaging system is shown in Fig. 3.13. It

consists of an LED, beam splitters, a tube lens, and a camera. The LED is used to illuminate the sample during measurement, the beam splitter 3 (BS 03) together with the beam splitter 1/cold light mirror are arranged to guide the LED light beam to the collimation and magnification systems, then finally project on the sample, the tube lens is used to create and project an intermediate image of the filters on a CCD camera.

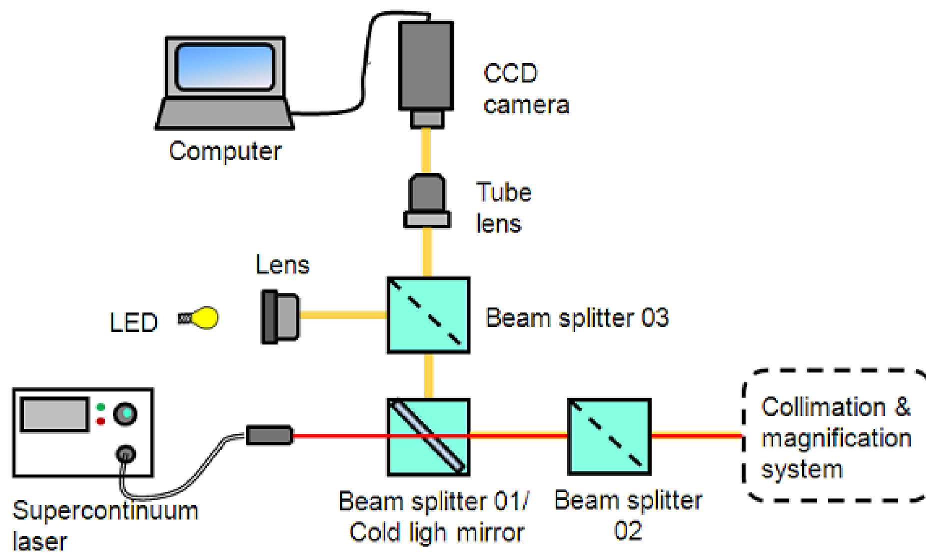

Fig. 3.13 Schematic diagram of the imaging system for visualizing the filter structure being measured, original figure from [99].

Working principle of the free beam broad band confocal setup

Fig. 3.14 shows the schematic diagram of the free beam broad band confocal setup, this setup can measure both transmission and reflection. The laser beam form SCWLL is projected firstly to beam splitter 01 (BS 01) in case of measurement in visible range or cold light mirror in case of measurement in NIR range, then strikes the mirror of the collimation and magnification system. Here,

the laser is reflected downward to the objective lens. Afterward the laser beam is focused on the filter. The light then guided to the condenser and coupled into a single mode optical fiber. The transmission spectrum is analyzed by an OSA. In case of measuring reflection, the reflected light travels backward to objective lens, the mirror, the beam splitter 02 (BS 02), and finally is coupled into a single mode fiber.

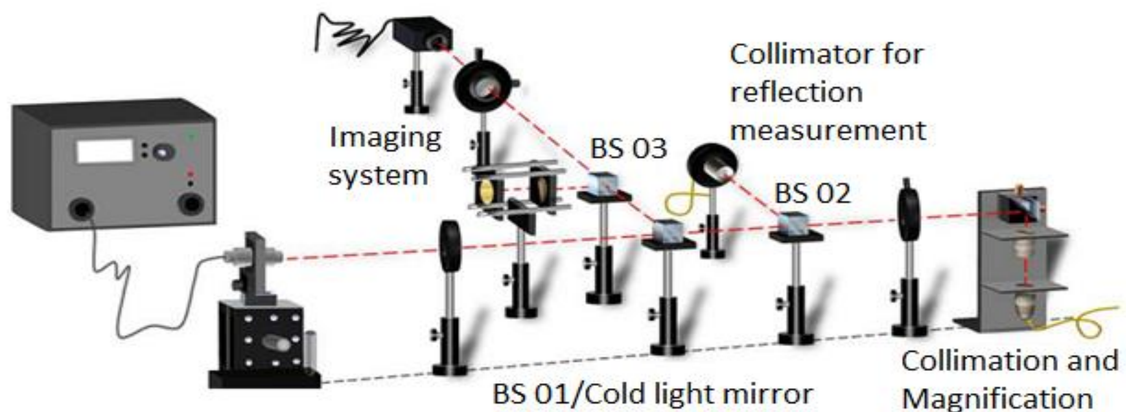

Fig. 3.14 The final assembly of the free beam broad band confocal setup. The setup includes four main parts: the SCWLL as an illumination system, the collimation and magnification system, the imaging system and the sample stage.

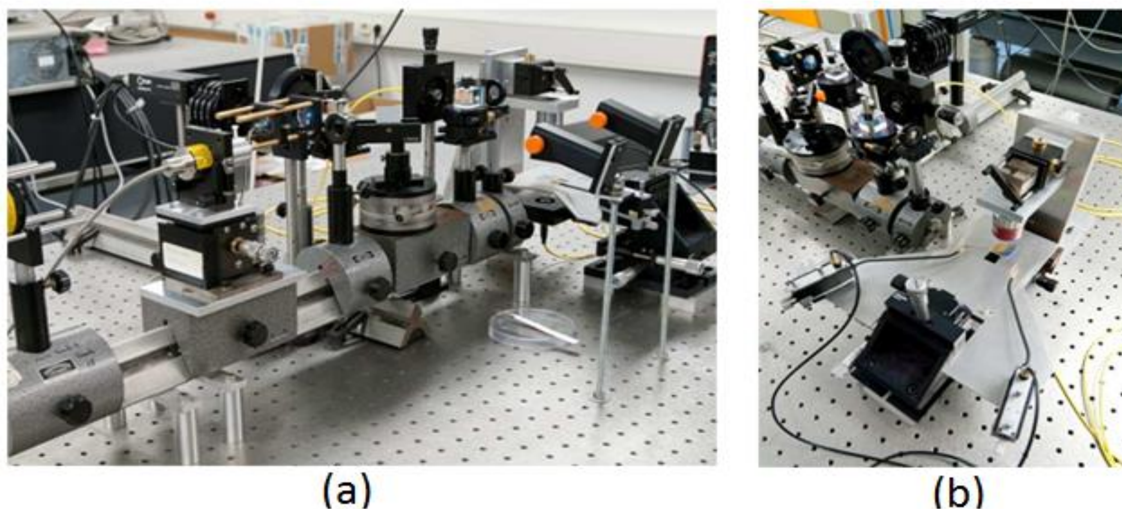

Fig. 3.15 Side view (a) and top view (b) of the free beam broad band confocal setup

4. Design, simulation and fabrication of NIR FP filters

This chapter will present the design and simulation for static NIR FP filters with different cavity structure designs. The simulated results of optical properties of different methods will also be compared and discussed.

4.1 Design of NIR static FP filters

The NIR static FP filters comprise of two identical dielectric Distributed Bragg Reflectors (DBRs) designed for a specific wavelength range. Each DBR consists of a periodic sequence of thin dielectric films with alternating high and low refractive indices. The optical thickness of each thin film in the DBR is a quarter of the design wavelength range in the respective material. The DBR reveals a spectral range of high reflectivity (the so-called stop-band) and these two DBRs form a resonator and the space in between is called FP cavity. The thickness of each cavity is directly proportional to the corresponding spectral filter line for a considered cavity material for each individual filter.

In this work, the NIR static FP filters are designed in three methods, namely (i) multiple spin coating, (ii) hybrid cavity and (iii) the novel resist corresponding with three structuring cavity designs. Fig. 4.1 shows the structuring of FP filter cavities using three different designs.

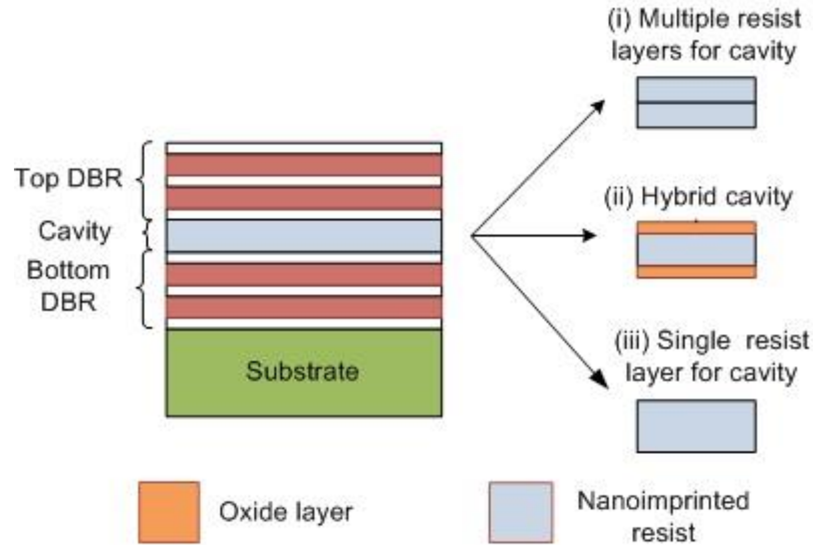

Fig. 4.1 Schematic of structuring FP filter cavities using three different methods.

In the method using multi spin coating, the multiple layer cavities are structured using subsequently several spin coating steps. The thickness of each resist layer in each individual spin coating process is d_1 (nm), d_2 (nm)… d_n (nm). Thus, the total cavity thickness is described $d = d_1 + d_2 + \ldots + d_n$ ideally. Each layer is cured by UV light for few minutes except the last layer. The spin coating time depends on the desired individual thickness. The last resist layer has to meet the required thickness for the SCIL process to receive the desired cavity structure.

In the method using hybrid cavity, thin oxide layers having a similar refractive index as the UV-curable resist are used to enlarge the total cavity height. Two thin oxide layers are embedding the resist layer which is imprinted. In this case, three layers comprise the cavity.

In the method using novel resist material, the imprint process is modified and improved by applying a novel resist material (mr-NIL210) with freely adjustable film thickness, the full desired thickness of the initial resist layer can be achieved

in a single spin coating step at high spin frequencies guaranteeing a smooth and homogeneous surface layer.

4.2 Simulation of NIR static FP filters

4.2.1 Simulation of DBRs for FP filters

The bottom and top DBR are simulated by OpenFilters software with 9.5 periods Si_3N_4/SiO_2 using PECVD deposition technology. Fig. 4.2 depicts the optical property of bottom DBR designed for the center wavelength at 1450 nm. The refractive index of Si_3N_4 is about 1.78 and for SiO2 is 1.42, thus, the difference of high refractive index and low refractive index is 0.36. A large stop-band of approx. 170 nm can be achieved.

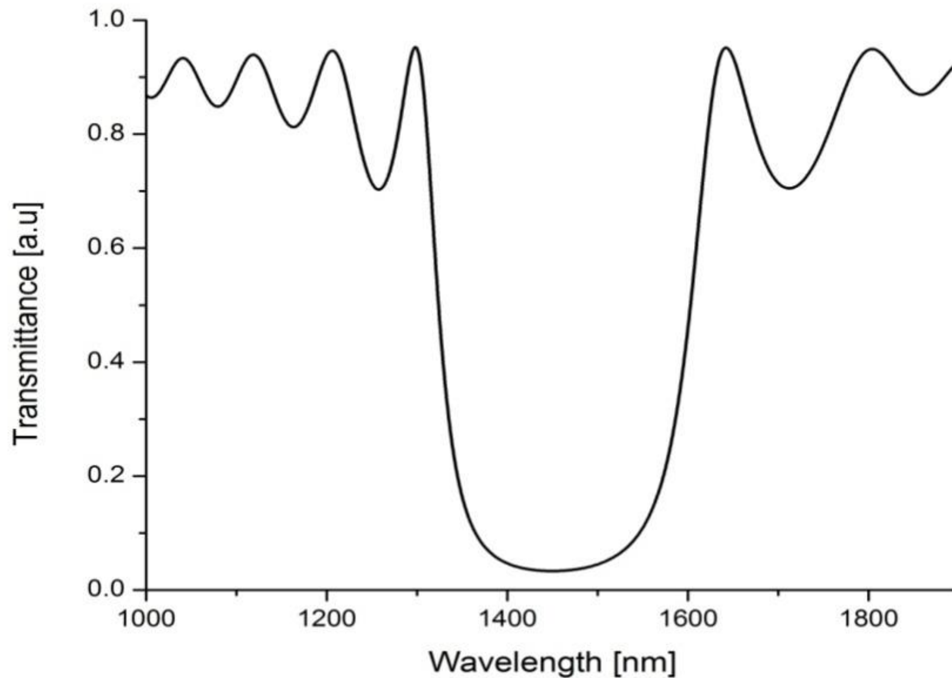

Fig. 4.2 Transmittance property of bottom DBR at designed wavelength 1450 nm

4.2.2 Simulation of NIR static FP filter arrays

The NIR static FP filter arrays are simulated following three designed methods. Two kinds of resist from Micro resist technology GmbH are used for the cavity layer: conventional resist mr-UVCur06 and novel resist mr-NIL210.

In this work, two times spin coating were applied to enlarge the initial resist thickness in the method using multiple spin coating. For the method using hybrid cavity, SiO_2 layers were used to combine with resist since it has comparable refractive index to the resist mr-UVCur06. The resist mr-NIL210 is applied for the novel resist method. Fig. 4.3 depicts the spectral variation of the refractive index for Si_3N_4, SiO_2, mr-NIL210 and mr-UVCur06 measured by ellipsometer. In the spectral range of interest, the difference in refractive index between SiO_2 and-UVCur06 is smaller than 0.1.

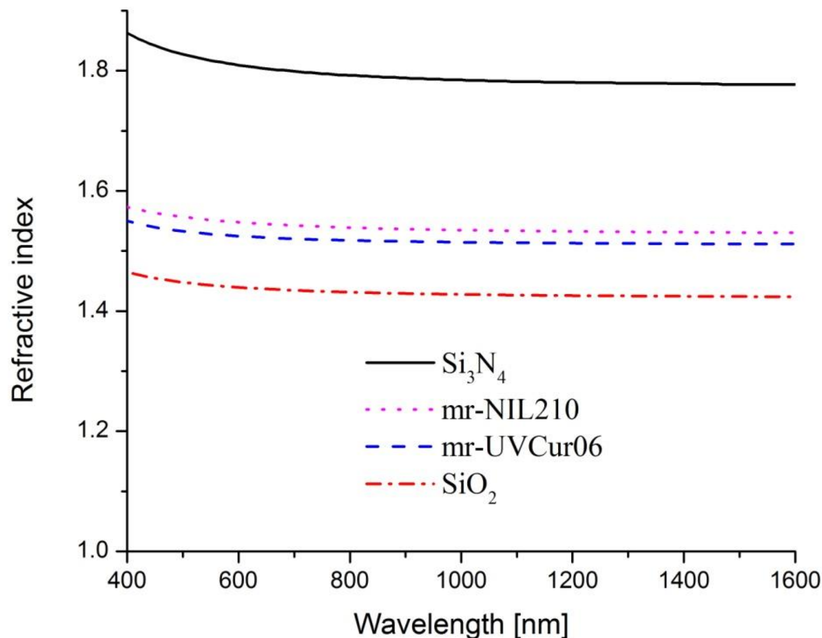

Fig. 4.3 Schematic of the refractive indices of SiO_2, Si_3N_4, mr-UVCur06 and mr-NIL210

Figs. 4.4 – 4.6 show the transmission properties of FP filter arrays simulated in the spectral range 1.4 – 1.5 µm.

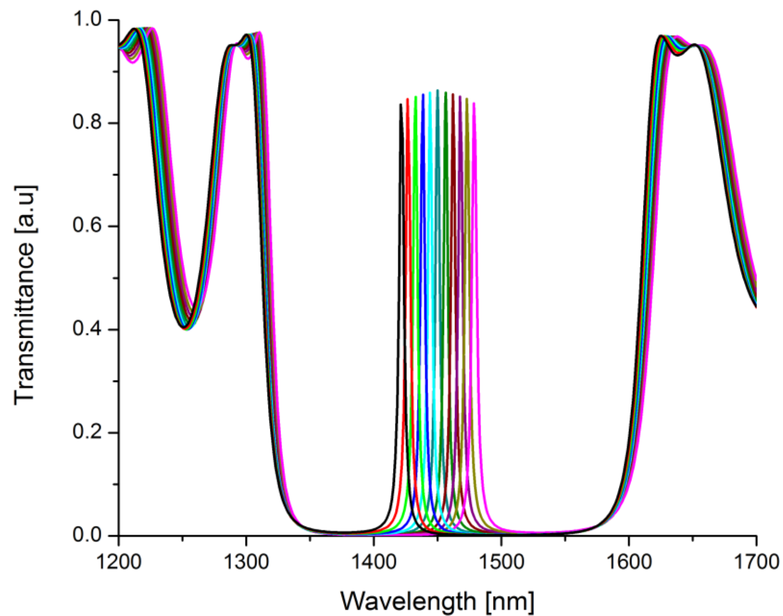

Fig. 4.4 Optical transmission spectra of filter arrays using spin coating twice for the cavity layer.

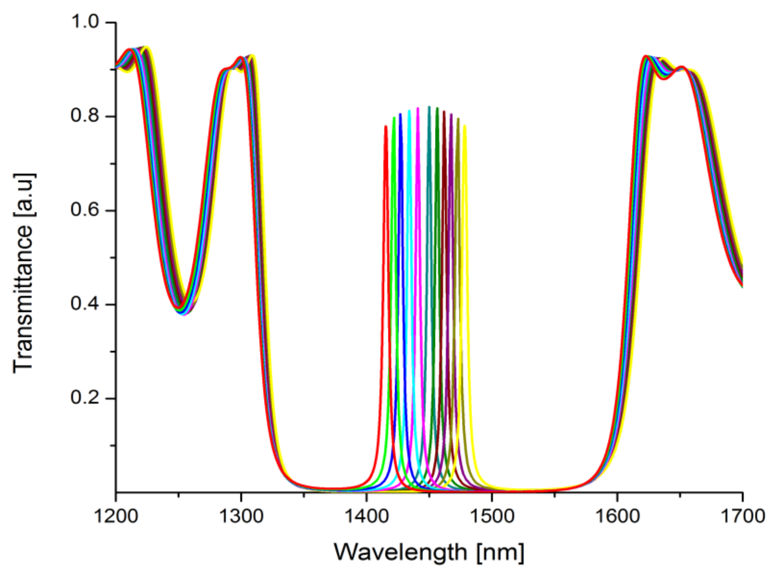

Fig. 4.5 Optical transmission spectra of filter arrays including the hybrid cavities

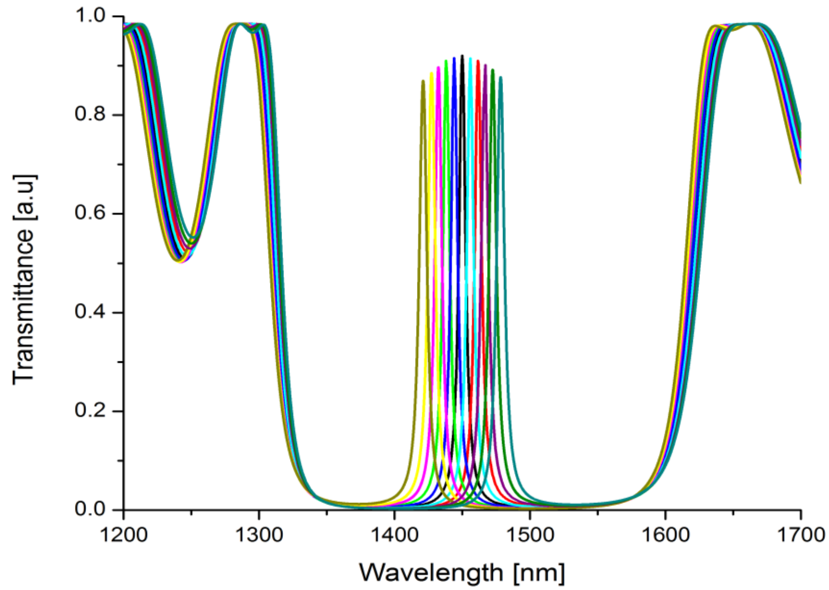

Fig. 4.6 Optical transmission spectra of filter arrays using the novel resist mr-NIL210 for the cavity layer

4.3 Discussion of the simulation results

4.3.1 Deposition rate of PECVD and deformation of stop-band of FP filters

As mentioned above, the bottom and top DBR are deposited by PECVD, these two DBR deposition process is separated by the process of cavity fabrication, and thus, the final stop-band of FP filters will strongly depend on the deposition rate of PECVD.

PECVD is a low cost and fast deposition technology, but it has also lower accuracy due to the multiple function of the machine and regular cleaning process of the chamber. Therefore, the mismatch in deposition rate between bottom DBR and top DBR might happen and leads to the deformation of the stop-band of FP filter. Fig. 4.7 shows the optical transmission spectra of FP filter at 1450 nm, the blue one is the transmission spectra of FP filter which has the same deposition rate for bottom and top DBRs and the other one is transmission

spectra of FP filter with mismatch of deposition rate between bottom and top DBR. This deposition rate mismatch leads to the shift of the transmission spectra line and the deformation of stop-band.

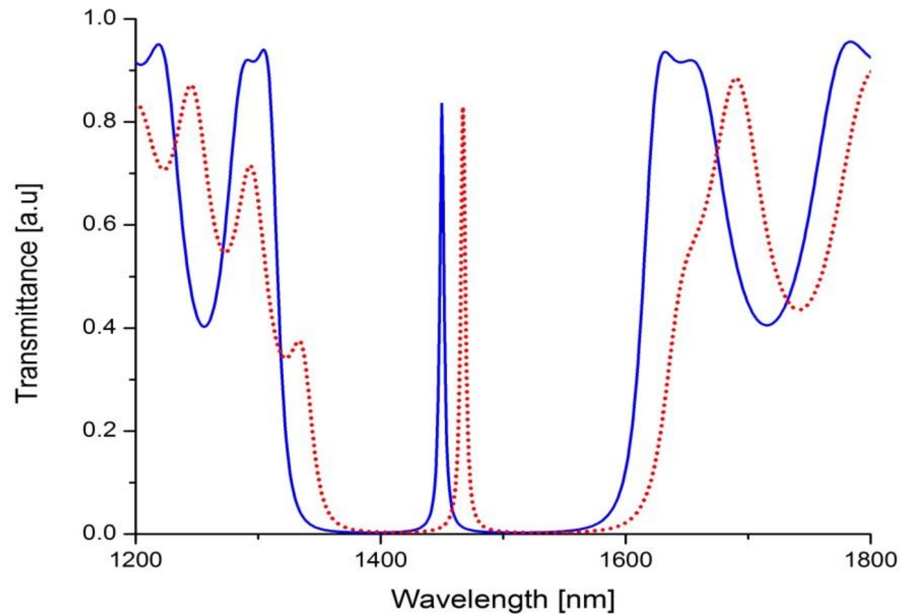

Fig. 4.7: Optical transmission spectra of FP filter with different deposition rate between bottom and top DBR: blue one has identical deposition rate and the red one has the mismatch deposition rate.

4.3.2 Simulated optical properties of FP filter arrays in three different methods

Figs. 4.4 – 4.6 reveals the optical transmission spectra of FP filter arrays simulated by OpenFilters for three methods. The simulated transmission of three methods is between 79 to 91%, the lowest transmitted intensity is obtained for the method using hybrid cavity. Fig. 4.8 depicts the comparison of simulated transmission for three methods in the spectral range 1.4 – 1.5 μm.

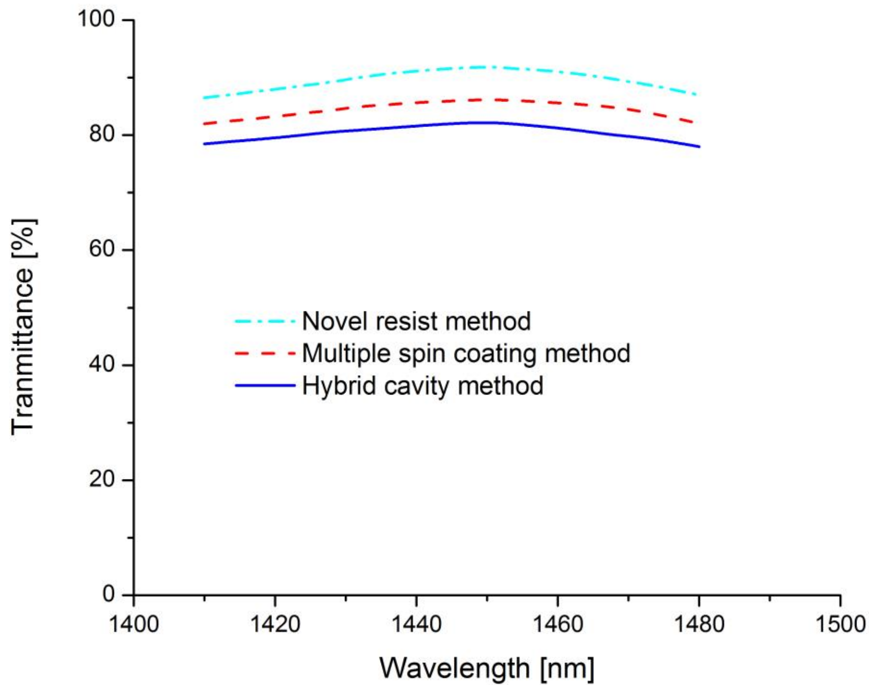

Fig. 4.8 Comparison of simulated transmittance properties of FP filter arrays using three different fabrication methods

Fig. 4.8 reveals that the transmission of FP filter arrays is highest in the method using novel resist and lowest in the method using hybrid cavity. The reason behind this phenomenon is: (i) the presence of SiO_2 layers in cavity in the method using hybrid cavity, which has a mismatch refractive index with resist mr-UVCur06 (0.1 in refractive index difference, as mentioned above), and therefore affects to the interference of light inside cavity and (ii) absorption of SiO_2 layers inside cavity. On the other hand, the heterostructure of cavity also affects to the optical properties of the FP filter arrays, as shown in Table 4.1, the transmission of FP filter arrays is reverse proportional with the number of interfaces in cavity structure, e.g. the transmitted intensity in the method using multiple spin coating is higher than that in the method using hybrid cavity and smaller compared to method using novel resist.

Table 4.1: Average transmission obtained for each FP filter fabrication method

Technological method	Simulated transmission of FP filter arrays (%)	Number of interfaces involved in the cavity
Hybrid cavity	80	4
Multiple spin coating	84	3
Novel resist	87	2

Fig. 4.9 shows the comparison of FWHM for three FP filter fabrication methods in the spectral range 1.4 – 1.5 µm. The simulated FWHM of three FP filter fabrication is between 4 to 4.58 nm, the largest value is achieved in the method using hybrid cavity.

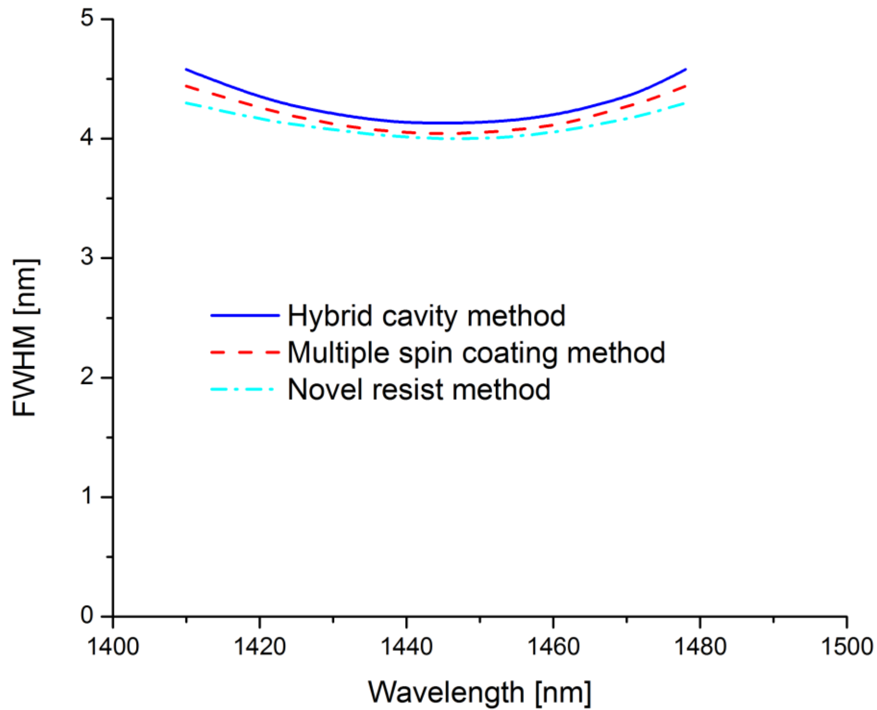

Fig. 4.9: Comparison of simulated FWHM of FP filter arrays using three different fabrication methods

From the Fig. 4.9 it can be seen that the FWHM is smallest in the center of stop-band and larger values are obtained for the filter transmission lines located at the borders of the stop-band. This is due to the fact that the reflectivity of the DBR mirrors is largest in the center of the stop-band. The more the filter transmission lines are shifted towards the borders of the stop-band the lower the reflectivity and, thus, the larger the FWHM of the lines. This result is in agreement with previous works of [104], [105].

Fig. 4.9 also reveals that the largest simulated FWHM is achieved for the method using hybrid cavities and smallest for the method using novel resist. As discussed above, the presence of SiO_2 in cavity and the hetero structure of the cavity lead to the lower optical properties of the FP filter arrays. Table 4.2 shows the average value of FWHM for three fabrication methods corresponding with the number of interfaces. The more interfaces the lower optical properties are.

Table 4.2: Average FWHM obtained for each FP filter fabrication

Technological method	Simulated FWHM (nm) of the filter transmission line	Number of interfaces involved in the cavity
Hybrid cavity	4.3	4
Multiple spin coating	4.2	3
Novel resist	4.1	2

4.4 Fabrication of NIR static FP filters

The fabrication of NIR static FP filters comprise the following steps: First, the bottom DBR is deposited on a detector array or on a transparent substrate which combined with a detector array afterwards. Next, the 3D nanoimprint process is performed using a 3D nanoimprint mold that contains negative cavity structures. Finally, the top DBR is deposited on the top of the nanoimprinted cavities. This

process is applied to fabricated FP filter arrays using a novel resist. In case of using multiple spin coating or hybrid cavity method, some additional steps to define the multiple layer cavity structure as well as the depositions of thin oxide layers, respectively.

Fig. 4.10 shows the fabrication process of NIR FP filter arrays.

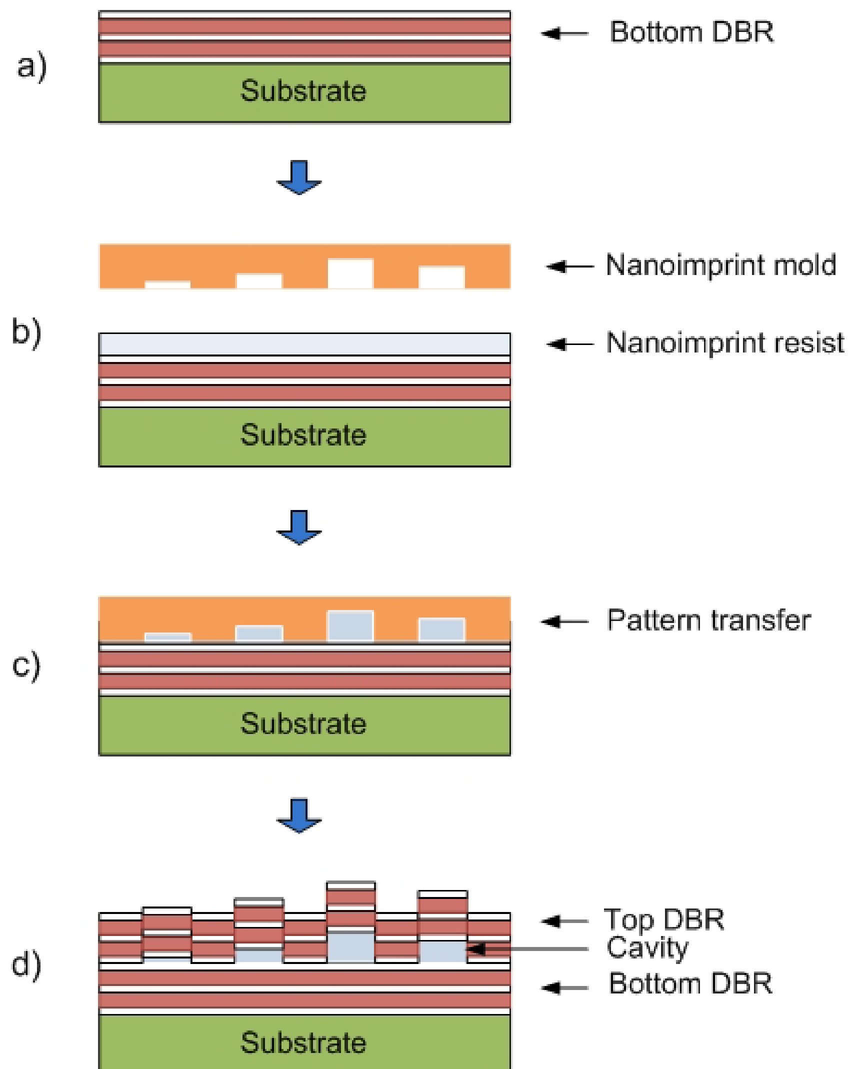

Fig. 4.10: Fabrication process of FP filter array: a) bottom DBR deposition, b and c) 3D nanoimprint to structure the filter cavities, d) top DBR deposition

5. Fabrication and characterization of master template for the near infrared range

In the process of FP filters fabrication, the 3D master template plays a very important role since its vertical height will be transferred to UV-Curable resin layers and defines the cavity thickness, which sets the spectral lines position at the end. In the previous work, we have successfully fabricated the master template for visible range having the height distributed from 30 nm to 180 nm [33]. However, these master templates are not suitable for the near infrared range since the working range of NIR range is from 800 nm to 2400 nm, which requires a master template having height up to 1 μm. Thus, new master templates are needed for the FP filters fabricated in the NIR range. This chapter will present the fabrication process, the result and discussion of the templates fabricated for NIR, and finally is the replication of soft stamp for SCIL process.

5.1 Fabrication of master templates for NIR range

The fabrication steps of 3D templates is introduced in detail in the work of [80]. It comprises of few steps:

(i) Cleaning GaAs wafer with isopropanol: this step is done to guaranty that the wafer is totally clean before going to lithography step. This cleaning will remove all the contaminants, particles which might affect to the precision of lithography step.

(ii) Baking the wafer for minimum 10 minutes at 120°C: after cleaning wafer with isopropanol and dry it with Nitrogen gas, the wafer is placed on the hot plate at 120°C for at least 10 minutes to remove all the water molecular.

(iii) Applying Ti Prime on the wafer substrate: Ti Prime is applied to increase the adhesion of photoresist on the wafer substrate. This is

done by spin coater; the Ti Prime is first dropped on the substrate and then coated at 4000 rpm for 40 seconds.

(iv) Applying photoresist on the wafer: the negative AZ 1518 is dropped on the wafer and coated at 4000 rpm for 40 seconds; this high rotation spreads the resist evenly on the wafer and attains a layer thickness of approximately 1.8 μm.

(v) Prebaking for 5 minutes at 90°C: This process to make the photoresist solid and now it is ready for lithography step.

(vi) Alignment and exposure under UV light (lithography step): the wafer containing the positive photoresist AZ 1518 is first aligned with the photomask using the Mask Aligner MA4 and then exposure with the UV light for 6.6 seconds. This step will transfer the structures on the photomask to photoresist layer on the substrate.

(vii) Development in 0.8% KOH for about 30 seconds: the exposure photoresist areas on the wafer in step (vi) will be soluble in KOH and be removed from the wafer and the unexposed photoresist areas are kept after development process, therefore the patterns are built up on the wafer.

(viii) Post bake for 5 minutes at 120°C: this process is also known as "hard baking". The photoresist becomes acid resistance and is used as a mask layer during the chemical etching process.

(ix) Plasma Diener process: this step is used to remove the rest of the resist which might not be removed from the development step.

(x) RIE etching: in this thesis work, the "Oxford Plasma 80 Plus RIE" was used for the etching step. The standard recipe is (CH_4(6)/H_2(36) sccm, 150W, 0,008 Torr, 20^{0}C since this recipe provides moderate etching rate and smooth surface [80].

(xi) Remove photoresist: first, the wafer is put into the NMP at 80°C for at least 8 hours, then the container storing the sample and NMP is vibrated by applying ultrasonic cleaning with 80% ultrasound power (Elma, Transonic Digitals). The high solubility of NMP at 80°C and the ultrasonic vibration help to break and peel off the photoresist.

To produce 64 different cavity heights, different photomasks are used with a series of lithography and RIE processes. The Fig. 5.1 below shows the fabrication process of master template using positive photoresist AZ1518.

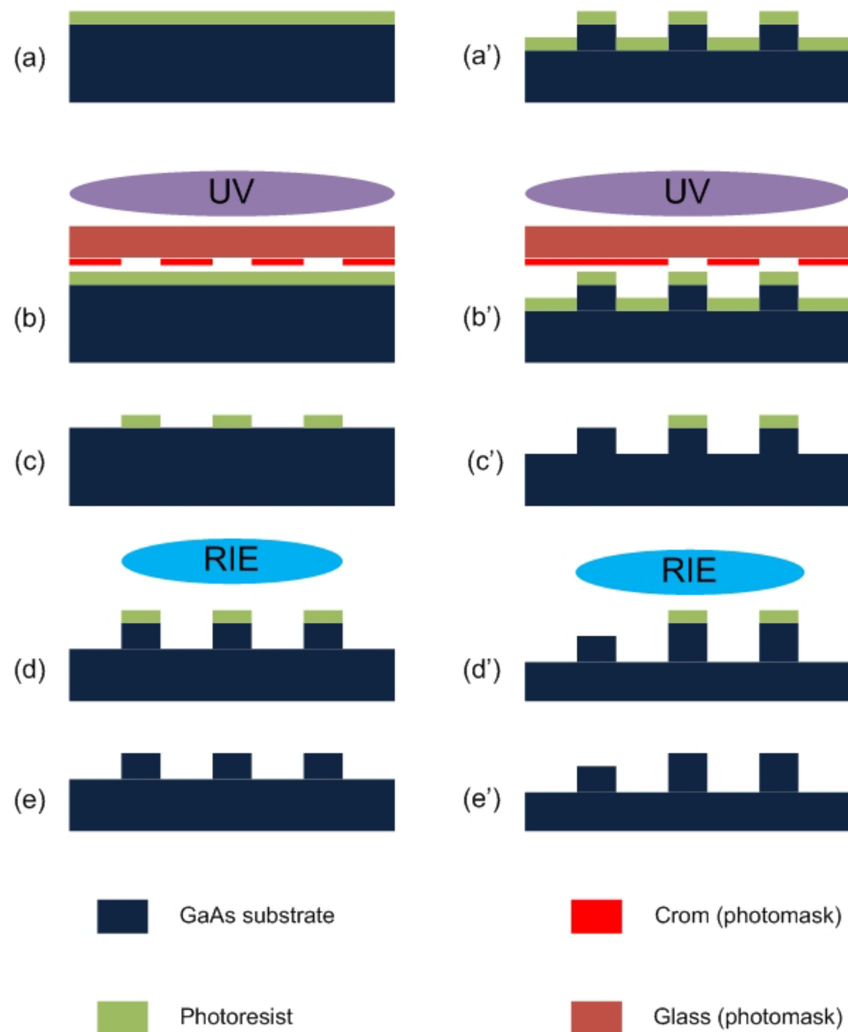

Fig. 5.1 Fabrication process of 3D master template: (a)-(e) is the first round, (a) spin-coating of positive photoresist AZ1518, (b) alignment, exposure, (c) development, (d) RIE and (e) remove photoresist; (a')-(e') is the next fabrication round.

5.2. Experimental results of NIR master template and discussion

5.2.1 Experimental results

Figure 5.2 shows the microscope image of mesa arrays of master template. The main structure is 8x8 inside the 12x12 arrays, e.g. covered by black line. Two lines in the border are designed in order to reduce the residual layer [106].

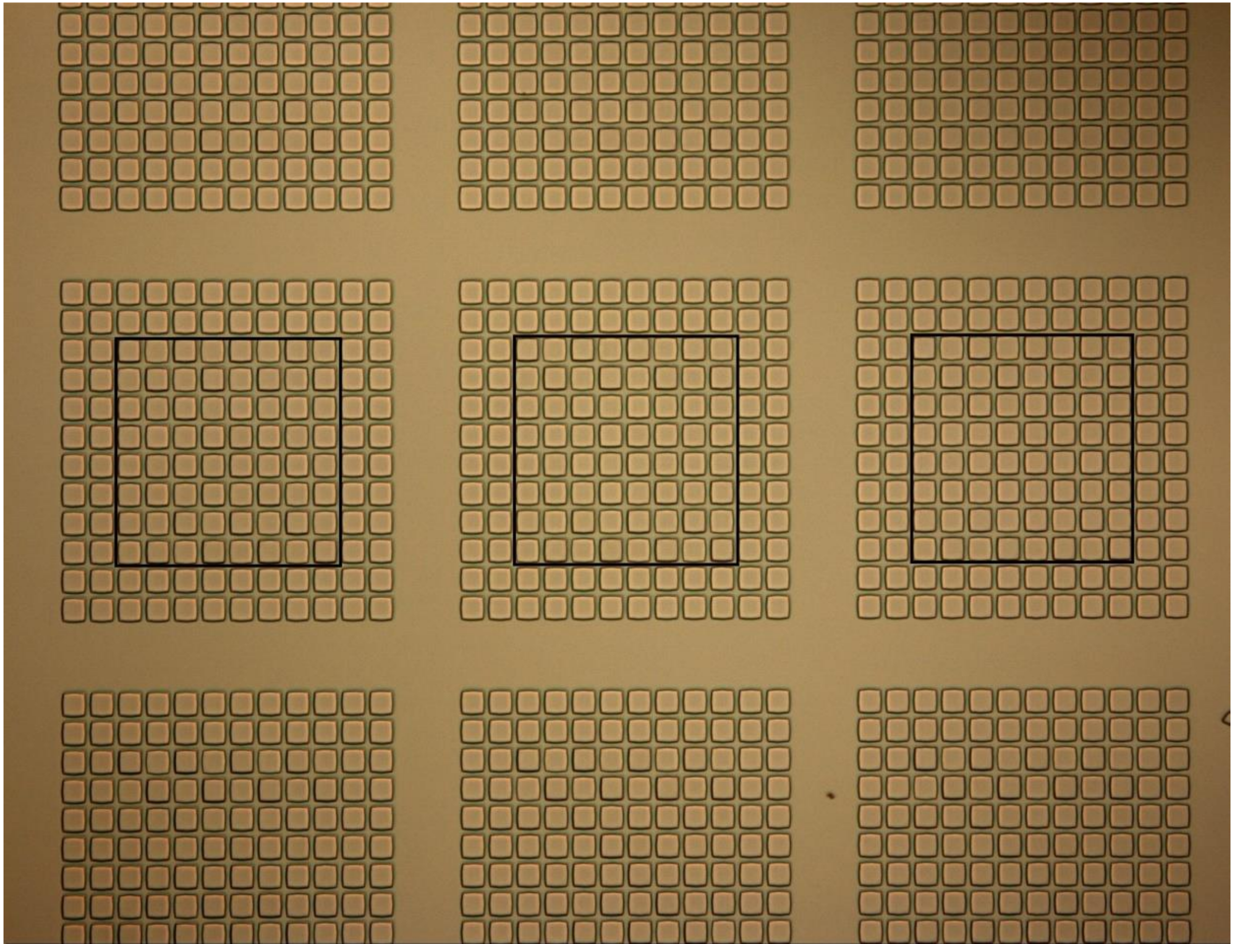

Fig. 5.2 Schematic of mesa structures of 3D master template observed by Leica Microscope. Each mesa cavity has the size 40x40 μm and the gap between each cavity is 10 μm

Figure 5.3 shows the WLI measurement of the topography of master template stored different heights. The 3D image (bottom) shows the different structure heights of the master template.

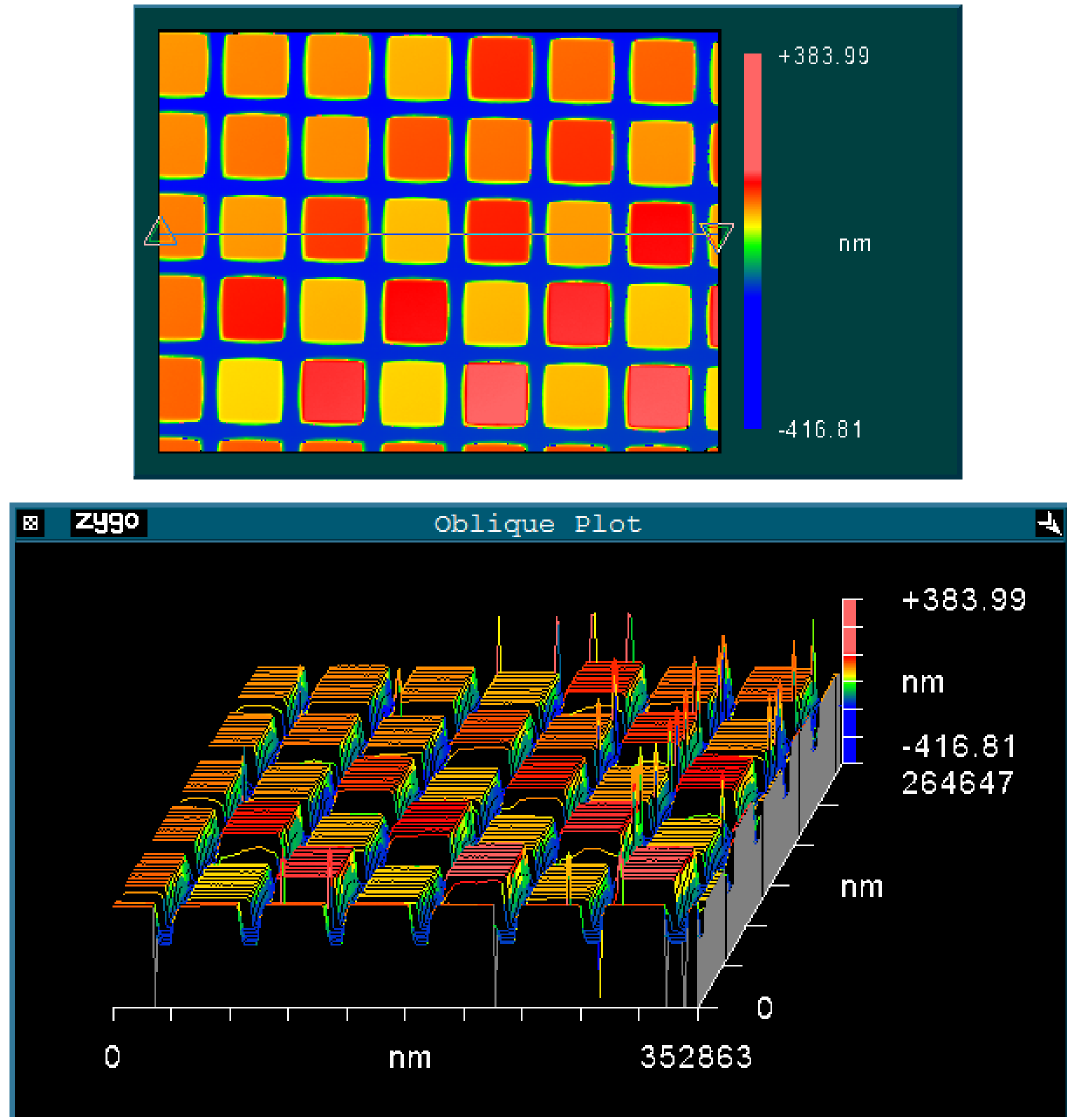

Fig. 5.3 White light interferometry measurement: 2D (top) and 3D (bottom) topography of 3D master template which contains arrays of different positive heights.

5.2.2 Discussion of the experimental result

Inhomogeneous etching

Table 5.1-5.2 show the measured heights of mesa array after 3rd and 4th etching step, respectively. In the 4th etching step, some mesa heights are designed to grown 16 nm (mark as red) and others will not change the height, theoretically.

Table 5.1 Measured heights (nm) of mesa arrays of master template after 3rd etching step.

506	400	506	400	506	400	506	400
400	506	400	506	400	506	400	506
474	432	474	432	474	432	474	432
432	474	432	474	432	474	432	474
474	432	474	432	474	432	474	432
432	474	432	474	432	474	432	474
506	400	506	400	506	400	506	400
400	506	400	506	400	506	400	506

Table 5.2 Measured heights (nm) of mesa arrays of master template after 4th etching step.

522	405	522	406	506	406	506	405
416	510	416	511	416	512	416	510
490	438	490	438	475	438	477	438
450	477	438	491	450	477	449	478
477	458	493	458	493	441	476	459
441	476	448	478	438	492	448	493
506	416	506	417	506	417	506	407
411	510	405	511	406	522	406	522

From the Table 5.2, it can be seen that not only the mesa heights are grown 16 nm (mark as red), but other mesas also grow approximately 5 nm (mark as yellow), neglecting 1-2 nm for the error of measurement. This unexpected growth is due to the inhomogeneous etching which is the main problem occurred during the RIE process, especially in the process using CH_4/H_2. As shown is Fig 5.4, the mesa covered with photoresist grow Δd (correspond to the etching dept Δd) and other area which is uncovered with photoresist get an etching dept Δd_1 and therefore get the unexpectedly "grow" ($\Delta d-\Delta d_1$). The chemical reaction between GaAs and the reactive gases (CH_4/H_2) might be the reason for this phenomenon [80].

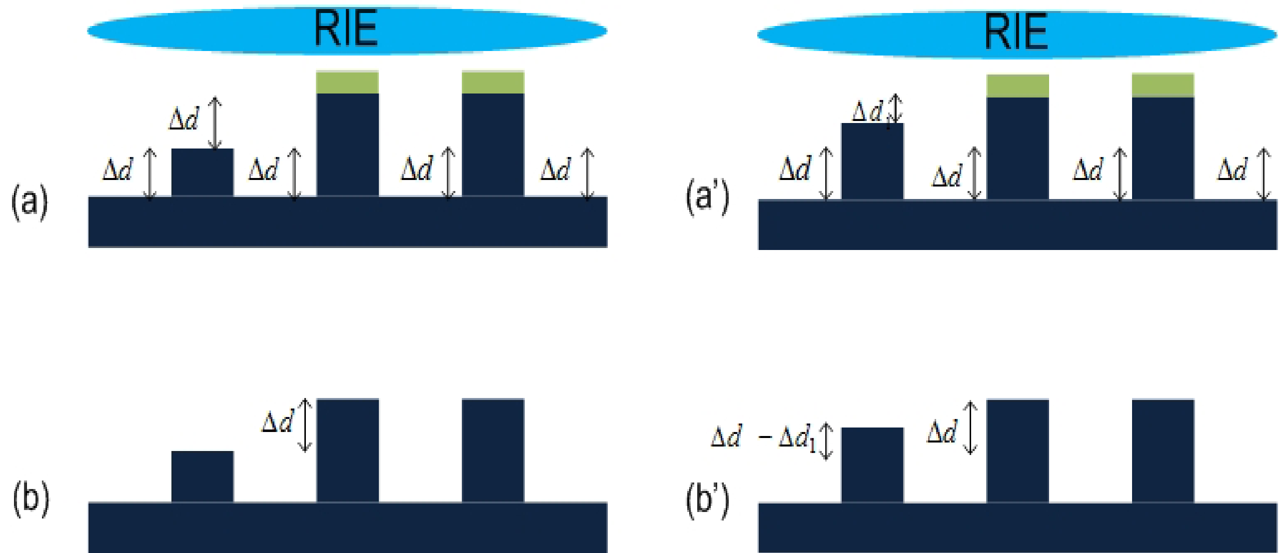

Fig. 5.4 Schematic of inhomogeneous etching of structures on master template using RIE: (a) homogeneous RIE with etching depth Δd, (b) remove photoresist, the mesa grows Δd; (a') inhomogeneous RIE with etching depth Δd_1 for first left mesa and Δd for other uncover area, (b') remove photoresist, two right mesa grow Δd and first left mesa grow ($\Delta d - \Delta d_1$).

The inhomogeneous etching is mostly occurred from the 3rd etching step and the unexpected grow in each step will accumulate the total unexpected grow at the end. This leads to the slightly inaccuracy of experimental result compared to the design as shown in Fig. 5.5. Due to the inhomogeneous etching, the experimental height is slightly higher than designed height.

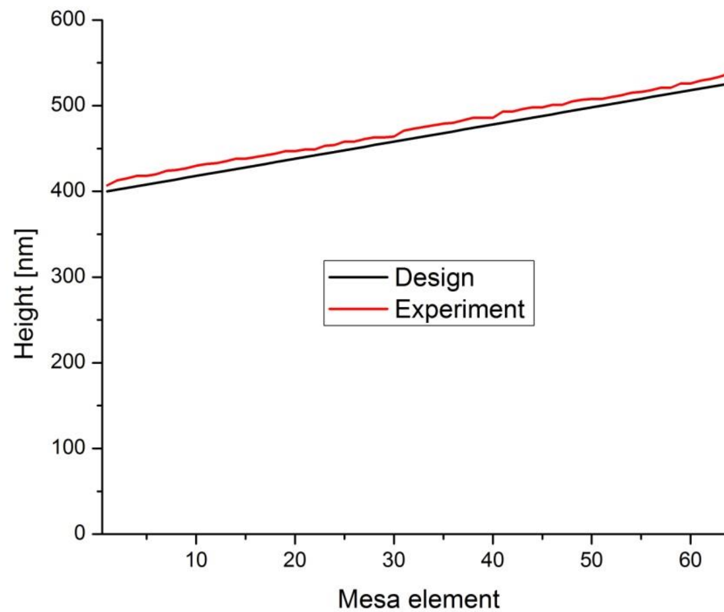

Fig. 5.5 Schematic of designed and experimental heights of master template

The slightly fluctuation on the experimental curve is due to (i) the inhomogeneous etching as mentioned above, (ii) the error of the measurement with WLI (1-2 nm).

5.3 Soft stamp replication

Since the SCIL works with the soft stamp, therefore a copy of the master template on a polymeric material need to be done. This polymeric material used in this replication is polydimenthysiloxane (PDMS) which is a silicon-based organic polymer prepared by mixing certain amounts of base and agent. Two types of PDMS are used for the replication process: soft PDMS (s-PDMS) and the hard PDMS (h-PDMS).

The replication process can be summarized in Fig. 5.6 below:

Fig. 5.6 Schematic of SCIL template replication process: (i) Deposition of anti-adhesive layer on the master template, (ii) Dispensing of PDMS: h-PDMS is coated and s-PDMS is poured, (iii) Positioning of the glass carrier on the master template coated with PDMS and curing of PDMS at 50°C on MRT, (iv) Separation of the master template and the glass carrier [107].

Fig. 5.7 shows the WLI result of the soft template replicated from the master template:

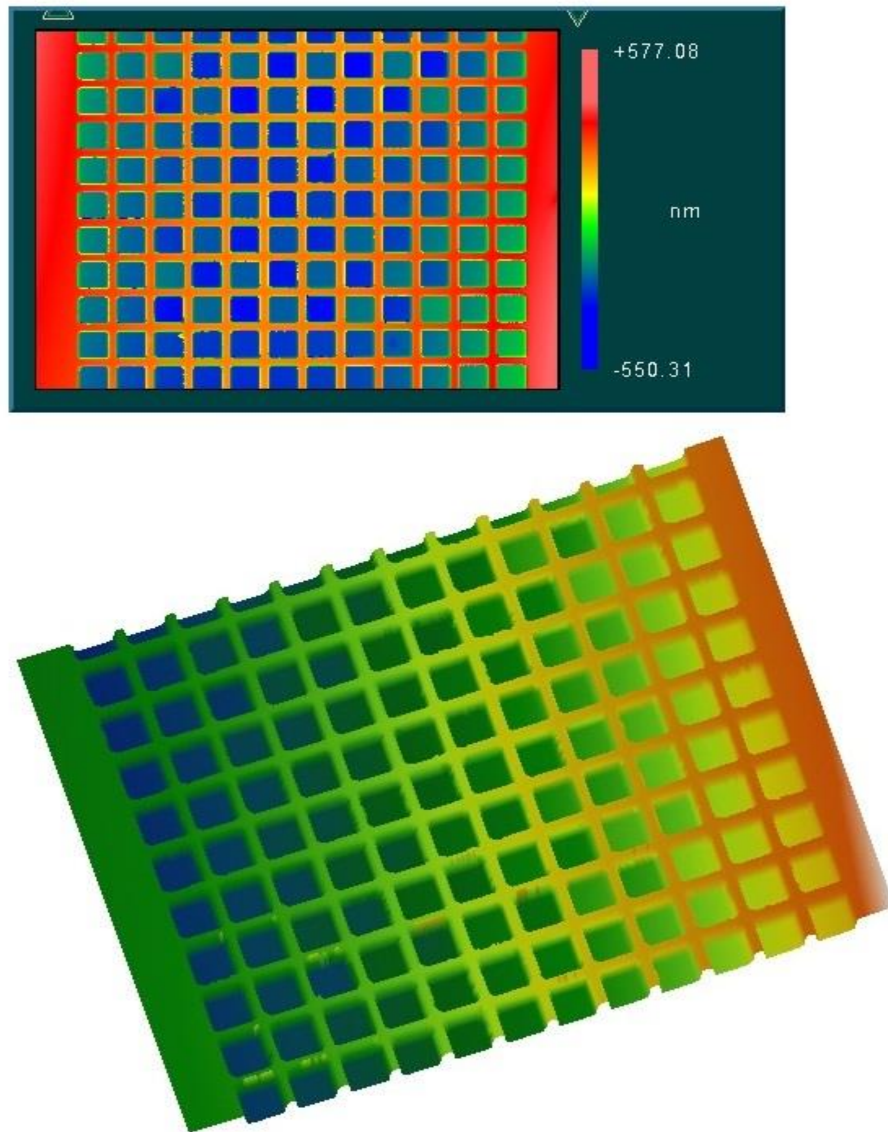

Fig. 6.6 Schematic of soft mold replicated from the master template: 2D with WLI (top) and 3D with Gwyddion software (bottom) with negative different heights of mesa structure.

The comparison of positive structure heights on master template and negative structure height on soft mold is very important study for the FP filter fabrication since the cavity heights, which define the filter transmission lines, are transferred from the soft mold. Fig. 6.7 shows the schematic of master template heights and soft mold heights.

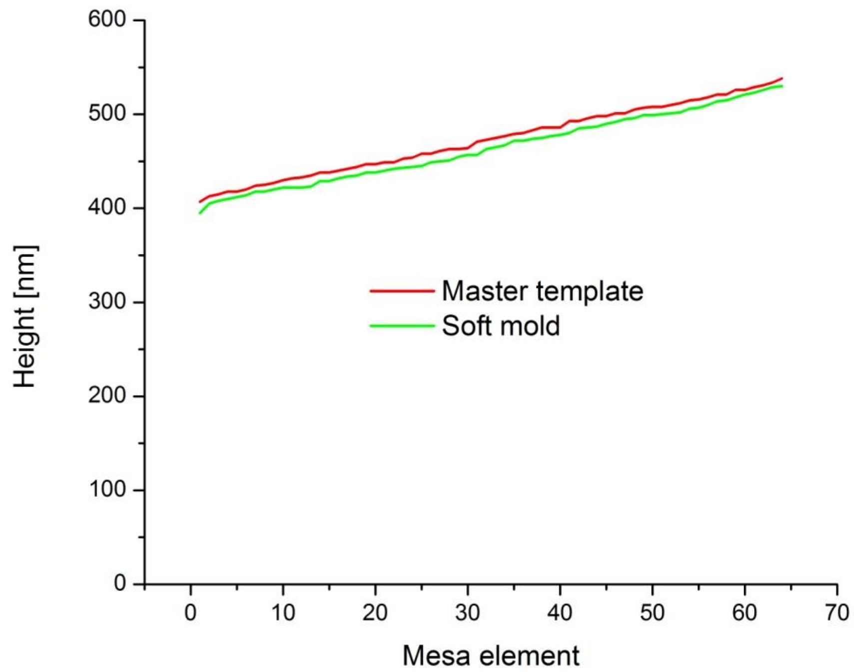

Fig. 5.7 Schematic of mesa heights of master template and soft mold

Fig. 5.7 reveals that the mesa heights of soft mold are slightly lower than the mesa heights of master template. This is due to the elastic property of the PDMS which influences the replication process, i.e. reducing the replicated efficiency.

6. Fabrication and characterization of static filter arrays for the near infrared range

In the previous chapters, we have discussed about the technological fabrication for DBRs and NIR master template. The master templates were successfully fabricated for NIR. These master templates are then replicated in soft stamps for SCIL process. This chapter reports the fabrication and characterization of FP filter arrays for NIR spectral range with different cavity designs: double spin coating resist for cavity, hybrid cavity combined thin oxide layers with resist and applying novel resist for cavity.

6.1 FP filter arrays fabricated by the method using multiple spin coating

As mentioned in previous chapter, the cavity thickness is directly proportional with the center wavelength and defined as $\frac{\lambda_c}{4n}$ with λ_c is the designed wavelength and n is the refractive index of the cavity material. To fabricate the NIR FP filter, it is required to generate cavity heights in the range of 1 µm thickness using 3D nanoimprint. However, the quality of cavity structures depend on the quality of initial spin coated resist layer and the available viscosity of UV-Curable resist [37], [36]. Considering a distinct viscosity, the applied spinning frequency is limiting the resist layer thickness. High thickness requires low spin frequency; however, low frequency will degrade the homogeneity of resist layer and the quality of imprinted structures. To overcome this drawback and to obtained extended homogeneous cavities for FP filter arrays in NIR spectral range, the method using multiple spin coating is applied to generate the extended cavity heights.

Fig. 6.1 shows the schematic of structuring FP filter cavity using multiple spin coating. In this method, the multiple layer cavities are structured using

subsequently spin coating steps. The thickness of each resin layer in each individual spin coating process is d_1 (nm), d_2 (nm)… d_n (nm). Thus, the total cavity thickness is $d = d_1 + d_2 +…+ d_n$ ideally. The spin coating time depends on the desired individual thickness. Note that the last resin layer has to thick enough to receive the cavity structure by SCIL process.

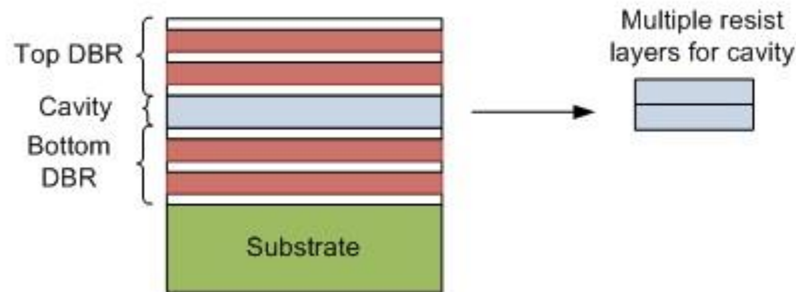

Fig. 6.1 Schematic of FP filter with multiple resist layer for cavity

6.1.1 Fabrication process of FP filter with cavity structured by multiple spin coating process

Parameters of NIR FP filters:

- 9.5 periods (Si_3N_4/SiO_2) are deposited by Plasma Enhanced Chemical Vapor Deposition (PECVD) for the bottom and top DBR.
- The UV-Curable resist mr-UVCur06 is used for cavity layer.

The fabrication process of FP filter with cavity structured by multiple resist layers following few steps: First, the bottom DBR is deposited on a detector array or on a transparent substrate which is combined with a detector array afterwards. Next, the multiple spin coating is performed to get the desired initial cavity thickness, and then the 3D nanoimprint process is applied on the last resist layer using a 3D nanoimprint mold that contains the negative cavities structures.

Finally, the top DBR is deposited on the top of nanoimprinted cavities. This fabrication process is shown in Fig. 6.2.

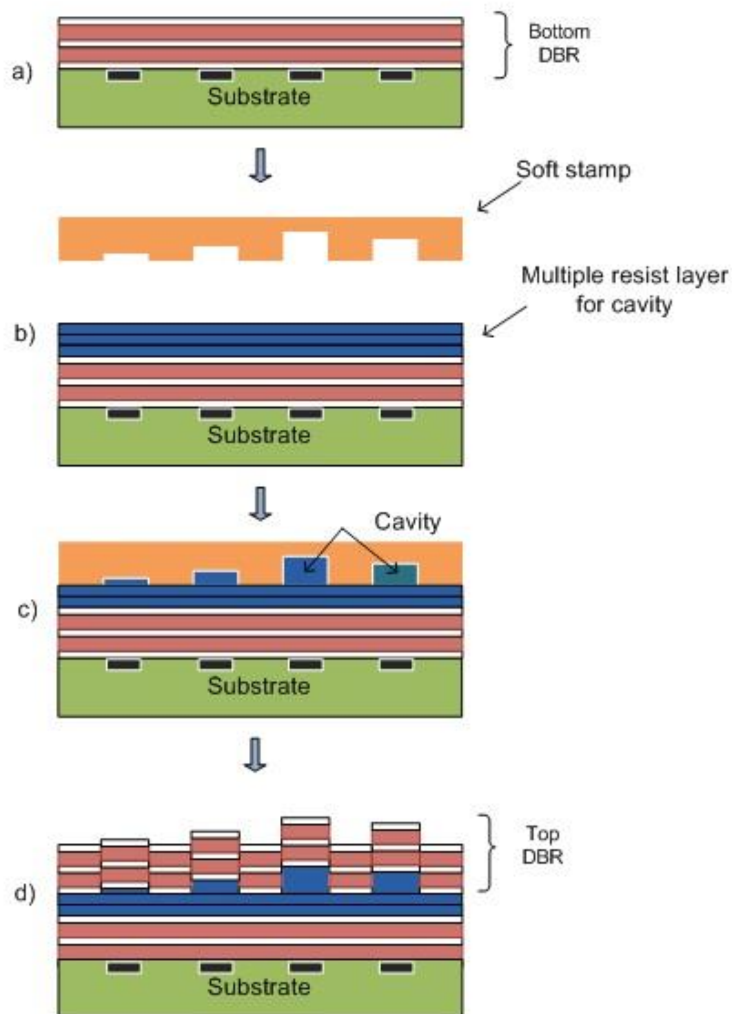

Fig. 6.2 Schematic of FP filter arrays fabrication with multiple resist structure for cavity: (a) deposit bottom DBR, (b) and (c) spin coating multiple resist layer and applied 3D nanoimprint, (d) deposit top DBR

6.1.2 Optical characterization of FP filter arrays fabricated by multiple spin coating method

Fig. 6.3 depicts the transmission property of FP filter fabricated for the spectral range 1.4 – 1.5 µm, the filters are designed with 9.5 periods Si_3N_4/SiO_2, the DBRs are deposited by PECVD and mr-UVCur06 is used for cavity layer.

A maximum transmission line >90 % and the average value >70% are observed. The lowest FWHM of approx. 5 nm can be achieved.

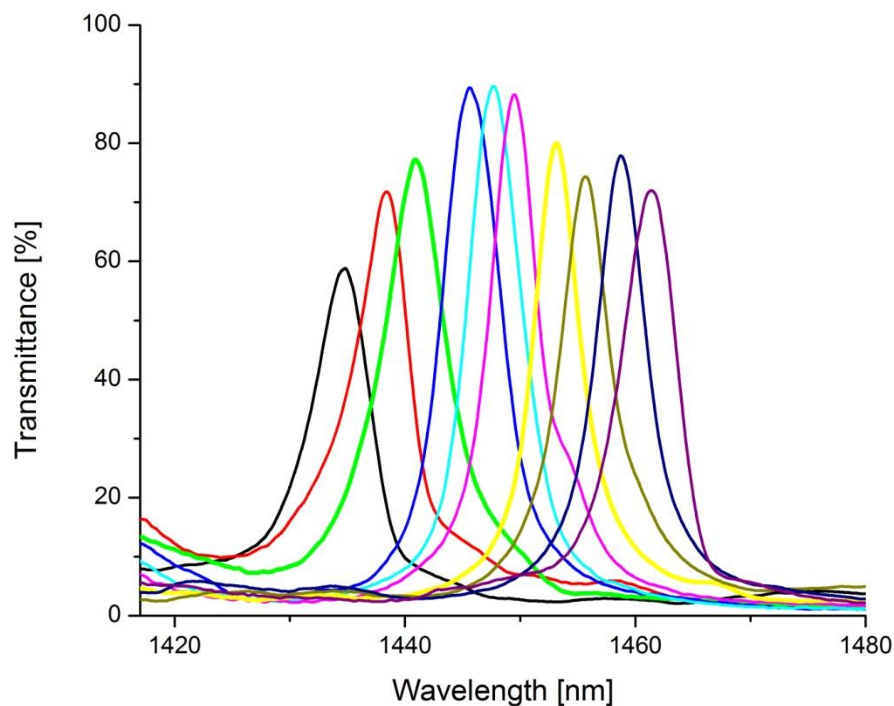

Fig. 6.3 Optical transmission spectra of FP filter arrays using spin coating twice for the cavity layer. In this figure, only some typical filter transmission lines out of 64 spectrally different lines are shown to avoid overloading.

6.1.3 Results and discussion

Fig 6.4 depicts the comparison of theoretical and measured transmission of FP filters array designed and fabricated for spectral range 1.4 – 1.5 µm. The first

observation is that the experimental spectral lines are general lower than the simulation. The reason behind this phenomenon is the absorption of the cavity layers.

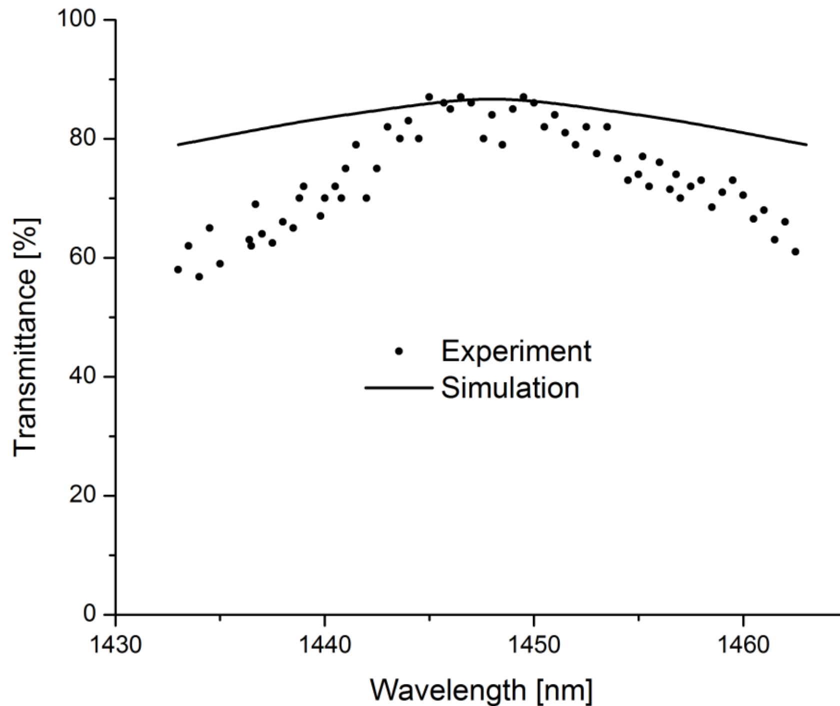

Fig. 6.4 Comparison of simulated and experimental transmittance of the FP filter lines. The filters have been fabricated using spin coating twice for the cavity layer.

Fig. 6.4 reveals that the experimental results are generally lower than the simulated values. This is due to in the theoretical model calculation, the ideal situation is considered, the following points involved in reality are neglected: (i) influence of plane wave fronts in the cavities during the measurements, (ii) the influence of the interface roughness causing interface scattering loss, as well as (iii) absorption and Rayleigh scattering. Note that, the optical absorption of the involved resist materials is measured zero for the optical absorption in the considered spectral range using spectroscopic ellipsometry. Thus, the theoretical

model calculations have been carried out without absorption within the resist materials. However, absorption can never be completely zero in reality.

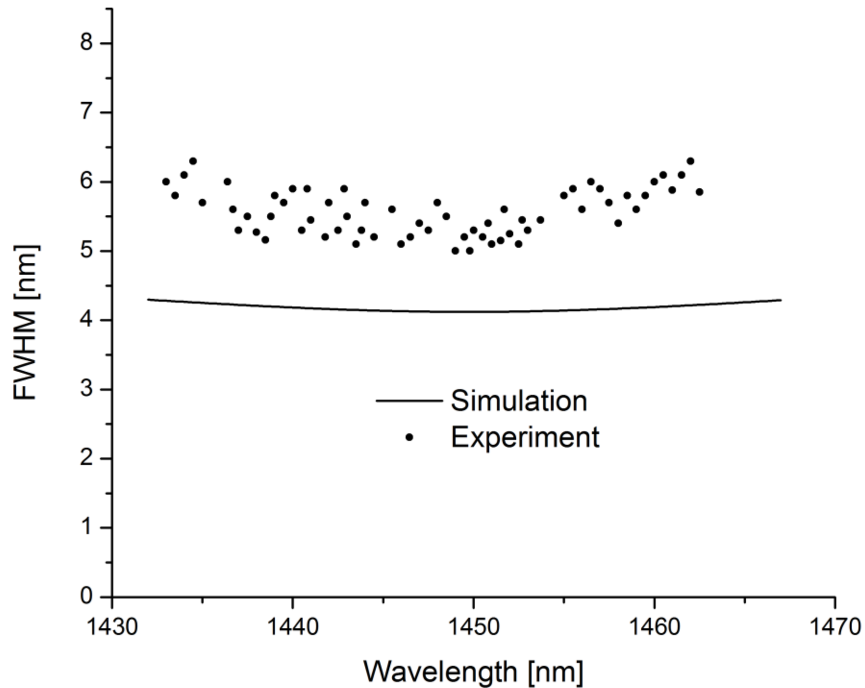

Fig. 6.5 Comparison of measured and simulated FWHM from filter arrays using spin coating twice for the cavity layer

Fig. 6.5 shows the comparison of measured and simulated FWHM from filter arrays using spin coating twice for the cavity layer. The experimental values are generally larger than the simulated results. This is due to the limitations in theoretical model calculation as mentioned above.

6.2 FP filter arrays fabricated by the method using hybrid cavity

In the chapter 6.1, the methodology to fabricate the FP filters using multiple spin coating for structuring the extended cavity. In this chapter, another method to get the extended cavity is presented using hybrid cavity, i.e. combination of thin

oxide layers and the organic cavity. Fig 6.6 shows the structure of a FP filter with hybrid cavity structure.

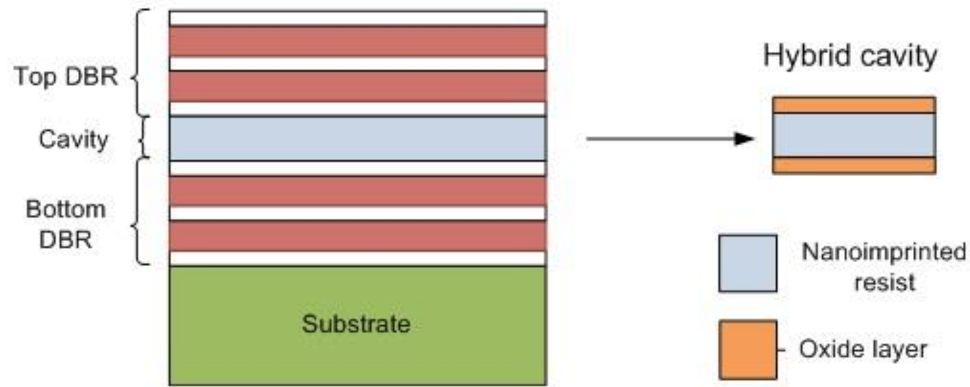

Fig. 6.6 Schematic of a FP filter with hybrid cavity structure

6.2.1 Fabrication process of FP filters using the method using hybrid cavity for structuring cavity

The following parameters are used for FP filters using hybrid cavity:

- 9.5 periods (Si_3N_4/SiO_2) deposited by PECVD.
- Spectral range designed: 1.4 – 1.5 µm.
- Cavity material: combination of SiO_2 and mr-UVCur06.
- The additional thin oxide layers (SiO_2) are deposited by PECVD.

Fig. 6.7 shows the fabrication process of FP filters using hybrid cavity: First, the bottom DBR is deposited on the glass substrate, then the first thin oxide layer SiO2 is deposited on the top of bottom DBR, afterward the resist mr-UVCur06 is coated on the top of thin oxide layer and next the 3D nanoimprint is applied to transfer the structure from the soft stamp onto resist layer, then the second thin oxide layer is deposited on the top of resist layer and finally the top DBR is deposited.

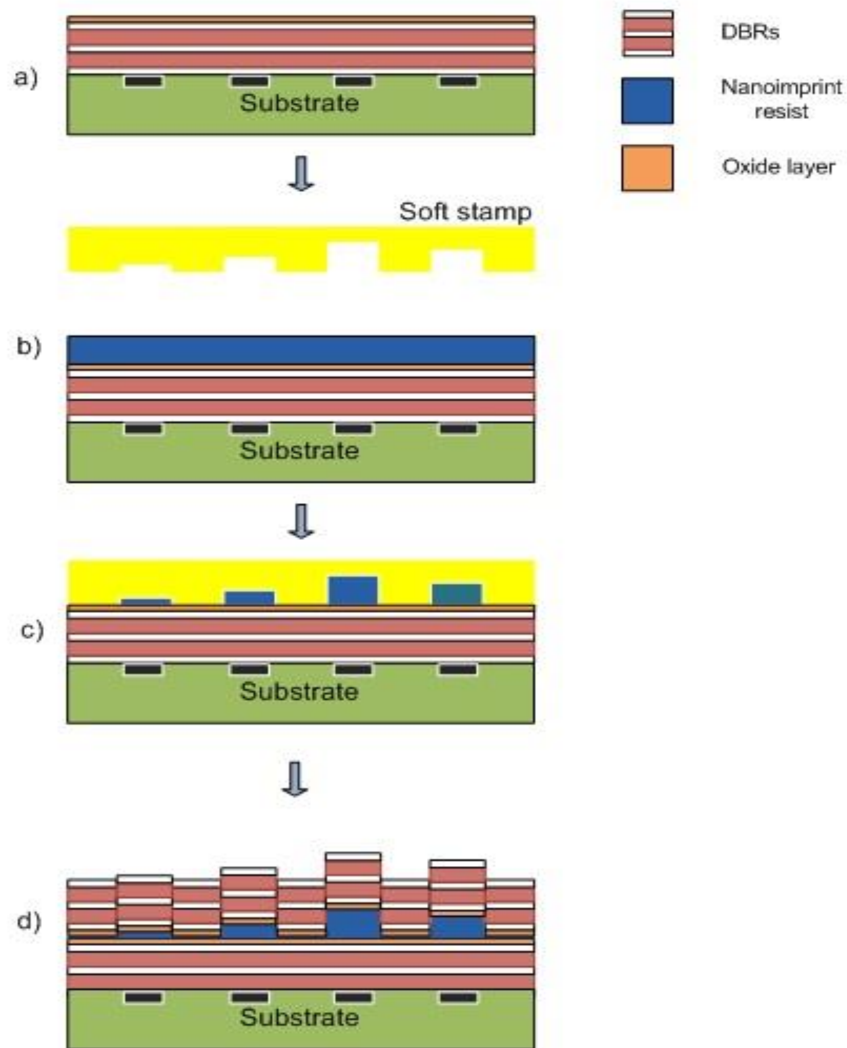

Fig. 6.7 Schematic of fabrication of FP filter arrays with hybrid cavity structure: (a) deposit bottom DBR and first oxide layer, (b) and (c) spin coating resist layer and apply 3D nanoimprint, (d) deposit second oxide layer and top DBR

6.2.2 Optical characterization of FP filter arrays using hybrid cavity

Fig 6.8 shows the transmission property of FP filter arrays using hybrid cavity for the spectral range 1.4 – 1.5 µm. A high maximum transmission >90% and an average transmission value above 70 % can be achieved.

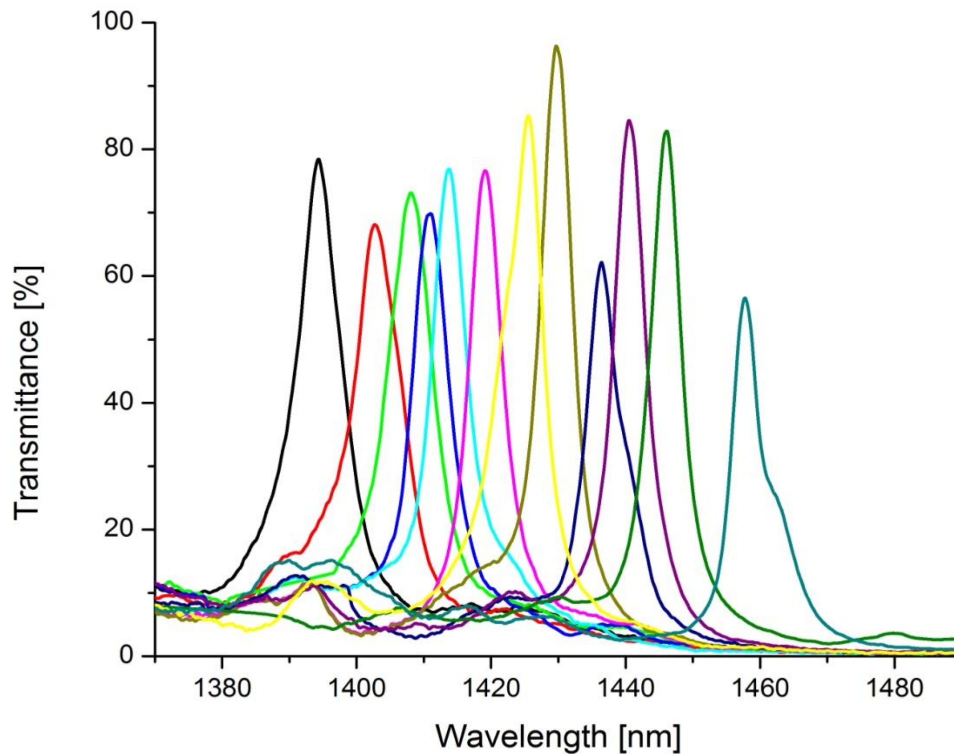

Fig. 6.8 Optical transmission spectra of filter arrays including the hybrid cavities. In this figure, only some typical filter transmission lines out of 64 spectrally different lines are shown to avoid overloading.

6.2.3 Results and discussion

Fig 6.9 shows the comparison of theoretical calculation and measured optical transmission of FP filter arrays designed and fabricated for spectral range 1.4 – 1.5 µm. Due to the limitations in model calculation as mentioned above (6.1.3), the measured transmission spectra are general smaller than the model calculation. The presence of SiO_2 in cavity structure might be the reason for the fluctuation in experimental data and mismatch in the shapes of simulated and experimental transmittance profiles.

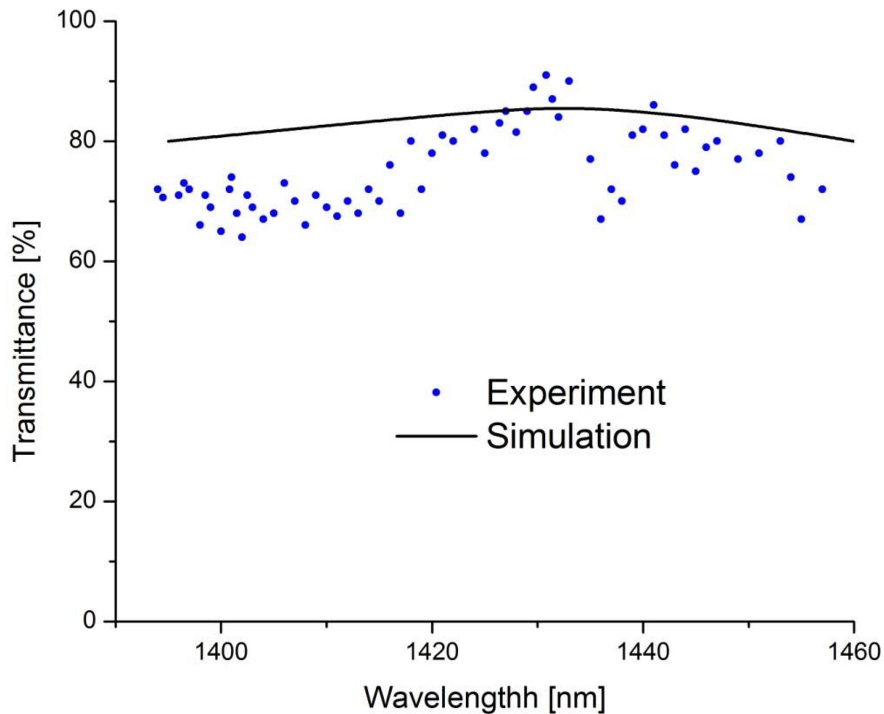

Fig. 6.9 Comparison of simulated and experimental transmittance of the FP filter lines. The filters have been fabricated using hybrid cavity

Fig 6.10 shows the theoretical calculation and measured FWHM of FP filter arrays using hybrid cavity in spectral range 1.4 – 1.5 µm. The first observation is that the experimental FWHM are general larger than simulated results. This phenomenon is partly due to the limitations in theoretical model calculations (mentioned in 6.1.3). Moreover, the surface roughness inside the cavity structure has to be considered. In layered heterostructures, these surface roughnesses are incorporated (slightly modified) into interface roughnesses. Note that surface roughness respectively interface roughness also exist for SiO_2 layers deposited by PECVD. Previously, the measurements on SiO2 oxide layers deposited by different technological methods [108] recorded by a profilemeter and AFM revealing an rms of below 3 nm for this situation.

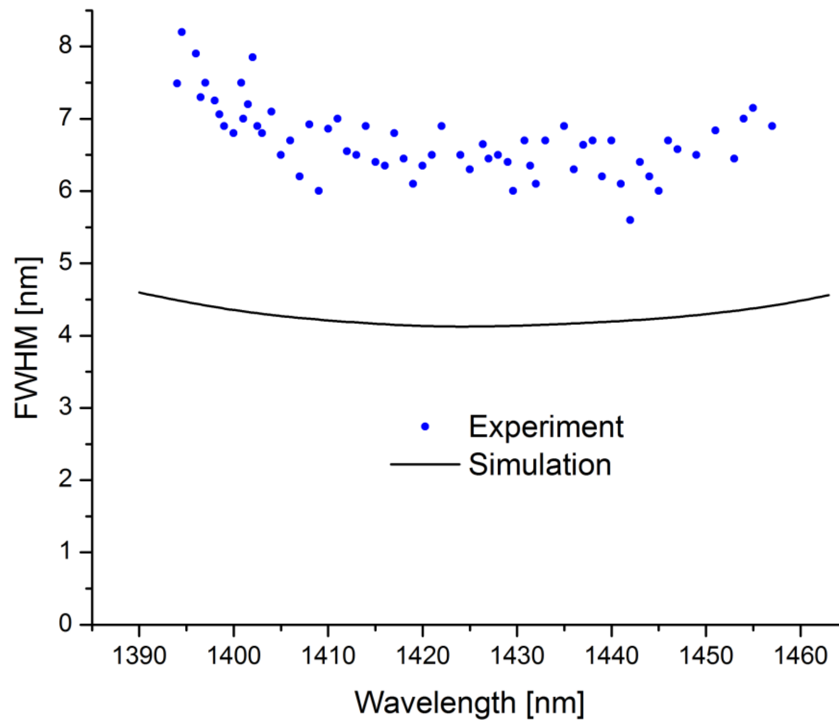

Fig. 6.10 Comparison of measured and simulated FWHM of filter arrays using hybrid cavity

6.3 FP filter arrays fabricated by the method using novel resist mr-NIL210

In the previous part 6.1 and 6.2, the FP filter arrays fabricated by the methods using multiple spin coating and hybrid cavity for extended cavity structure have been presented. However, these two methods still have the disadvantages, i.e. the interface roughness in multiple cavity layers' structure and high cost in fabrication due to multiple processes for cavity.

From the disadvantage mentioned above in multiple layers of the cavity structure. It is needed to find a novel resist which has fast curing in SCIL process and gives the high initial thickness layer by single spin coating. In co-operation

with Micro resist technology GmbH, the novel resist mr-NIL210 was investigated and applied to fabricate the NIR FP filters.

6.3.1 Investigation of novel resist mr-NIL210 for SCIL process

The height resolution of cavity structures depends sensitivity on the quality of the initially spin coated UV-Curable resist layers and the available viscosity of UV-Curable resist [36], [37].

Fig. 6.11 shows the coating recipe of Amonil, mr-UVCur06 and novel resist mr-NIL210. From this figure, we can see that the conventional resists (Amonil and mr-UVCur06) can give the thickness from 150 to 600 nm with the spin coater speed from 1000 to 5500 rpm while the cavity thickness required for NIR FP filter is from 250 to 800 nm. Note that, for a homogeneous resist layer it is required to work with spin coater at high frequency. Thus, for the required cavity height of NIR FP filters, the conventional resists are not suitable. The novel resist mr-NIL210, however, can give a higher thickness compared to conventional resists at the same spin frequency. This guarantees for a homogeneous resist layer and therefore, resulting a good imprinted structure.

Fig. 6.12 shows the imprint structures of mr-UVCur06 (left) and mr-NIL210 (right) using the same initial thickness (500 nm) and imprint parameters (exposure time and delay time). The imprint profiles (bottom) show the deformation of imprint structure of the resist mr-UVCur06 (a meniscus shape rather than a mesa shape) and a good imprint structure of resist mr-NIL210 (bottom right) indicated by a mesa shape. This deformation is due to the uncompleted full fill the mold during imprint process.

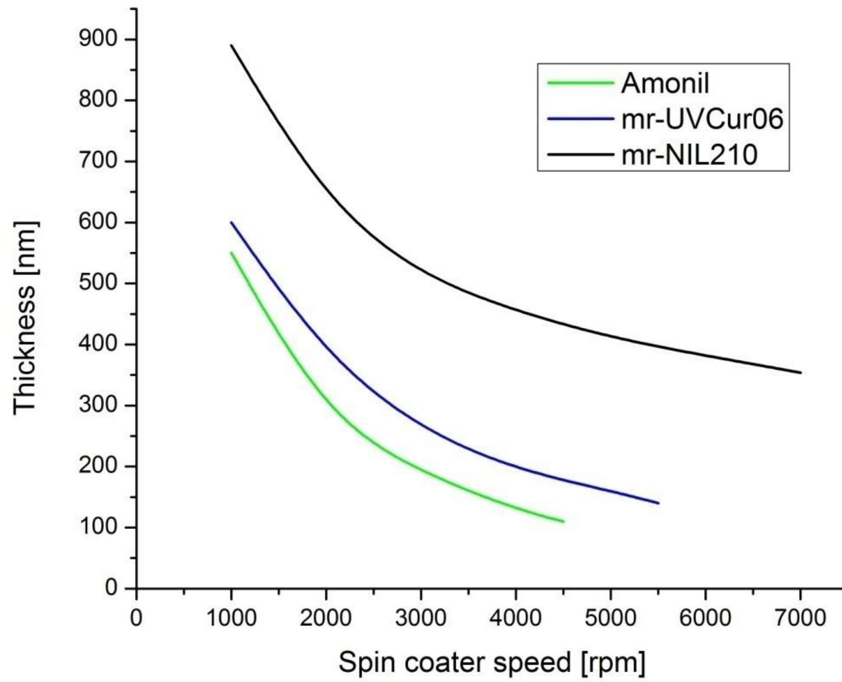

Fig. 6.11 Spin curve behavior of conventional resists and novel resist mr-NIL210

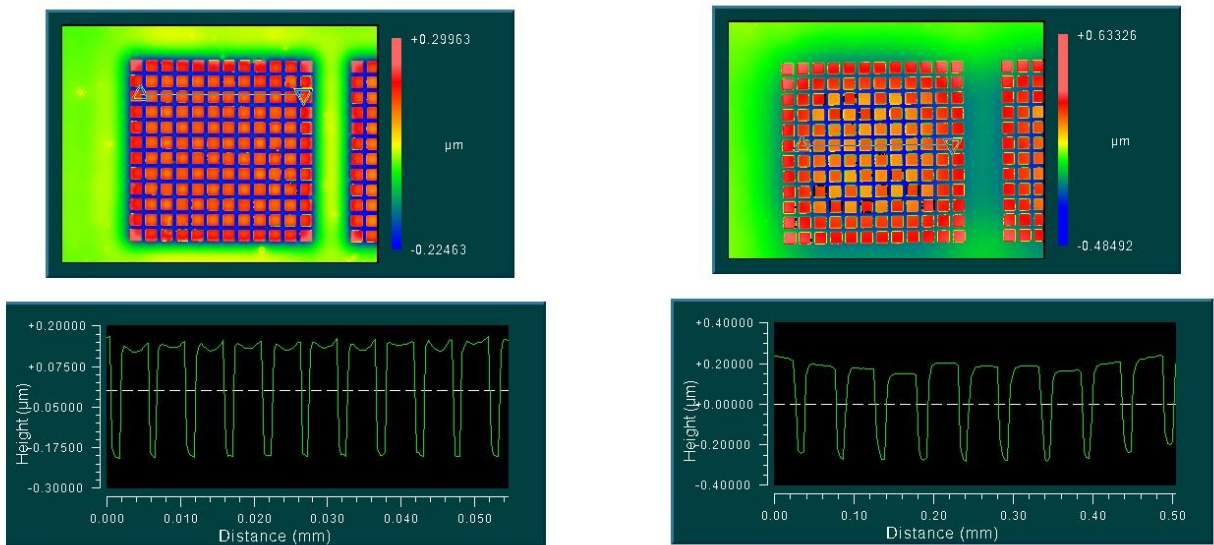

Fig. 6.12 Schematic of imprint structures of mr-UVCur06 (left) and mr-NIL210 (right)

6.3.2 Fabrication process of FP filter arrays using novel resist mr-NIL210

In this method, the FP filter arrays are fabricated following parameters:

- 9.5 periods (Si_3N_4/SiO_2) for DBRs deposited by PECVD.
- Using mr-NIL210 for cavity layer.

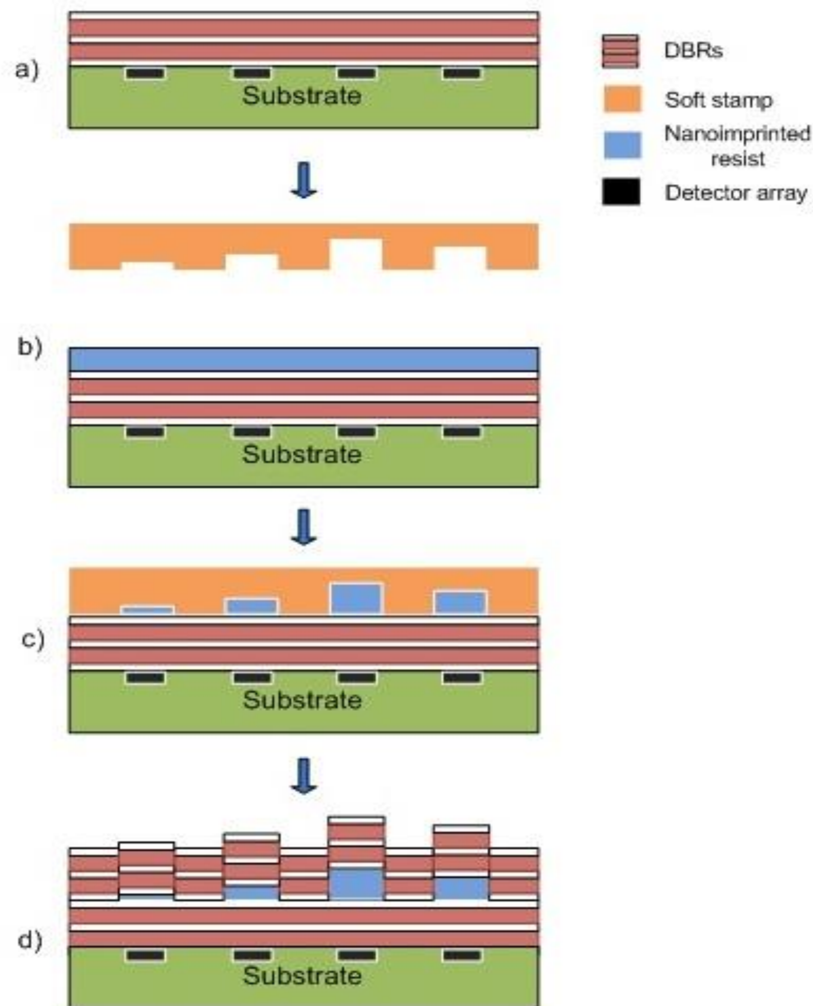

Fig. 6.13 Schematic of fabrication of FP filter arrays using novel resist for cavity layer: (a) deposit bottom DBR, (b) and (c) spin coating resist layer and apply 3D nanoimprint, (d) deposit top DBR

The fabrication process of FP filter arrays comprises the following steps: First, the bottom DBR is deposited on a transparent substrate which is combined with

detector arrays afterwards. Next, the 3D nanoimprint is performed using soft stamp that contains the negative cavities structures. Finally, the top DBR is deposited on the top of nanoimprinted cavities.

6.3.3 Optical characterization of FP filter arrays using novel resist mr-NIL210

Fig. 6.14 shows the optical transmission property of FP filter arrays fabricated for the spectral range 1.4 – 1.5 μm. A maximum transmission up to >90% and an average value of >70% can be achieved. The smallest FWHM 4.7 nm at the wavelength 1458 nm is observed.

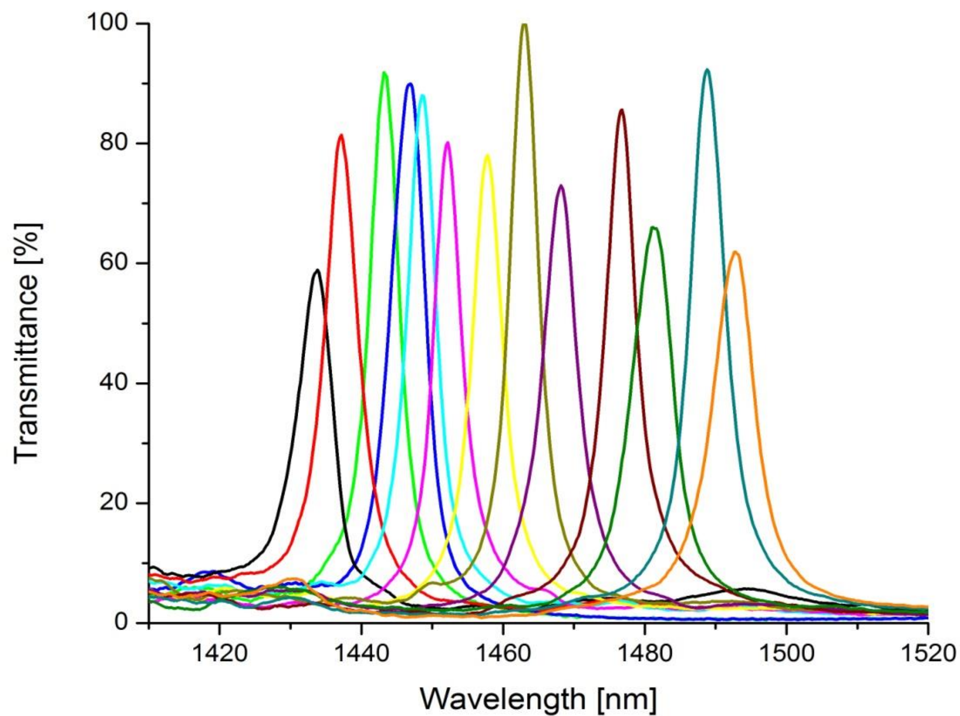

Fig. 6.14 Optical transmission properties of FP filter arrays using the novel resist mr-NIL210. In this figure, only some typical filter transmission lines out of 64 spectrally different lines are shown to avoid overloading.

6.3.4 Result and discussion

Fig. 6.15 shows the comparison between simulated and measured transmittance at the maximum of the filter transmission lines. Due to the limitations in theoretical model calculation, the experimental values are generally smaller than simulated results. The fluctuation in experimental data and mismatch of the shapes in simulated and experimental transmittance might be caused by: (i) the cavity material mr-NIL210 might have wavelength dependent absorption which has been neglected in the simulation, this absorption could lead to the undulation presented in the experimental result in Fig. 6.15; (ii) the surface roughness of the cavities could lead to wavelength dependent scattering.

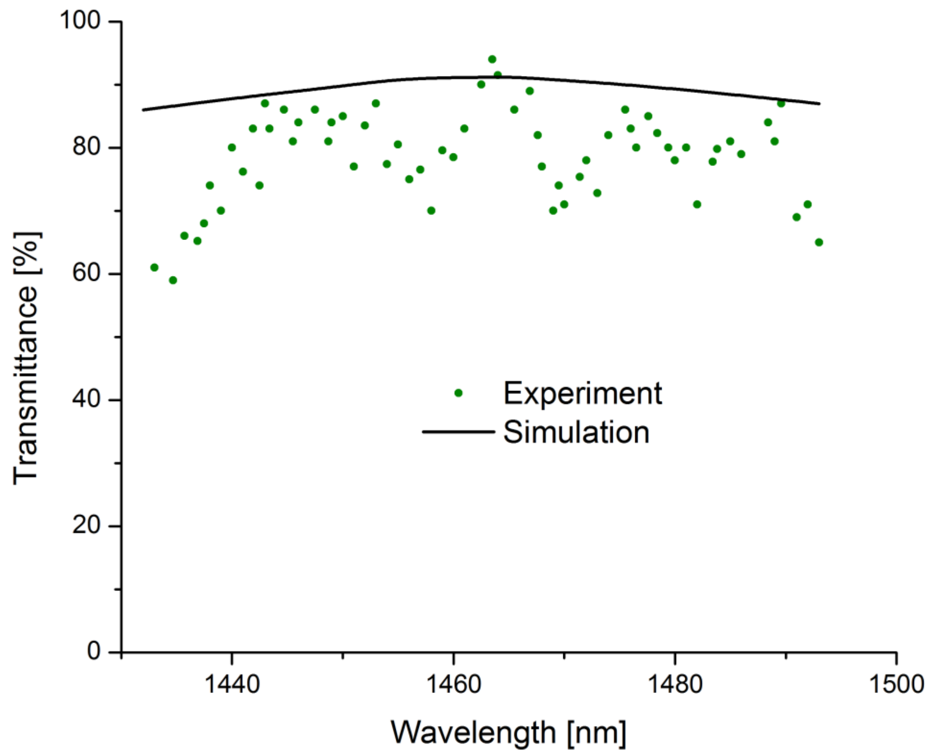

Fig. 6.15 Comparison of simulated and experimental transmittance of the FP filter lines. The filters have been fabricated using novel resist for the cavity layer.

In Fig. 6.16, the simulated and experimental FWHM are compared. Since the limitations mentioned in 6.1.3, the experimental data are larger than simulated data.

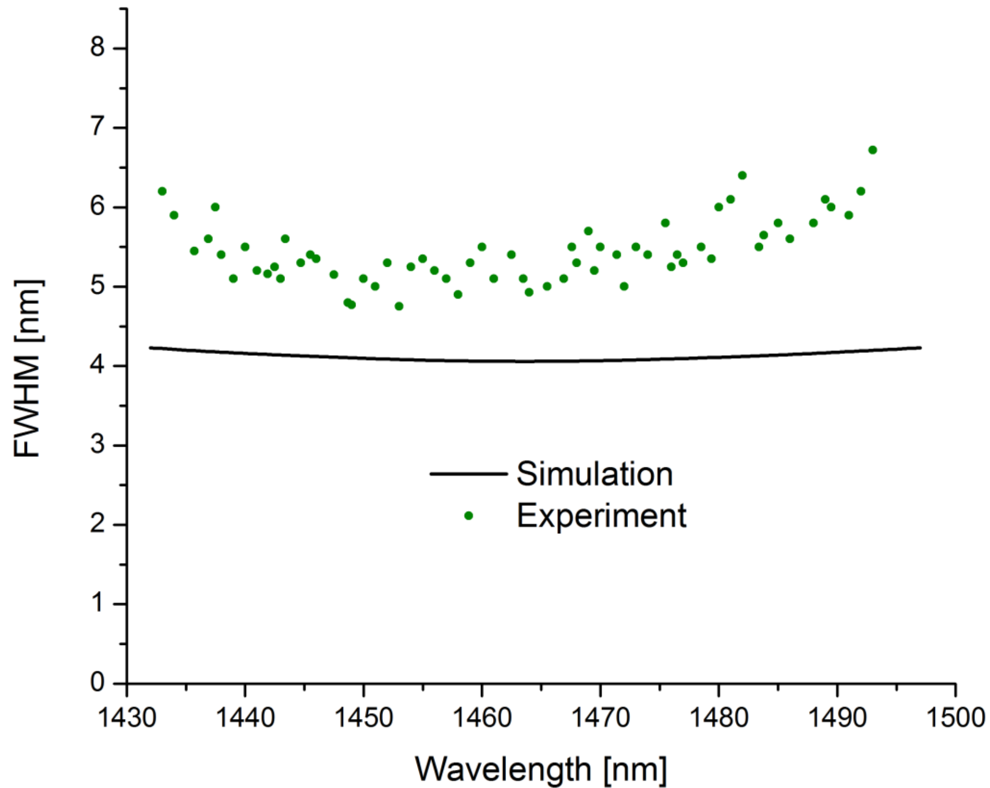

Fig. 6.16 Comparison of measured and simulated FWHM of FP filter arrays using novel resist mr-NIL210 for the cavity layer

6.4 Characterization of the three FP filter fabrication methods of NIR FP filter arrays

6.4.1 Comparison of the technological effort for the three FP filter fabrication methods

Using the multiple coating and the hybrid cavity design, the working of conventional resist mr-UVCur06 at unfavorable spin frequency can be avoided

and therefore reduce the degradation in homogeneity of the resist layer which enables a better 3D nanoimprint result. However, these two methods take more effort to control the total cavity thickness since each individual layer generates an error which accumulate to an error of the total cavity thickness and lead to a shift of the filter transmission line at the end. The consequences observed in the optical transmittance property of FP filters including the hybrid cavity shown in Fig. 6.8. The optical transmission spectra of the filter arrays are shifted to smaller wavelength since the total cavity thickness is lower than the designed thickness. In contrast, the third method using the novel resist material mr-NIL210 saves time and cost in fabrication of FP filter arrays since it requires only a single spin coating step to define the desired initial resist layer thickness and also reduces the effort in controlling the cavity thickness. The higher the number of potential error sources the higher the required effort to control the thickness of the total cavities in practice.

6.4.2 Surface roughness in the heterostructure of cavity

The heterostructure of cavity in the methods using multiple spin coating and hybrid cavity not only takes an extra cost and time during fabrication process but exist also higher surface roughness compared to the method using novel resist. This surface roughness affects to the propagation of light in FP filter, i.e. changing the incident angle, and therefore, causing the loss which reduces the transmitted intensity of FP filters.

Figs. 6.17-6.18 show the surface profile of single layer mr-UVCur06 and double layers mr-UVCur06 measured by AFM.

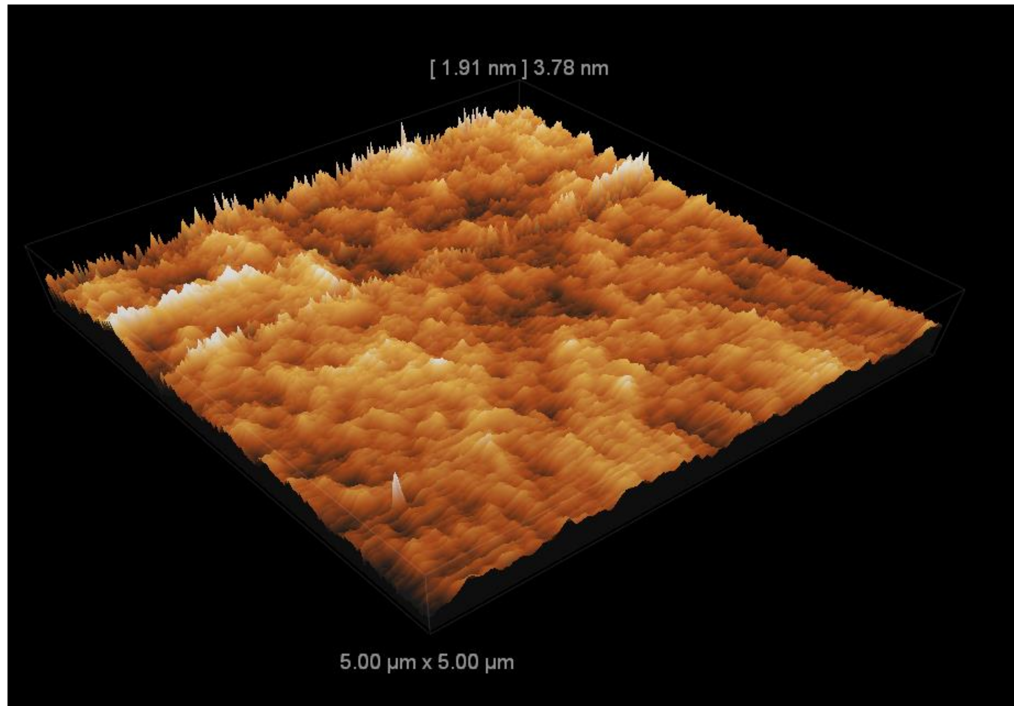

Fig. 6.17 Surface profile of single resist layer mr-UVCur06. The total scan length is 5µmx5µm and the highest point on the profile is 3.78 nm.

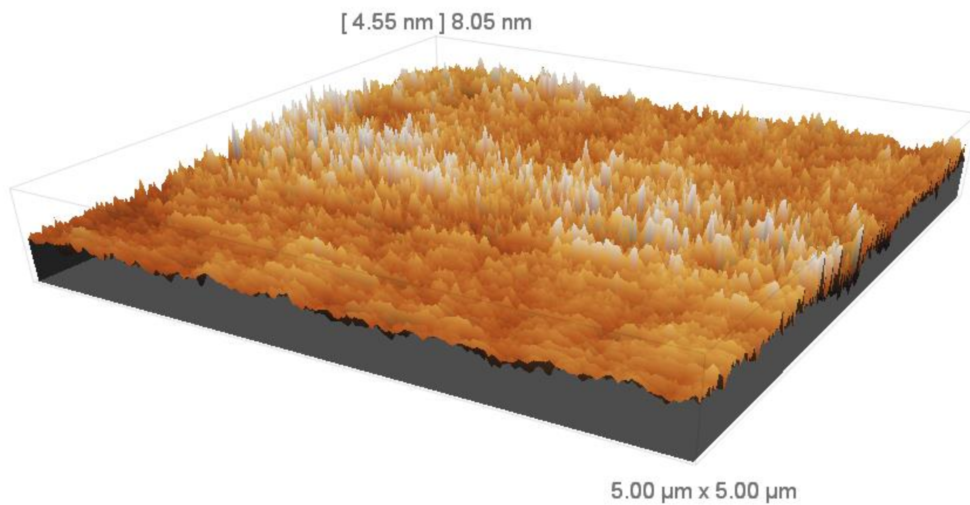

Fig. 6.18 Surface profile of two layers mr-UVCur06. The total scan length is 5µmx5µm and the highest point on the profile is 8.05 nm.

The results show that the surface roughness is increased when increases the number of resist layer, an rms of below 4 nm for single layer and 8 nm for two layers' resist mr-UVCur06 are observed. The reason behind this phenomenon is in case of heterostructure the surface roughnesses are incorporated (slightly modified) into interface roughnesses. These interface roughnesses are accumulated with the number of the layer in heterostructure.

In case of using hybrid cavity method, the total surface roughness of cavity comprises of one part from resist layer mr-UVCur06 and other part from SiO_2 layer which has the surface roughness of around 3 nm with PECVD deposition [108]. An rms of approx. 10 nm is observed for the hybrid structure as shown in Fig. 6.19.

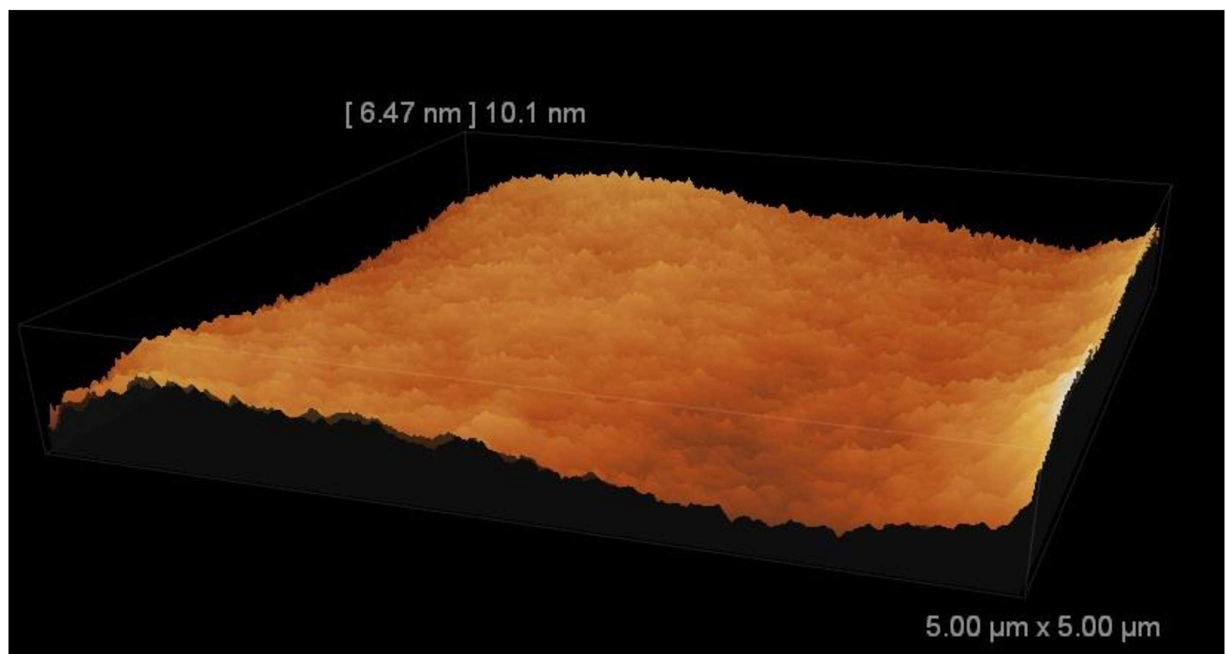

Fig. 6.19 Surface profile of hybrid structure. The total scan length is 5µmx5µm and the highest point on the profile is 10.1 nm

Fig. 6.20 shows the surface roughness of novel resist layer mr-NIL210, an rms of around 4 nm is observed.

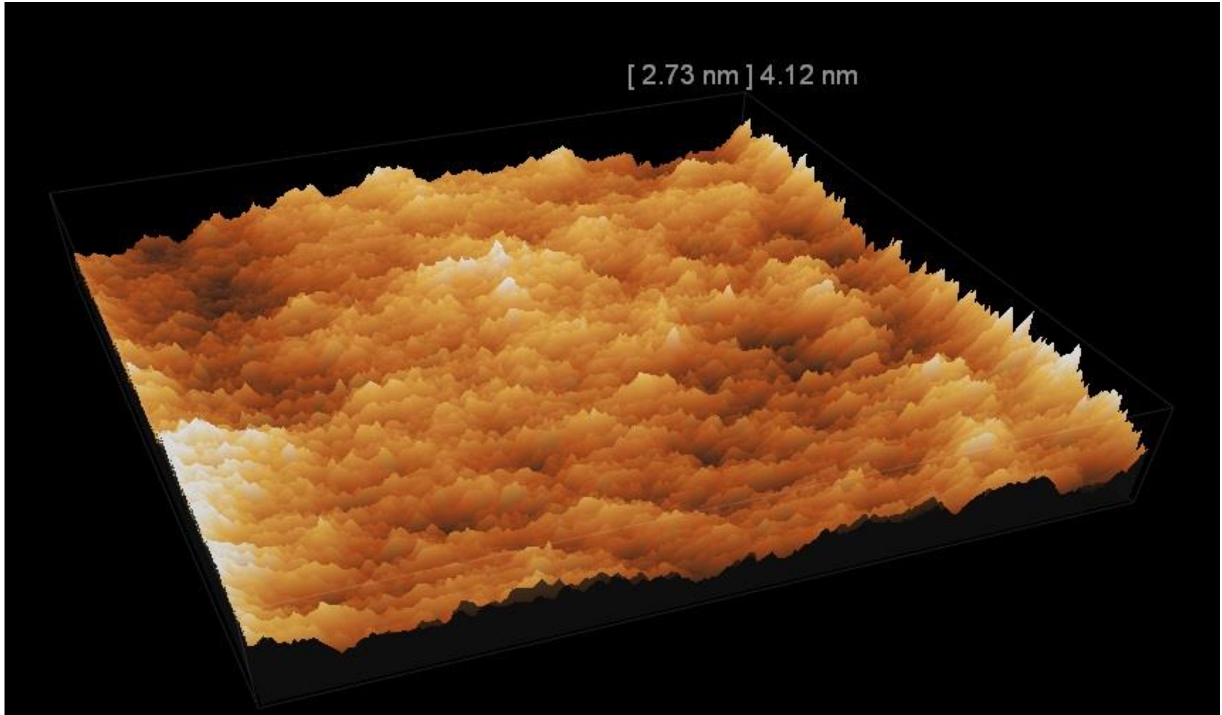

Fig. 6.20 Surface profile of novel resist layer mr-NIL210. The total scan length is 5μmx5μm and the highest point on the profile is 4.12 nm.

The measurement rms of surface roughnesses for three cavity structure mentioned above are summarized in Table 6.2

Tab. 6.2 Surface roughness (in nm) of different cavity structures

Cavity structure	rms (nm)	Number of interfaces
One layer mr-NIL210	≈ 4	2
Two layer mr-UVCur06	≈ 8	3
Hybrid layer	≈ 10	4

From the table, it can be seen that the surface roughness is directly proportional with the number of interfaces of cavity structure. This affects to the optical properties of FP filters, i.e. transmitted intensity and FWHM. Table 6.3 shows the average experimental values of transmitted intensity and FWHM for three FP filter fabrication method reported above.

Tab. 6.3 Average transmitted intensity and FWHM obtained for each FP filter array fabrication method

Specific characteristics of the technological method used	Measured transmitted intensity of the filter transmission line (%)	Measured FWHM of the filter transmission line (nm)	Number of interfaces involved in the cavity
Hybrid cavity	76	6.6	4
Double spin coating	78	5.6	3
Novel resist	82	5.4	2

Table 6.3 reveals that the optical properties of FP filters in the method using hybrid cavity is weaker compared to another two methods, this is due to the presence of SiO_2 inside the cavity structure which increases the number of interfaces and thus, increases the surface roughness of cavity and therefore reduces the optical properties of FP filters. Moreover, the small mismatch refractive index of SiO_2 and the resist mr-UVCur06, which affects to the interference inside cavity, is also a reason for the weaker optical properties.

6.4.3 Effect of high temperature during top DBR deposition

The optical properties of FP filters are not only depending on the interface roughness of the layers included in the cavities but they are also affected by the process conditions during the top DBR fabrication. This process affects the imprinted cavity by (i) temperature, (ii) plasma and (iii) pressure conditions. All

three parameters influence the shrinkage of the resist layer and, therefore, might affect the spectral position of the filter lines at the end.

The imprinted structures are measured before and after the top DBR deposition. We observed a shrinkage of 13.7% for structures defined by the double spin coating using mr-UVCur06, 7.9% for applying the novel resist mr-NIL210 and 4.3% for structures defined by the hybrid cavity combining mr-UVCur06 and SiO2. The reasons behind the lower shrinkage applying the hybrid cavity are on one hand the partial shrinkage of the imprinted structures already occurring during the deposition of the top SiO2 layer for the hybrid cavity and on the other hand the smaller volume of resist existing in the cavity structures. The latter is caused by the fact that the SiO2 layer is counted to the cavity thickness but only the polymer is shrinking. To end up with the targeted cavity heights, the shrinkages have to be considered during the design process of the structures.

7. Summary and outlook

Within this work, the 3D nanoimprint FP filter arrays have been successfully fabricated for NIR range. The homogeneous extended cavity heights have been implemented using different methods, namely the multiple spin coating method, the hybrid cavity method and the novel resist method.

The fabrication of the NIR FP filter arrays comprises few steps. Firstly, the NIR FP filters were simulated with different cavity structures using OpenFilters software. The optical properties of FP filters in each method were characterized and discussed in chapter 4. The results show that the transmission intensity is above 80% and the FWHM is below 5 nm for three FP filter fabrication methods. Compared to the other two methods, the optical properties of hybrid cavity method are weaker since the presence of SiO_2 inside the cavity structure. Secondly, the master templates were fabricated and then replicated for fabrication of NIR FP filters. The inhomogeneous etching and the elastic property of PDMS affect to the fabrication and replication results; these are reported in chapter 6. Finally, the NIR FP filter arrays were fabricated and characterized by technologies reported in chapter 2 and 3: the DBRs were deposited by cheap and fast technology PECVD; the different cavity heights were produced by nanoimprint technology; the FP filters were characterized by free beam broad band confocal setup.

The technological fabricated effort of FP filters was characterized and compared for three FP filter arrays fabrication methods. The multiple spin coating method and the hybrid cavity method take more efforts in fabrication process than the novel resist method since the multiple steps in fabrication such as the multiple coating steps for multiple resist layers or deposited steps of SiO_2 for cavity.

Therefore, these two methods also take more time and cost than the method using novel resist. Furthermore, due to the multiple processes in structuring cavity, the multiple spin coating method and hybrid cavity method have to take more effort in controlling the cavity thickness, since each spin coating step or deposited step generates an error thickness and will be accumulated an total error thickness at the end. This error thickness of cavity leads to the shift of filter transmission line at the end. Another problem for multiple layers of cavity structure is the surface roughness/interface roughness. The multiple layers generate a higher surface roughness than single layer, this surface roughness affect to the optical properties of FP filters, i.e. reduces the transmission intensity and enlarges the FWHM (chapter 6). The novel resist mr-NIL210 method, on the other hand, simpler and cheaper than other two methods since the required initial thickness can be achieved by single spin coating step, which helps to easily control the initial resist layer thickness and provides a low surface roughness of resist layer.

The measured optical properties of FP filter arrays fabricated by three methods are compared and discussed with simulated results. Since the limitation in theoretical model calculation, the simulated results behave a better optical properties compared to measure results, i.e. higher transmission intensity and smaller FWHM. The measured transmission intensity of FP filter arrays for three methods is above 70%. The FWHM of all filter transmission lines is between 4.7 to 8.2 nm and the smallest FWHM is achieved at 1450 nm using the novel resist method. For three FP filter fabrication methods, the measured optical properties of multiple spin coating method are better than the hybrid cavity method and worse than the novel resist method. This related to the cavity structure such as the number of the interface and the presence of SiO_2 which absorb the light and

increase the surface/interface roughness and therefore reduce the transmission intensity and enlarge the FWHM of FP filters.

The behavior of cavities during top DBR fabrication was investigated. Under the high temperature, plasma and pressure condition the cavities are shrunk. This shrinkage is depended on the cavity structure, a shrinkage of 13.7% is observed for structures defined by the double spin coating method, 7.9% for applying the novel resist mr-NIL210 and 4.3% for structures defined by the hybrid cavity method. This shrinkage of cavity heights leads to the shift of filter transmission lines at the end, therefore, it has to be considered during design process to end up with the targeted cavity heights.

In summary, FP filter arrays for the spectral range between 1.4 and 1.5 µm have been implemented for the first time demonstrating that it is feasible to fabricate homogeneous extended cavities with 3D nanoimprint technology. Thus, low cost, strongly miniaturized, high optical resolution FP filter arrays for the NIR spectral range as important elements of nanospectrometers are achievable. For future work, the mechanical stability of cavity layer should be investigated. This mechanical stability is expected to be strongly influenced by the number of interfaces and material adhesion of two materials forming a heterointerface.

APPENDIX

Appendix A

Spin coating process of photoresist and polymers

A.1 Spin coating process for patterning the positive photoresist AZ1518 with optical photolithography

Table A.1: process flow for patterning the AZ1518 photoresist.

Dry H_2O	120 °C hot-plate	10 min
Coating Ti-Prime	4000 rpm	40 s
Coating AZ1518	4000 rpm	40 s
Soft-bake	90 °C hot-plate	5 min
Exposure	Mask aligner	6.6 s
Development	0.8% KOH	30 s
O2 Plasma	50 Watt	3 min

A.2 Spin coating process for patterning the UV-Curable organic polymer mr-UVCur06

Table A.2.1: process flow for single spin coating mr-UVCur06 to generate 200 nm resist layer

Dry H_2O	150 °C hot-plate	20-25 min
Coating Ti-Prime	3000 rpm	30 s
Coating mr-UVCur06	3000 rpm (~200 nm)	60 s
Soft-bake	80 °C hot-plate	60 s

Table A.2.2: process flow for spin coating twice (double spin coating) mr-UVCur06 to generate 400 nm resist layer

Dry H_2O	150 °C hot-plate	20-25 min
Coating Ti-Prime	3000 rpm	30 s

Coating mr-UVCur06	3000 rpm (~200 nm)	60 s
Soft-bake	80 ^oC hot-plate	60 s
Explosure	UV lamp	>5 min
Coating mr-UVCur06	3000 rpm (~200 nm)	60 s
Soft-banke	80 ^oC hot-plate	60 s

A.3 Spin coating process for patterning the novel resist mr-NIL210 to generate 500 nm resist layer

Dry H_2O	150 ^oC hot-plate	20-25 min
Coating mr-NIL210	3000 rpm	60 s
Soft-bake	100 ^oC (~500 nm)	60 s

Appendix B

Thin Film deposition process by PECVD

Table B.1 Process parameters of deposition Si_3N_4 Film

Gas source 1 flow	2% Silane (SiH_4) in N_2	1000 sccm
Gas source 2 flow	Ammoniac (NH_3)	20 sccm
RF generator 1	13.56 MHz / pulsed mode	20 Watt / 19 sec
RF generator 2	130 kHz / pulsed	20 Watt / 6 sec
Pressure		0.65 Torr
Temperature		120 ^oC

Table B.2 Process parameters of deposition SiO_2 Film

Gas source 1 flow	2% Silane (SiH_4) in N_2	430 sccm
Gas source 2 flow	Nitrous Oxide (N_2O)	710 sccm
RF generator 1	13.56 MHz / continuous mode	20 Watt
RF generator 2	130 kHz	-
Pressure		1 Torr
Temperature		120 ^oC

Appendix C

Process flow of master template fabrication using GaAs
C1. Cleaning:

a. Acetone, iso-propanol; dry with N_2
b. O_2-plasma asher, 250 Watt / 5 min

C2. Lithography

a. Dry H_2O: hot-plate 120 ^oC / 10 min
b. Spin-coating: 1) Ti-Prime (40 s, 4000 rpm); 2) AZ1518 (40 s, 4000 rpm)
c. Prebake: hot-plate 90 ^oC / 5 min (exact)
d. Alignment and exposure: Suss MicroTec MA4, Mask INA-SA 5 (Mask 1 to 7) /6.6 s
e. Development: KOH 0.8% / 30 (approx.); rinse with H_2O; dry with N_2
f. Hardbake: hot-plate, 120 ^oC / 5 min (approx.)

C3. Measurement: Microscope

C4. Descum process: O_2-plasma asher, 50Watt / 2 min

C5. Etching: RIE – Oxford: CH_4(6)H_2(36)sccm / 150W / 0.008 Torr / 20 ^oC

C6. Remove photoresist:

a. Put in NMP on hot-plate 80 ^oC for at least 8 hours
b. Vibration the container NMP with 80% ultrasound power / 2 min
c. Rinse with iso-propanol

C7. Measurement: Microscope; White Light Interferometer

LIST OF ABBREVATIONS

AFM	Atomic Force Microscopy
CCD	Charged-Coupled Device
CMOS	Complementary Metal-Oxide-Semiconductor
CNP	Combined Nanoimprint and Photolithography
DBR	Distributed Bragg Reflector
EBL	Electron Beam Lithography
FWHM	Full Width at Half Maximum
IBSD	Ion Beam Sputter Deposition
IC	Integrated Circuit
IR	Infrared
ITRS	International Technology Roadmap for Semiconductors
INA	Institute of Nanostructure Technologies and Analytics
LED	Light Emitting Diodes
MBE	Molecular Beam Epitaxy
MEMS	Miro-Electro-Mechanical System
MIMIC	Micromolding in Capillaries
NIL	Nanoimprint Lithography
nTP	Nanotransfer Printing
OPD	Optical Path Difference
PhC	Photonic Crystal
PECVD	Plasma Enhanced Chemical Vapor Deposition
R2RNIL	Roll to Roll Nanoimprint Lithography
REM	Replica Molding
RF	Radio frequency
RIE	Reactive Ion Etching
RMS	Root Mean Square
SCCM	Standard Cubic Centimeters per Minute
SCIL	Substrate Conformal Imprint Lithography
S-FIL	Step-and-Flash Imprint Lithography
UV	Ultraviolet
UV-NIL	UV Nanoimprint Lithography
VASE	Variable Angle Spectroscopic Ellipsometry
WLI	White Light Interferometry
µCP	Microcontact Printing
µTM	Microtransfer Molding

CHEMICAL ELEMENTS

Al	Aluminum
AlGaAs	Aluminum Gallium Arsenide
Ar	Argon
CH_4	Methan
GaAs	Gallium Arsenide
H_2	Hydrogen
HF	Hydrofluoric acid
InP	Indium Phosphide
KOH	Potassium Hydroxide
N_2	Nitrogen
NH_3	Ammonia
NMP	1-Methyl-2-pyrrolidone
O_2	Oxygen
PDMS	Polydimethylsiloxane
SF_6	Sulfur Hexafluoride
Si	Silicon
SiO_2	Silicon dioxide
Si_3N_4	Silicon Nitride
TiO_2	Titanium Dioxide

BIBLIOGRAPHY

[1] C. Fernandez, C. Astier, E. Rock, J. B. Coulon, and J. L. Berdagué, "Characterization of milk by analysis of its terpene fractions," Int. J. Food Sci. Technol., vol. 38, no. 4, pp. 445–451, 2003.

[2] A. J. M. Pemen and P. C. T. van der Laan, "On-line detection of partical discharges in statorwindings of large turbine generators"," Proc. IEE Colloq. Discharges Large Mach., pp. 3/1–3/4, 1998.

[3] W. W. Parson, Modern Optical Spectroscopy: With Exercises and Examples from Biophysics and Biochemistry, vol. 1. Springer, 2007.

[4] Nikolai V. Tkachenko, Optical Spectroscopy: Methods and Instrumentations. Elsevier, 2006.

[5] F. Graham Smith, T. A. King, and D. Wilkins, Optics and Photonics: An Introduction, 2nd Edition. John Wiley & Sons, 2007.

[6] B. Schrader, B. Dippel, I. Erb, S. Keller, T. Löchte, H. Schulz, E. Tatsch, and S. Wessel, "NIR Raman spectroscopy in medicine and biology: results and aspects," J. Mol. Struct., vol. 480–481, pp. 21–32, May 1999.

[7] C. Zhang and J. Su, "Application of near infrared spectroscopy to the analysis and fast quality assessment of traditional Chinese medicinal products," Acta Pharm. Sin. B, vol. 4, no. 3, pp. 182–192, Jun. 2014.

[8] K. Kong, C. Kendall, N. Stone, and I. Notingher, "Raman spectroscopy for medical diagnostics - From in-vitro biofluid assays to in-vivo cancer detection.," Adv. Drug Deliv. Rev., vol. 89, pp. 121–134, 2015.

[9] A. Paudel, D. Raijada, and J. Rantanen, "Raman spectroscopy in pharmaceutical product design," Adv. Drug Deliv. Rev., vol. 89, pp. 3–20, 2015.

[10] W. E. Moerner, "A Dozen Years of Single-Molecule Spectroscopy in Physics, Chemistry, and Biophysics," J. Phys. Chem. B, vol. 106, no. 5, pp. 910–927, Feb. 2002.

[11] D. R. Walt, "Optical Methods for Single Molecule Detection and Analysis," Anal. Chem., vol. 85, no. 3, pp. 1258–1263, Feb. 2013.

[12] R. Karoui and J. De Baerdemaeker, "A review of the analytical methods coupled with chemometric tools for the determination of the quality and identity of dairy products," Food Chem., vol. 102, no. 3, pp. 621–640, 2007.

[13] A. J. Berger, I. Itzkan, and M. S. Feld, “Feasibility of measuring blood glucose concentration by near-infrared Raman spectroscopy,” Spectrochim. Acta Part A Mol. Biomol. Spectrosc., vol. 53, no. 2, pp. 287–292, Feb. 1997.

[14] Y. Wang, D. C. Alsmeyer, and R. L. Mccreery, “Raman Spectroscopy of Carbon Materials: Structural Basis of Observed Spectra,” Chem. Mater., vol. 2, no. 5, pp. 557–563, 1990.

[15] D. Brennan, J. Alderman, L. Sattler, J. Walshe, J. Huang, B. O’Connor, and C. O’Mathuna, “Development of a micro-spectrometer system for process control application,” Infrared Phys. Technol., vol. 43, no. 2, pp. 69–76, 2002.

[16] W. Wang and J. Paliwal, “Near-infrared spectroscopy and imaging in food quality and safety,” Sens. Instrum. Food Qual. Saf., vol. 1, no. 4, pp. 193–207, Oct. 2007.

[17] H. Lin and Y. Ying, “Theory and application of near infrared spectroscopy in assessment of fruit quality: a review,” Sens. Instrum. Food Qual. Saf., vol. 3, no. 2, pp. 130–141, Apr. 2009.

[18] B. Fairuz, Ahmad Omar and B. Zubir, Mohd Matjafri, “Optical Sensor in the Measurement of Fruits Quality : A Review on an Innovative Approach,” Int. J. Comput. Electr. Eng., vol. 1, no. 5, pp. 557–561, 2009.

[19] S. R. Delwiche, “Protein Content of Single Kernels of Wheat by Near-Infrared Reflectance Spectroscopy,” J. Cereal Sci., vol. 27, no. 3, pp. 241–254, May 1998.

[20] J. G. P. W. Clevers, “The use of imaging spectrometry for agricultural applications,” ISPRS J. Photogramm. Remote Sens., vol. 54, no. 5–6, pp. 299–304, Dec. 1999.

[21] J. S. Bao, Y. Z. Cai, and H. Corke, “Prediction of Rice Starch Quality Parameters by Near-Infrared Reflectance Spectroscopy,” J. Food Sci., vol. 66, no. 7, pp. 936–939, 2001.

[22] P. Maja, Š. Martin, Š. Dejan, and Č. Potokar Marjeta, “Application of near infrared spectroscopy to predict chemical composition of meat and meat products,” Technol. Mesa, vol. 51, no. 2, pp. 133–142, 2010.

[23] H. Cen and Y. He, “Theory and application of near infrared reflectance spectroscopy in determination of food quality,” Trends Food Sci. Technol., vol. 18, no. 2, pp. 72–83, 2007.

[24] J.P. Smith, "Spectrometers get small - Miniature spectrometers rival benchtop instruments," Anal. Chem., vol. 72, p. 653A–658A, 2000.

[25] R. F. Wolffenbuttel, "MEMS-based optical mini- and microspectrometers for the visible and infrared spectral range," J. Micromechanics Microengineering, vol. 15, no. 7, pp. S145–S152, Jul. 2005.

[26] T. Kwa and R. Wolffenbuttel, "Integrated Grating Detector Array Fabricated in Silicon Using Micromachining Techniques," Sensors and Actuators a-Physical, vol. 31, no. 1–3, pp. 259–266, 1992.

[27] S. H. Kong, D. D. L. Wijngaards, and R. F. Wolffenbuttel, "Infrared micro-spectrometer based on a diffraction grating," Sensors and Actuators a-Physical, vol. 92, no. 1–3, pp. 88–95, 2001.

[28] W. Wei, S. Huang, N. Wang, Z. Jin, J. Zhang, and W. Chen, "A Near-Infrared Spectrometer Based on Novel Grating Light Modulators," Sensors, vol. 9, no. 4, pp. 3109–3121, 2009.

[29] J. H. Correia, G. de Graaf, S. H. Kong, M. Bartek, and R. F. Wolffenbuttel, "Single-chip CMOS optical microspectrometer," Sensors Actuators A Phys., vol. 82, no. 1–3, pp. 191–197, May 2000.

[30] G. Lammel, S. Schweizer, and P. Renaud, "Microspectrometer based on a tunable optical filter of porous silicon," Sensors Actuators A Phys., vol. 92, no. 1–3, pp. 52–59, 2001.

[31] D. Sander, J. Müller, and È. Mu, "Selffocussing phase transmission grating for an integrated optical microspectrometer," Sensors Actuators A Phys., vol. 88, no. 1, pp. 1–9, 2001.

[32] S.-W. Wang, M. Li, C.-S. Xia, H.-Q. Wang, X.-S. Chen, and W. Lu, "128 Channels of Integrated Filter Array Rapidly Fabricated By Using the Combinatorial Deposition Technique," Appl. Phys. B, vol. 88, no. 2, pp. 281–284, Jul. 2007.

[33] X. Wang, A. Albrecht, H. H. Mai, C. Woidt, T. Meinl, M. Hornung, M. Bartels, and H. Hillmer, "High resolution 3D NanoImprint technology: Template fabrication, application in Fabry-Pérot-filter-array-based optical nanospectrometers," Microelectron. Eng., vol. 110, pp. 44–51, 2013.

[34] A. Albrecht, X. Wang, H. H. Mai, T. Schotzko, I. Memon, M. Bartels, M. Hornung, and H. Hillmer, "High Vertical Resolution 3D Nanolmprint Technology and its Application in Optical Nanosensors," Nonlinear Opt. Quantum Opt., vol. 43, no. 1–4, pp. 339–353, 2012.

[35] R. Ji, M. Hornung, M. a. Verschuuren, R. van de Laar, J. van Eekelen, U. Plachetka, M. Moeller, and C. Moormann, “UV enhanced substrate conformal imprint lithography (UV-SCIL) technique for photonic crystals patterning in LED manufacturing,” Microelectron. Eng., vol. 87, no. 5–8, pp. 963–967, 2010.

[36] M. Vogler, M. Bender, U. Plachetka, A. Fuchs, and S. Wiedenberg, “Low Viscosity and Fast Curing Polymer System for UV-based Nanoimprint Lithography and its Processing,” Proc. SPIE, vol. 6517, 2007.

[37] H. Atobe, H. Hiroshima, and Q. Wang, “Evaluation of viscosity characteristics of spin-coated UV nanoimprint resin,” Jpn. J. Appl. Phys., vol. 49, no. 6, 2010.

[38] C. Fabry and A. Perot, “Théorie et applications d’une nouvelle méthode de spectroscopie interférentielle,” Ann. Chim. Phys, vol. 16, Jan. 1899.

[39] H. Venghaus, Wavelength Filters in Fibre Optics. Springer Berlin Heidelberg, 2006.

[40] H. A. MacLeod, Thin-Film Optical Filters, Third Edition. CRC Press, 2001.

[41] S. Irmer, “Air-Gap Based Vertical Cavity Micro-Opto- Electro-Mechanical Fabry-Pérot Filters,” PhD thesis, University of Kassel, 2005.

[42] J. M. Vaughan, The Fabry-Perot Interferometer: History, Theory, Practice, and Applications. Taylor & Francis, 1989.

[43] S. Kasap, H. Ruda, and Y. Boucher, Cambridge Illustrated Handbook of Optoelectronics and Photonics. Cambridge, 2009.

[44] A. Emadi, H. Wu, S. Grabarnik, G. De Graaf, K. Hedsten, P. Enoksson, J. H. Correia, and R. F. Wolffenbuttel, “Fabrication and characterization of IC-Compatible Linear Variable Optical Filters with application in a micro-spectrometer,” Sensors Actuators A Phys., vol. 162, no. 2, pp. 400–405, 2010.

[45] J. H. Correia, M. Bartek, and R. Wolffenbuttel, “High-Selectivity Single-Chip Spectrometer in Silicon for Operation at Visible Part of the Spectrum,” IEEE Trans. Electron Devices, vol. 47, no. 3, pp. 553–559, 2000.

[46] H. Hillmer, “Optisches Filter und Verfahren zu seiner Herstellung,” DE 10 2006 039 071, 2012.

[47] M. Bartels, F. Köhler, S. Wittzack, X. Wang, and H. Hillmer, “Ultra

precise nanoimprint templates," Nanos. 03.08, p. 18, 2008.

[48] M. Bartels, S. Wittzack, F. Köhler, X. Wang, A. Albrecht, S. Schudy, M. Engenhorst, H. H. Mai, O. Setyawati, T. Woit, C. Woidt, and H. Hillmer, "High Vertical Resolution 3D Nanoimprint Technology for Nanophotonic Applications," IEEE/LEOS Int. Conf. Opt. MEMS Nanophotonics, pp. 87–88, 2009.

[49] X. Wang, A. Albrecht, S. Schudy, T. Woit, V. Daneker, K. Schultz, H. H. Mai, F. Köhler, S. Wittzack, M. Bartels, and H. Hillmer, "High-resolution, Low-cost Microsensors for Networked Sensing Systems: Optical Nanospectrometers with Nanoimprinted Cavities of Filter Arrays," in IEEE Technical Digest INSS, 2010, pp. 171–174.

[50] H. H. Mai, A. Albrecht, C. Woidt, X. Wang, V. Daneker, O. Setyawati, T. Woit, K. Schultz, M. Bartels, and H. Hillmer, "3D nanoimprinted Fabry–Pérot filter arrays and methodologies for optical characterization," Appl. Phys. B, vol. 107, no. 3, pp. 755–764, May 2012.

[51] S. Y. Chou, P. R. Krauss, and P. J. Renstrom, "Nanoimprint lithography," vol. 14, no. June, pp. 4129–4133, 1996.

[52] J. L. Wilbur, A. Kumar, H. A. Biebuyck, E. Kim, and G. M. Whitesides, "Microcontact printing of self-assembled monolayers: applications in microfabrication," Nanotechnology, vol. 7, no. 4, pp. 452–457, Dec. 1996.

[53] F. Bessueille, M. Pla-Roca, C. a. Mills, E. Martinez, J. Samitier, and A. Errachid, "Submerged microcontact printing (SμCP): An unconventional printing technique of thiols using high aspect ratio, elastomeric stamps," Langmuir, vol. 21, no. 10, pp. 12060–12063, 2005.

[54] Y. Xia and G. M. Whitesides, "Soft lithography," Annu. Rev. Mater. Sci., vol. 28, no. 12, pp. 153–184, 1998.

[55] A. P. Quist, E. Pavlovic, and S. Oscarsson, "Recent advances in microcontact printing.," Anal. Bioanal. Chem., vol. 381, no. 3, pp. 591–600, Feb. 2005.

[56] B. Y. Xia, J. J. Mcclelland, R. Gupta, D. Qin, X. Zhao, L. L. Sohn, R. J. Celotta, and G. M. Whitesides, "Replica Molding Using Polymeric Materials : A Practical Step Toward Nanomanufacturing," Adv. Mater., no. 2, pp. 147–149, 1997.

[57] M. D. Tang, A. P. Golden, and J. Tien, "Molding of three-dimensional microstructures of gels.," J. Am. Chem. Soc., vol. 125, no. 43, pp. 12988–

9, Oct. 2003.

[58] M. Hornung, R. Ji, M. Verschuuren, and R. van den Laar, “6 inch full field wafer size nanoimprint lithography for photonic crystals patterning,” in 10th IEEE International Conference on Nanotechnology, 2010, pp. 339–342.

[59] J. Perumal, T. H. Yoon, H. S. Jang, J. J. Lee, and D. P. Kim, “Adhesion force measurement between the stamp and the resin in ultraviolet nanoimprint lithography--an investigative approach.,” Nanotechnology, vol. 20, no. 5, Mar. 2009.

[60] Y. Kanamori, “Fabrication of soft nanoimprint stamps and polymer subwavelength gratings by spin coating techniques,” Proc. SPIE, vol. 5635, pp. 144–153, 2005.

[61] P. Gallo, B. Viallet, E. Daran, and C. Fontaine, “Efficient aminosilane adhesion promoter for soft nanoimprint on GaAs,” Appl. Phys. Lett., vol. 87, no. 18, p. 183111, 2005.

[62] Y. Chen, “Soft nanoimprint lithography,” Proc. SPIE, vol. 5645, pp. 283–288, 2005.

[63] W. Zhou, Nanoimprint Lithography: An Enabling Process for Nanofabrication, 1st ed. Springer Berlin Heidelberg, 2013.

[64] S. Chou, P. Krauss, and P. Renstrom, “Imprint of sub-25nm vias and trenches in polymers,” Appl. Phys. Lett., vol. 67, no. 21, p. 3114, 1995.

[65] N. Koo, U. Plachetka, M. Otto, J. Bolten, J.-H. Jeong, E.-S. Lee, and H. Kurz, “The fabrication of a flexible mold for high resolution soft ultraviolet nanoimprint lithography,” Nanotechnology, vol. 19, no. 22, p. 225304, Jul. 2008.

[66] S. Landis, N. Chaix, C. Gourgon, C. Perret, and T. Leveder, “Stamp design effect on 100 nm feature size for 8 inch NanoImprint lithography.,” Nanotechnology, vol. 17, no. 10, pp. 2701–2709, 2006.

[67] T. Balla, S. M. Spearing, and A. Monk, “An assessment of the process capabilities of nanoimprint lithography,” J. Phys. D. Appl. Phys., vol. 41, no. 17, p. 174001, 2008.

[68] R. Ji, M. Hornung, M. A. Verschuuren, R. van de Laar, J. van Eekelen, U. Plachetka, M. Moeller, and C. Moormann, “UV enhanced substrate conformal imprint lithography (UV-SCIL) technique for photonic crystals patterning in LED manufacturing,” Microelectron. Eng., vol. 87, no. 5–8,

pp. 963–967, May 2010.

[69] L. J. Guo, “Recent progress in nanoimprint technology and its applications,” J. Phys. D. Appl. Phys., vol. 37, no. 11, pp. R123–R141, Jun. 2004.

[70] R. W. Cahn, P. Haasen, and E. J. Kramer, Materials science and technology: a comprehensive treatment. Wiley-VCH Verlag GmbH, 1996.

[71] K. Allaert, A. Van Calster, H. Loos, and A. Lequesne, “A Comparison Between Silicon Nitride Films Made by PCVD of N[sub 2]-SiH[sub 4]/Ar and N[sub 2]-SiH[sub 4]/He,” J. Electrochem. Soc., vol. 132, no. 7, p. 1763, 1985.

[72] M. Köhler, Etching in Microsystem Technology. John Wiley & Sons, 2008.

[73] K. Nojiri, Dry Etching Technology for Semiconductors. Springer, 2014.

[74] G. Bose, IC Fabrication Technology, 1st ed. McGraw-Hill Education, 2014.

[75] G. S. May and C. J. Spanos, Fundamentals of Semiconductor Manufacturing and Process Control. John Wiley & Sons, 2006.

[76] J. Chopra, “Analysis of Lithography Based Approaches in Development of Semiconductors,” Int. J. Comput. Sci. Inf. Technol., vol. 6, no. 6, pp. 61–72, 2014.

[77] T. Weichelt, U. Vogler, L. Stuerzebecher, R. Voelkel, and U. D. Zeitner, “Resolution enhancement for advanced mask aligner lithography using phase-shifting photomasks.,” Opt. Express, vol. 22, no. 13, Jun. 2014.

[78] M. J. Madou, Fundamentals of Microfabrication: The Science of Miniaturization, Second Edition. CRC Press, 2002.

[79] Stephen M. Rossnagel, William D. Westwood, and Jerome J. Haber, Handbook of Plasma Processing Technology: Fundamentals, Etching, Deposition, and Surface Interactions. Noyes Publications, 1990.

[80] X. Wang, “High Resolution 3D Nanoimprint Technology: Template Fabrication, Aplication in Fabry-Pérot-filter-based Nanospectrometers,” PhD thesis, University of Kassel, 2010.

[81] B. T. Chen, “Investigation of the solvent-evaporation effect on spin coating of thin films,” Polym. Eng. Sci., vol. 23, no. 7, pp. 399–403, May 1983.

[82] D. B. Hall, P. Underhill, and J. M. Torkelson, “Spin Coating of Thin and

Ultrathin Polymer Films," Polym. Eng. Sci., vol. 38, no. 12, pp. 2039–2045, 1998.

[83] A. Kitamura, "Thermal effects on liquid film flow during spin coating," Phys. Fluids, vol. 13, no. 10, p. 2788, 2001.

[84] J. H. La, "An Investigation of Spin Coating of Electron Resists," vol. 19, no. 15, pp. 1117–1121, 1979.

[85] M. Pannek, T. Dunkel, and D. W. Schubert, "Effect of a bell-shaped cover in spin coating process on final film thickness," Mater. Res. Innov., vol. 4, no. 5–6, pp. 340–343, Apr. 2001.

[86] L. Wu, "Spin coating of thin liquid films on an axisymmetrically heated disk," Phys. Fluids, vol. 18, no. 6, 2006.

[87] D. W. Schubert and T. Dunkel, "Spin coating from a molecular point of view: its concentration regimes, influence of molar mass and distribution," Mater. Res. Innov., vol. 7, no. 5, pp. 314–321, Oct. 2003.

[88] D. B. Mitzi, L. L. Kosbar, C. E. Murray, M. Copel, and A. Afzali, "High-mobility ultrathin semiconducting films prepared by spin coating," Nature, vol. 428, no. 6980, pp. 299–303, Mar. 2004.

[89] A. M. Taleb, W. A. A. Twej, B. T. Chiad, and A. J. H. Al-wattar, "Study of Spinning Speed , Multilayer Coating and Formaldehyde Effect on Preparation of Xerogel Film Doped with Laser Dyes," African Phys. Rev., vol. 3, pp. 117–124, 2009.

[90] S. Middleman and A. K. Hochberg, "Process engineering analysis in semiconductor device fabrication," AlChE, vol. 41, no. 1, 1995.

[91] M. D. Tyona, "A comprehensive study of spin coating as a thin film deposition technique and spin coating equipment," Adv. Mater. Res., vol. 4, no. 4, pp. 181–193, 2013.

[92] M. D. Tyona, "A theoritical study on spin coating technique," Adv. Mater. Res., vol. 2, no. 4, pp. 195–208, 2013.

[93] N. Sahu, B. Parija, and S. Panigrahi, "Fundamental understanding and modeling of spin coating process: A review," Indian J. Phys., vol. 83, no. 4, pp. 493–502, 2009.

[94] H. Fujiwara, Spectroscopic Ellipsometry: Principles and Applications. Wiley, 2007.

[95] J. A. Woollam, B. D. Johs, C. M. Herzinger, J. N. Hilfiker, R. A.

Synowicki, and C. L. Bungay, "Overview of variable-angle spectroscopic ellipsometry (VASE): I. Basic theory and typical applications," Proc. SPIE - Int. Soc. Opt. Eng., vol. -1, pp. 3–28, Jun. 1999.

[96] D. K. Schroder, Semiconductor Material and Device Characterization. John Wiley & Sons, 2006.

[97] C. O Mahony, M. Hill, M. Brunet, R. Duane, and A. Mathewson, "Characterization of micromechanical structures using white-light interferometry," Meas. Sci. Technol., vol. 14, no. 10, pp. 1807–1814, Oct. 2003.

[98] J. C. Wyant, "White light interferometry," Proc. SPIE - Int. Soc. Opt. Eng., vol. 4737, no. 2002, pp. 98–107, 2002.

[99] H. H. Mai, "Characterization of Novel Fabry Pérot Filter Arrays for Nanospectrometers in Medical Applications," PhD thesis, University of Kassel, 2012.

[100] H. Wallace, "A Different Kind of Chemistry: A History of Tungsten Halogen Lamps," IEEE Ind. Appl. Mag., no. December, p. 11, 2001.

[101] Raymond Kane and Heinz Sell, Revolution in Lamps: A Chronicle of 50 Years of Progress. Fairmont Press, 2001.

[102] Robert R. Alfano, The Supercontinuum Laser Source: Fundamentals with Updated References. Springer Science & Business Media, 2006.

[103] Koheras Super K EXW, "SuperK EXTREME supercontinuum lasers." [Online]. Available: http://www.nktphotonics.com/product/superk-extreme-supercontinuum-lasers/?cid=7856.

[104] S. Irmer, J. Daleiden, V. Rangelov, C. Prott, and F. Römer, "Ultralow Biased Widely Continuously Tunable Fabry-Pérot Filter," IEEE Photonics Technol. Lett., vol. 15, no. 3, pp. 434–436, 2003.

[105] F. Römer, "Charakterisierung und Simulation optischer Eigenschaften von mikromechanisch abstimmbaren Filterbauelementen," PhD thesis, University of Kassel, 2005.

[106] A. Albrecht, "Substrate Conformal Imprint Lithography als innovatives Verfahren zur Herstellung von Nanospektrometern im sichtbaren Spektralbereich," PhD thesis, University of Kassel, 2012.

[107] Suss Micro Tec. AG, "SCIL video," 2010. [Online]. Available: http://www.suss.com/markets/nanoimprint-lithography/scil/scil-video.html.

[108] M. R. Amirzada, A. Tatzel, V. Viereck, and H. Hillmer, "Surface roughness analysis of SiO_2 for PECVD, PVD and IBD on different substrates," Appl. Nanosci., doi: 10.1007/s13204-015-0432-8 , 2015.

Publication

1. **Duc Toan Nguyen**, M. Ababtain, I. Memon, A. Ullah, A. Istock, C. Woidt, W. Xie, P. Lehmann, H. Hillmer (2016). 3D nanoimprint for NIR Fabry-Pérot filter arrays: fabrication, characterization and comparison of different cavity designs. Applied Nanoscience: pp. 1- 9 (2016); http://dx.doi.org/10.1007/s13204-016-0524-0.

2. A. Ullah, H. Wilke, I. Memon, Y. Shen, **D. T. Nguyen**, C. Woidt and H. Hillmer (2015). Stress relaxation in dual ion beam sputtered Nb_2O_5 and SiO_2 thin films: application in a Fabry–Pérot filter array with 3D nanoimprinted cavities. J. Micromech. Microeng. 25.